

INFORMATION TO USERS

This manuscript has been reproduced from the microfilm master. UMI films the text directly from the original or copy submitted. Thus, some thesis and dissertation copies are in typewriter face, while others may be from any type of computer printer.

The quality of this reproduction is dependent upon the quality of the copy submitted. Broken or indistinct print, colored or poor quality illustrations and photographs, print bleedthrough, substandard margins, and improper alignment can adversely affect reproduction.

In the unlikely event that the author did not send UMI a complete manuscript and there are missing pages, these will be noted. Also, if unauthorized copyright material had to be removed, a note will indicate the deletion.

Oversize materials (e.g., maps, drawings, charts) are reproduced by sectioning the original, beginning at the upper left-hand corner and continuing from left to right in equal sections with small overlaps. Each original is also photographed in one exposure and is included in reduced form at the back of the book.

Photographs included in the original manuscript have been reproduced xerographically in this copy. Higher quality 6" x 9" black and white photographic prints are available for any photographs or illustrations appearing in this copy for an additional charge. Contact UMI directly to order.

UMI

A Bell & Howell Information Company
300 North Zeeb Road, Ann Arbor MI 48106-1346 USA
313/761-4700 800/521-0600

ANATEXIS AND METAMORPHISM OF CRUSTAL ROCKS DURING
MAGMATIC ACCRETION: FIELD AND NUMERICAL RESULTS

by

Scott A. Barboza

A dissertation submitted in partial fulfillment of the requirements for the degree of

Doctor of Philosophy

University of Washington

1998

Approved by

GEORGE W. BERGMAN
Chairperson of Supervisory Committee

Program Authorized

to Offer Degree

GEOLOGY

Date

November 20, 1998

UMI Number: 9916621

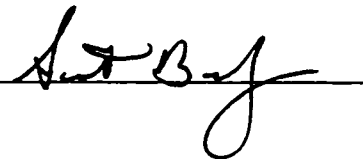
**UMI Microform 9916621
Copyright 1999, by UMI Company. All rights reserved.**

**This microform edition is protected against unauthorized
copying under Title 17, United States Code.**

UMI
300 North Zeeb Road
Ann Arbor, MI 48103

Doctoral Dissertation

In presenting this dissertation in partial fulfillment of the requirements for the Doctoral degree at the University of Washington, I agree that the Library shall make its copies freely available for inspection. I further agree that extensive copying of this dissertation is allowable only for scholarly purposes, consistent with "fair use" as prescribed in the U.S. Copyright Law. Requests for copying or reproduction of this dissertation may be referred to University Microfilms, 1490 Eisenhower Place, P.O. Box 975, Ann Arbor, MI 48106, to whom the author has granted "the right to reproduce and sell (a) copies of the manuscript in microform and/or (b) printed copies of the manuscript made from microform."

Signature 

Date 11/20/98

University of Washington

Abstract

ANATEXIS AND METAMORPHISM OF CRUSTAL ROCKS DURING
MAGMATIC ACCRETION: FIELD AND NUMERICAL RESULTS

by Scott A. Barboza

Chairperson of the Supervisory Committee: Professor George W. Bergantz

Department of Geological Sciences

The generation of crustal melt and its subsequent segregation and ascent comprise a fundamental set of processes that results in the chemical differentiation of continental crust. Interpreting magmatic products and explaining their petrologic diversity requires a quantitative understanding of the physical and chemical factors that influence the generation of felsic melts in the source region. Crustal melting followed by the fractionation of refractory phases, and/or mixing crustal components with fractionated mantle-derived melts can cause compositional variability in the products of crustal magmatism. Both models of granitoid magmatism imply a change in the thermal conditions in the source region, a requirement that may be explained by the intrusion of sills of mantle-derived magma at or near the base of the crust (underplating).

However, the response of crustal rocks to the intrusion of mafic magma (magmatic accretion) is not well understood. Variable estimates of the time and length scales of crustal melting following magmatic accretion have been obtained by different theoretical and numerical studies. Crustal melting models based on the assumption of near turbulent conditions within the intrusion have predicted rapid cooling and bulk melting of the overlying crustal rocks. The results of other numerical studies suggest lower rates of heat transfer and more limited crustal melting in response to underplating. An integrated approach linking the results of numerical simulations with field and geochemical observations is required to discriminate between the alternative models and yield a more complete model of crustal anatexis.

In this study I present the results of a series of numerical and field studies. The numerical studies demonstrate that rapid convective heat transfer and bulk melting during magmatic accretion is a limiting case which may not be realized in the natural setting due to the complex chemical and rheological response of crustal rocks to the heat released during magmatic accretion. The field studies demonstrate that emplacement of even large volumes of mafic magma may be associated with only narrow contact aureoles of depleted rocks. These results demonstrate that magmatic accretion may not inexorably lead to regional metamorphism and widespread anatexis.

TABLE OF CONTENTS

| | |
|--|------|
| LIST OF FIGURES | v |
| LIST OF TABLES | viii |
| CHAPTER 1: DYNAMIC MODEL OF DEHYDRATION MELTING | |
| MOTIVATED BY A NATURAL ANALOG: APPLICATIONS TO THE | |
| IVREA-VERBANO ZONE, NORTHERN ITALY | 1 |
| INTRODUCTION | 1 |
| THE IVREA-VERBANO ZONE: A FIELD EXAMPLE | 4 |
| DEHYDRATION MELTING | 6 |
| METHODOLOGY..... | 6 |
| General Nature of Melt Movement | 6 |
| Thermodynamic Model | 9 |
| Building the binary | 11 |
| Model description..... | 12 |
| RESULTS AND DISCUSSION..... | 14 |
| Thermal evolution and the distribution of melt above the underplating sill | 14 |
| Convective velocities and the rheological and thermal envelope of | |
| convection | 17 |
| Influence of the rheological parameters on convective vigor..... | 18 |
| Evolution of convective vigor with time | 19 |
| An application to the Ivrea-Verbano Zone | 21 |
| Melt extraction | 22 |
| The existence of a low melt fraction window of extractable melt | 23 |
| CONCLUSIONS AND SUMMARY | 24 |

CHAPTER 2: MELT PRODUCTIVITY AND RHEOLOGY:

COMPLEMENTARY INFLUENCES ON THE PROGRESS OF

MELTING 35
INTRODUCTION 35
CONTINUUM MODEL 36
PHASE DIAGRAM..... 40
NUMERICAL SOLUTION 43
EXAMPLE PROBLEM 44
CONCLUSIONS..... 51

CHAPTER 3: RHEOLOGICAL TRANSITIONS AND THE PROGRESS OF

MELTING OF CRUSTAL ROCKS..... 66
INTRODUCTION 66
CONTINUUM MODEL 69
MODEL ASSUMPTIONS 74
MODEL DESCRIPTION AND GEOLOGICAL MOTIVATION 75
RESULTS AND DISCUSSION 77
 Initiation of convection..... 78
 Influence of rheological transitions on the progress of melting 80
 Sensitivity of thermal evolution to rheological transitions..... 81
 Relative importance of melt productivity and the rheological transition 82
CONCLUSIONS..... 83

CHAPTER 4: REGIONAL GRANULITE-FACIES METAMORPHISM IN

THE IVREA ZONE: IS THE MAFIC COMPLEX THE SMOKING GUN

OR A RED HERRING?..... 96
INTRODUCTION 96
GEOLOGIC FRAMEWORK..... 97
THE RELATIONSHIP BETWEEN BASALTIC MAGMATISM, CRUSTAL
 ANATEXIS, AND GRANULITE-FACIES METAMORPHISM 99
 Field and Petrologic evidence..... 99

| | |
|---|------------|
| Geochemical Evidence | 101 |
| IMPLICATIONS - BOTH REGIONAL AND CONTACT MELTING | 102 |
| DISCUSSION..... | 104 |
| CONCLUSIONS..... | 105 |
| CHAPTER 5: METAMORPHISM AND ANATEXIS IN THE MAFIC | |
| COMPLEX CONTACT AUREOLE, IVREA ZONE, NORTHERN | |
| ITALY | 110 |
| INTRODUCTION | 110 |
| GEOLOGIC SETTING..... | 112 |
| Regional Framework | 112 |
| LITHOLOGIES | 114 |
| Mafic Complex | 114 |
| Kinzigitic Formation | 115 |
| Geochronology..... | 117 |
| METAMORPHISM..... | 118 |
| Between upper and lower Val Strona di Omegna and Val d'Ossola | 120 |
| Between lower Val Sesia and Val Strona di Postua..... | 122 |
| THERMOBAROMETRY | 126 |
| PRESSURE-TEMPERATURE HISTORY..... | 129 |
| Petrogenetic grid | 129 |
| Summary of inferred <i>PTt</i> path | 129 |
| ANATEXIS | 132 |
| Samples..... | 133 |
| Results | 134 |
| DISCUSSION AND CONCLUSIONS..... | 135 |
| Tectonic implications | 135 |
| Magmatic accretion models..... | 140 |
| BIBLIOGRAPHY | 158 |

APPENDIX A: DERIVATION OF THE LOGARITHMIC ISOCON

METHOD175

LIST OF FIGURES

| <i>Number</i> | <i>Page</i> |
|--|-------------|
| Figure 1.1. Schematic diagram for melting model. | 26 |
| Figure 1.2. Geologic sketch map of the Southern Alps west of the Lago Maggiore..... | 27 |
| Figure 1.3. Kinematic viscosity and permeability as a function of the melt fraction. | 28 |
| Figure 1.4. 10 kbar NKM silica, alumina, and titania saturated pseudo-ternary liquidus phase relations. | 29 |
| Figure 1.5. Predicted variation of melt fraction as a function of temperature. | 30 |
| Figure 1.6. Evolution of melt distribution. | 31 |
| Figure 1.7. Contours of three parameters for Case 1 ($T_{\text{contact}} = 1000 \text{ }^\circ\text{C}$) and Case 2 ($T_{\text{contact}} = 900 \text{ }^\circ\text{C}$) simulations. | 32 |
| Figure 1.8. Propensity for porous flow of melt as a function of the melt fraction.. | 33 |
| | |
| Figure 2.1. Schematic diagram of the rheological model. | 53 |
| Figure 2.2. Plot of the kinematic viscosity of the mixture and the melt. | 54 |
| Figure 2.3. Plot of the melt productivity for the two cases. | 56 |
| Figure 2.4. Schematic of the two invariant-point binary phase diagram. | 55 |
| Figure 2.5. Schematic of computational domain. | 57 |
| Figure 2.6. The mixture velocity (arrows) and temperature (contours in $^\circ\text{C}$) of the two models at $t^*=0.2$ | 58 |
| Figure 2.7. Plot of the flux ratio. | 59 |
| Figure 2.8. Ratio of the global kinetic energy in the two invariant-point system to that of the one-invariant point system. | 60 |

| | |
|---|-----|
| Figure 3.1. Schematic depiction of the CMF model..... | 85 |
| Figure 3.2. Plot of the kinematic viscosity of the mixture and the melt. | 86 |
| Figure 3.3. Plot of the kinematic viscosity and permeability against melt fraction. | 87 |
| Figure 3.4. Melt productivity two lithologies..... | 88 |
| Figure 3.5. Schematic of the computational domain. | 89 |
| Figure 3.6. Sample results 79.3 years after the initiation of the simulations with $\zeta=10, 8, \text{ and } 6$ | 90 |
| Figure 3.7. Distance the biotite dehydration isopleth had propagated as a function of time, for simulations with $\zeta=10, 8, \text{ and } 6$ | 91 |
| Figure 3.8. Melting efficiency as a function of time predicted by the simulations with the various rheological models..... | 92 |
| Figure 3.9. Melting efficiency as a function of time predicted by the simulations with the various rheological models..... | 93 |
| | |
| Figure 4.1. Simplified geologic map of the Southern Alps west of Lago Maggiore..... | 107 |
| Figure 4.2. K/Rb ratio vs. wt.% K. | 108 |
| Figure 4.3. Classification of granitoid rocks in the Ivrea and Strona-Ceneri zones according to normative An-Ab-Or compositions..... | 109 |
| | |
| Figure 5.1. Geologic map of the southern Ivrea and Strona-Ceneri zones west of Lago d'Orta..... | 142 |
| Figure 5.2. Detail sample location maps along R. Forcioula and F. Duggia. | 143 |
| Figure 5.3. AFM projection from muscovite and K-feldspar..... | 144 |
| Figure 5.4. Reaction textures..... | 145 |
| Figure 5.5. X-ray maps of grossular component in garnet..... | 146 |
| Figure 5.6. Calculated <i>PT</i> positions of thermobarometric equilibria. | 147 |
| Figure 5.7. Partial petrogenetic grid and proposed <i>PTt</i> path..... | 148 |

| | |
|--|-----|
| Figure 5.8. Isocon mass balance between migmatitic metapelite melanosome samples and the calculated composite metapelite protolith..... | 149 |
| Figure 5.9. Isocon mass balance between the predicted melt and leucosomes immediately adjacent to the migmatitic metapelite melanosomes..... | 150 |
| Figure 5.10. Plot of LILE's vs. SiO ₂ for metapelite melanosomes and leucotonalite leucosomes..... | 151 |
| Figure 5.11. Inferred tectonic evolution of the Ivrea zone..... | 152 |

LIST OF TABLES

| <i>Number</i> | <i>Page</i> |
|---|-------------|
| Table 1.1: Data for the model..... | 34 |
| Table 2.1: Nomenclature..... | 61 |
| Table 2.2: Geometry of phase diagram..... | 62 |
| Table 2.3: Melt fractions and phase compositions..... | 63 |
| Table 2.4: Auxiliary relations and linking functions..... | 64 |
| Table 2.4: Values of constants..... | 65 |
| Table 3.1: Nomenclature..... | 94 |
| Table 3.2: Values for the various material properties and for the initial and boundary conditions used in the numerical simulations..... | 95 |
| Table 5.1: Whole rock major- and trace-element compositions of representative metapelite melanosomes..... | 153 |
| Table 5.2: Whole rock major- and trace-element compositions of representative leucosomes..... | 154 |
| Table 5.3: Representative matrix biotite analyses..... | 155 |
| Table 5.4: Representative garnet core compositions..... | 156 |
| Table 5.5: Representative matrix plagioclase analyses..... | 157 |

ACKNOWLEDGMENTS

I thank George W. Bergantz for his assistance with the numerical and field studies and for his careful and thoughtful reviews, which resulted in numerous improvements to the manuscript. I also wish to acknowledge James E. Quick, Silvano Sinigoi, and Michael Brown for many fruitful discussions, expert guidance, and logistical support for the field surveys. I thank I. Stewart McCallum, Bernard W. Evans, and Mark S. Ghiorso for serving on my committee, and Luigi Burlini and Scott Kuehner for assistance with technical aspects of the research.

This research was supported by grants from the Geological Society of America, the National Science Foundation, the University of Washington Royalty Research Fund, and the University of Washington Graduate Research Fund.

DEDICATION

I wish to dedicate this dissertation to the memory of Joanne Shirley Barboza (1934-1995).

CHAPTER 1: DYNAMIC MODEL OF DEHYDRATION MELTING MOTIVATED
BY A NATURAL ANALOG: APPLICATIONS TO THE IVREA-VERBANO
ZONE, NORTHERN ITALY

INTRODUCTION

Many continental granitoids contain at least some component of crustally derived material (Brown, 1994; Harris et al., 1995; Pitcher, 1993; Wyllie, 1977). One mechanism for generating crustal melts is dehydration melting following the ponding of mantle-derived magma within or at the base of the crust (Bergantz and Dawes, 1994; Huppert and Sparks, 1988). Of particular interest is the melting of pelitic rocks, as there is ample field evidence for this process during contact metamorphism (Grant and Frost, 1990; Harris et al., 1995; Symmes and Ferry, 1995). However, little is known about the rates of melt generation and mechanisms of melt transport. Some studies have indicated that melt may be removed from the source region through a rather efficient mechanism. For example, in the Ballachulish aureole, granitic melt appears to have segregated into leucosomes in less than 5×10^4 years (Buntebarth, 1991; Sawyer, 1994). Sawyer (1991) proposed that tonalitic melt in the Grenville front probably separated from its source in less than 100 years.

Clemens and Mawer (1992) have argued that the mechanism for melt removal may be fracturing resulting from the positive ΔV of hydrate breakdown during dehydration melting while other studies have emphasized the role of

deformation and shear (Brown et al., 1995; Davidson et al., 1995; Rushmer, 1995; Sawyer, 1994). Melt segregation in the mantle, on the other hand, is thought to result primarily from buoyancy forces which initiate the porous flow of melt (Nicolas, 1989). It is likely that each of these mechanisms (fracturing, shear, and buoyancy), to some extent, contributes to the extraction of crustal melts from their source. However, the relative importance of buoyancy or shear in the melt transport process is poorly understood.

The thermal evolution of underplating regions has also been a subject of many debates. Analog experiments and mathematical models have led to the proposal that underplating of basaltic magmas will lead to bulk melting of the country rock and the thermal evolution of underplating regions will be dominated by convective processes (Huppert and Sparks, 1988). However, there is little direct geological or geochemical evidence to support this view. As a result, the style and vigor of convection in both the basaltic sill and the overlying country rock has been subject to much debate (Huppert and Sparks, 1991; Marsh, 1991), and numerous alternate models have been advanced (Bergantz and Dawes, 1994).

One of the central themes of this study is that rheological variations associated with the increase in melt fraction during melting provide the dominant control on the dynamics of the growing region of partial melt. The notion of a distinct critical melt fraction (CMF), at which the skeleton of restitic crystals breaks down, and stresses are supported by the fluid phase, requires substantial revision for geological systems undergoing partial melting. The rheological transitions in partially molten

rocks can be complex and difficult to generalize (Rushmer, 1995; Rutter and Neumann, 1995). The rheological model invoked in this study is an extension of mixture theory for two-phase systems (Agarwal and O'Neill, 1988; Ni and Beckermann, 1991; Oldenburg and Spera, 1992). The CMF can still play a role in the rheological characterization of partially molten material, but it does not represent an abrupt transition from a rigid skeleton to a crystal-laden fluid, but rather a gradual transition between the two.

The intent of this study is to explore the relationship between melt generation, the dynamics of melt movement, and the thermal evolution of an underplated region adhering to documented geological conditions. To this end a thermo-mechanical model has been developed to: (i) explore the time and length scales of dehydration melting and the dynamics of the melt movement following underplating; (ii) to evaluate the influence of thermally and compositionally induced buoyancy as a mechanism for the extraction of felsic melt. A numerical study is particularly well-suited to address such questions as experiments carried out with laboratory analogs cannot be used to study the relative importance of such processes in a physically realistic manner (Bergantz, 1995; Bergantz and Dawes, 1994; Jaupart and Tait, 1995). Irvine (1970), Bergantz (1989), and Bowers et al. (1990) have used a similar modeling approach for evaluating partial melting during contact metamorphism. However, these studies allowed no convection in the region of partial melting and cannot resolve issues related to the dynamics of melt movement.

The geometrical and thermal relationships used in this study are based on current models for the emplacement dynamics of the underplated igneous complex at the Ivrea-Verbano Zone (IVZ) (Quick et al., 1994). A simplified version of this process is summarized in Figure 1.1. Mantle-derived magma near its liquidus temperature (1200 °C) is emplaced in a small, spatially stable, sill at the base of an initially unmelted sequence of pelitic rocks in the lower crust. The growth of a solid, conductive quenched margin causes the contact to quickly stabilize at a temperature intermediate between that of the country rock and the initial temperature of the intruding basalt. Melting in the country rock proceeds as the intrusion cools and buoyant instabilities develop in the growing lens of felsic melt. The movement of melt that results from these instabilities advects heat away from the contact with the intrusion and yields a region of partial melting whose geometry and rate of growth differs significantly from both conductive models and those that assume convection is turbulent.

THE IVREA-VERBANO ZONE: A FIELD EXAMPLE

The results of this study will be compared to the Ivrea-Verbano zone (IVZ) in northern Italy, arguably the premier locality for the study of dehydration melting subsequent to underplating. The IVZ (Figure 1.2) is a lower crustal section consisting of a 140 km long sequence of steeply dipping pelitic and mafic rocks metamorphosed under amphibolite to granulite facies conditions (Zingg, 1980). To

the northwest, the IVZ is separated from rocks of the Austroalpine Domain by the Insubric Line - a major shear zone that marks the southern extent of Alpine deformation (Schmid et al., 1987). To the southeast, the IVZ is separated from rocks of intermediate crustal depth within the Serie dei Laghi unit by the Cremosina, Pogallo, and CMB Lines (Boriani et al., 1977; Boriani et al., 1988; Boriani and Sacchi, 1973; Handy, 1987).

The IVZ is composed of two major lithologic divisions - the Kinzigite Formation and the Mafic Complex. The Mafic Complex is primarily composed of rocks of gabbroic composition, but also includes large peridotite bodies near the Insubric Line and dioritic rocks near the contact with the Kinzigite Formation (Rivalenti et al., 1980; Rivalenti et al., 1975; Sinigoi et al., 1994). The Kinzigite Formation is composed predominantly of sillimanite-bearing paragneisses termed "kinzigites" and "stronalites" in the amphibolite and granulite grade respectively (Zingg, 1980). The rocks of the Kinzigite Formation were exposed to increasingly higher degrees of metamorphism toward the contact with the Mafic Complex and, importantly, are increasingly depleted in the granitophile elements with increasing degree of metamorphism (Schmid, 1978/1979; Schmid and Wood, 1976). Together, the IVZ and the Serie dei Laghi are thought to represent an uplifted cross-section through the continental crust (Fountain, 1976; Mehnert, 1975).

DEHYDRATION MELTING

The melting relationships used in this model are that of the fluid-absent (dehydration) melting of metapelitic rock. Dehydration melting is defined as the melt reaction that occurs when all of the water in the system is initially contained within the hydrous mineral assemblage and is transferred directly to the melt during the melting reaction without ever appearing as a product or reactant (Rushmer, 1991). There are numerous studies which underline the importance of this process for crustal growth and evolution (Beard and Lofgren, 1989; Brown and Fyfe, 1970; Thompson, 1982; Whitney, 1988; Yardley, 1986). We choose to focus on dehydration melting in this study because it has been suggested as: (i) a major source of contamination to intruding mafic magmas (Sinigoi et al., 1994), (ii) a source of migmatites and other water-undersaturated granitic melts (Rushmer, 1991), (iii) a cause of some granulite formations (Fyfe, 1973; Mehnert, 1968; Wickham, 1987), and (iv) a source of melts of tonalitic to trondhjemitic composition (Rushmer, 1991).

METHODOLOGY

GENERAL NATURE OF MELT MOVEMENT

A region undergoing melting is essentially a solid-liquid mixture with multiple phase changes. Unlike a pure substance, there is not a distinct crystallization front, rather the solid melts over a temperature range (Figure 1.1). Mixture theory

provides an approach for the development of the equations describing the transport of energy, mass, momentum, and chemical species. A comprehensive discussion of the theory and derivation of the full set of continuum governing equations is discussed in detail elsewhere and will not be revisited here (Bennon and Incropera, 1987a; Oldenburg and Spera, 1992; Prakash and Voller, 1989). A detailed discussion with regards to the derivation and specific application is given in Barboza (1995). The key feature of the mixture theory approach is that it explicitly allows for the full range of dynamic conditions, from porous media flow at low melt fraction to fully liquid behavior at high melt fraction.

The melt fraction at which the solid skeleton breaks down and the flow regime changes from one of porous flow to that of viscous flow with suspended solids is the critical melt fraction (CMF). The fraction of melt is less than the CMF in the region of porous flow where the solid skeleton is fixed relative to the percolating interstitial melt. A wide range of estimates for the CMF of a number of compositions are available. Experimental deformation of partially molten granite yields estimates of $CMF \approx 25-30\%$ (Arzi, 1978; van der Molen and Paterson, 1979). Estimates based on the distribution of the phenocryst content of erupted lava and theoretical arguments based on contiguity limits yield more conservative estimates of $CMF \approx 50\%$ (Marsh, 1981; Miller et al., 1988). However, the experiments of Rutter & Neumann (1995) produced no sharp discontinuity in strength with increasing melt fraction. In light of this result, we have used a ramping, switching function, to model the transition in drag from Darcy dominated drag to suspension dominated drag. Hence the transition from

Darcy dominated to suspension dominated flow did not occur at a distinct value of the CMF. References to the CMF in this study should, therefore, be understood to be a reference melt fraction at which the transition to suspension dominated flow is initiated, not as indicating an abrupt transition in rheology. Other rheological models could have been chosen, our choice reflects a best estimate taken from current experimental results. The permeability in the region of porous flow was calculated using the melt fraction in the Blake-Carmen-Kozeny relation.

Melt movement in both the porous flow and viscous flow regime was initiated by buoyant instabilities that arise from variations in the density of the melting pelite. These density changes are strongly dependent on the distribution of suspended solids, the melt composition, and the temperature. The magnitude of the buoyancy force resulting from these density changes is incorporated in the thermal and solutal expansion coefficients in the buoyancy source term for the momentum equation. The expansion coefficients were derived from the experimental data with calculations using the MELTS algorithm (Ghiorso and Sack, 1995).

The melt viscosity was calculated from the experimental data by the Shaw model (Shaw, 1972) and the Krieger and Dougherty relation was used to account for the influence of suspended solids (Bergantz and Dawes, 1994; Oldenburg and Spera, 1992; Wildemuth and Williams, 1984). As with permeability, a switching function has been incorporated in the viscosity relation to ensure that the influence of suspensions does not impact the effective viscosity in the region of porous flow (Oldenburg and Spera, 1992). Figure 1.3 depicts the kinematic viscosity as a function

of melt fraction for the melt and for the magma (melt + solid suspensions). The temperature and composition dependence of the viscosity of the melt was calculated from the experimental melt compositions and temperatures as a function of the observed melt fractions and, therefore, assumes equilibrium melting (Vielzeuf and Holloway, 1988). Melt viscosity is constant between melt fractions of 0.15 and 0.5 because the melt generated within this range takes place at the biotite dehydration invariant point so temperature and composition do not change. The large increase in effective viscosity just above the CMF approximates the influence of suspended solids on the viscosity of the magma during viscous flow. Although the Krieger and Dougherty relation yields excellent agreement with experimental data (Wildemuth and Williams, 1984), recent work has demonstrated that, under some conditions, the Shaw model may overestimate the viscosity of a silicate melt by up to 2 orders of magnitude (Schulze et al., 1994). Thus, the model simulations were conducted using the entire range of proposed felsic melt viscosities.

THERMODYNAMIC MODEL

The modeling strategy adopted in this study is that of mixture theory where the multi-phase governing equations are averaged yielding a single set of governing equations for the melt/restite mixture. Closure of these governing equations for the solid-liquid mixture requires additional thermodynamic functions to link the

enthalpy and composition to the melt fraction. By assuming local equilibrium, the phase diagram provides the needed relationships.

The dehydration melting of both muscovite and biotite (neglecting the influence of biotite solid solution) takes place at invariant points. The composition of the melt produced at these invariant points will remain constant as long as the restitic phases are in equilibrium with the invariant point melt composition. In addition, excess alumina and mafic oxides have very low solubilities in melts dominated by the orthoclase and H₂O components. The particular mica composition undergoing melting will, therefore, influence the composition of the restitic phases but have only a limited influence on the composition of the melt (Patiño Douce and Johnston, 1991). Since the composition of the melt produced during the dehydration melting of either mica is approximately the same, the melt generated at either invariant point and the suite of resulting restite compositions define a line within the compositional volume. Removal of this melt will cause the composition of the remaining unmelted restite to evolve linearly (Patiño Douce, personal communication) and a simple pseudo-binary phase diagram may capture much of the melting systematics of many pelitic rocks. Errors in melt fraction estimates resulting from the above approximation will be minimal at the relatively low temperatures of interest where the refractory phases are not involved in the melting reaction. In addition, smaller errors are expected for pelite compositions in which melting occurs dominantly at one or the other of the invariant points.

The pelite composition used in the experiments of Vielzeuf and Holloway (1988) was selected as our model composition. Three benefits are obtained by choosing this particular pelite. First, as discussed above, errors in the predicted melt composition will be minimized with when most of the melting occurs at an invariant point. Second, this composition is optimal for melt production. By “optimal”, we mean that this composition produces more melt at lower temperatures than most naturally occurring crustal rocks (Bergantz and Dawes, 1994). This composition thus provides a useful end-member for evaluating the general dynamics of melt-production and extraction in the lower crust. Finally, the composition corresponds reasonably well to the average metagreywacke composition found in the Kinzigite Formation of the IVZ (Schnetger, 1994). The major difference in mineralogy is that the Kinzigite Formation metagreywacke contains 6% K-feldspar and 3% muscovite whereas the experimental pelite composition contains 0% and 9% respectively of these minerals.

Building the binary

The first step in the thermodynamic parameterization is to build a pseudo-binary from which to generate liquid fraction and composition data. The 10 kbar NKM ($\text{Na}_2\text{O}\cdot\text{Al}_2\text{O}_3 - \text{K}_2\text{O}\cdot\text{Al}_2\text{O}_3 - \text{MgO} + \text{FeO}$), silica, alumina, titania saturated pseudoternary (Figure 1.4) was chosen on which to plot the experimental melt compositions. The phase relations, invariant points, and cotectics were derived by Patiño Douce and Johnston (1991) using their own data with those of Vielzeuf and

Holloway (1988) and Le Breton and Thompson (1988). We observe that the suite of melt compositions along with the invariant points form an approximately linear array across this pseudo-ternary. Our methodology was to extend a binary from the M apex of the pseudo-ternary through the array of compositions and invariant points to the intersection with the N-K join (M'). The experimental melt compositions and derived invariant points were then projected onto the binary join and composition was parameterized as a fractional distance along the pseudo-binary. The liquidus line was constrained by the projected experimental melt compositions and the temperatures at which they were generated. The solidus line was derived using the lever rule by fitting the variation of liquid fraction with temperature observed in the experiments and calculated from mass balance to that predicted by the model (Figure 1.5).

MODEL DESCRIPTION

We consider melting of a sequence of pelitic rocks in the two dimensional, 5 km x 5 km computational domain overlying the contact with a sill of basaltic magma in the lower crust. The geometry of the sill underlying the computational domain was based on current estimates of the sill width during emplacement of the Mafic Complex at the IVZ (Quick et al., 1994). The sill was stipulated to be 2 km in width and long enough that the important features of the convection could be captured in two dimensions (Figure 1.1). No assumption was made about the sill thickness except that it contained enough basaltic magma to

maintain the contact temperature throughout the duration of the simulations. This will be addressed in more detail below.

The computational domain was oriented such that the right wall was parallel to the vertical plane of symmetry of the sill (Figure 1.1). The results, thus, depict melting in a semi-infinite half-space over one limb of the intruding sill. A 65 x 65 variable spaced grid was employed and the domain was separated into regions for the purposes of grid point distribution. The highest density of nodes was placed in a 2 km x 2 km region surrounding the simulated contact with the sill. All simulations were halted prior to the melting front leaving the region of higher resolution grid spacing. A grid refinement study was also undertaken to ensure that the solutions were independent of spatial and temporal grid spacing.

At time $t=0$, the temperature along the base of the computational domain up to 1 km from the right hand wall was elevated to a value of T_{contact} , simulating the intrusion of a 2 km wide sill of underplating mafic magma. The contact temperature was maintained through the duration of the simulations. The other walls of the domain were insulated, but all simulations were halted before an appreciable increase in temperature (1-5 °C) was observed at the roof or left wall. This ensured that the thermal boundary conditions did not significantly influence the solution. No-slip boundary conditions were employed on the left wall, roof, and floor. Free-slip conditions were permitted on the right wall as it was the axis of symmetry of melt movement.

The material in the domain was initially the unmelted fertile pelite composition of Vielzeuf and Holloway (1988). The initial pressure and temperature in the domain was 10 kbar and 600 °C - about 150 °C below the solidus of the model composition pelite and corresponding to the approximate depth at which the Mafic Complex was likely intruded (Zingg, 1983). These conditions correspond to a relatively high continental geotherm (17 °C/km), but are similar to predicted geotherms for modern candidates for underplating such as in NE Japan and the Rio Grande Rift (Hyndman, 1981; Kay and Kay, 1980). Two sets of simulations (Case 1 and Case 2) were performed using different contact temperatures (T_{contact}) over the range of estimates for these rheological parameters. A summary of the different combinations of T_{contact} and rheological parameters used in the simulations is given in Table 1.1 along with the other model thermo-physical properties.

RESULTS AND DISCUSSION

THERMAL EVOLUTION AND THE DISTRIBUTION OF MELT ABOVE THE UNDERPLATING SILL

The vigor of convection and, thus, the amount of melt produced in the pelite was found to be strongly dependent on T_{contact} and the combinations of values for the rheological parameters of the system (CMF and $\frac{\mu^\ell}{\mu_{\text{Shaw}}^\ell}$). Note that $\frac{\mu^\ell}{\mu_{\text{Shaw}}^\ell}$ is simply the viscosity of the melt used by a particular simulation divided by the viscosity predicted by the Shaw model. A simple way of evaluating the convective

vigor is by monitoring the evolution of the melt distribution in the partially molten pelite above the sill and by comparing the melt distribution for simulations with different values of T_{contact} and the rheological parameters. We use profiles of the melt distribution rather than the total mass of melt to emphasize the field comparison because the model pelite composition exhibits large jumps in melt fraction which correspond with the disappearance of easily recognizable minerals from the assemblage. The profiles are monitored along the right wall of the computational domain and three cases are presented for comparison (Figure 1.6). Plot A is a Case 1 ($T_{\text{contact}} = 1000 \text{ }^{\circ}\text{C}$) simulation in which the convection was observed to be vigorous relative to the other simulations. Plot B (Case 1) and Plot C (Case 2) are both simulations in which convection was suppressed. The sharp increase in melt fraction furthest from the contact with the sill on the plots in Figure 1.6 is muscovite dehydration. The second large increase in melt fraction closer to the contact is biotite dehydration. The spatial position of the muscovite-out (ms) and biotite-out (bt) transitions are labeled on Plot B.

Note that in the Case 1 simulations, the distance the biotite-out transition had propagated from the contact was strongly dependent on the presence of convection. The distance the muscovite-out transition had propagated, on the other hand, was relatively unaffected by advective transport of heat through most the duration of the simulations. For instance, in the presence of convection after 3.5×10^4 yrs (Plot A in Figure 1.6) muscovite was no longer stable in the assemblage at a height of about 1.6 km above the contact with the sill. The position of the muscovite-out

isograd is about 1.1 km in the conduction case - only 0.5 km closer to the contact. The biotite-out transition, on the other hand, had propagated 1.2 km from the contact with the intrusion in the convective case (Plot A) while only 0.4 km in the conduction case (Plot B). We conclude that, in the field, the muscovite-out transition will probably lie relatively close to a conductive isotherm whether or not buoyancy driven melt movement was an important component of the thermal evolution of the region surrounding many intrusions.

In the IVZ, the muscovite-out isograd lies approximately 1 km stratigraphically above the contact with the Mafic Complex (Zingg, 1980) in the vicinity of what is believed to be the locus of the intrusion (Quick et al., 1994). The simulations demonstrate that, even with the lowest rates of heat flux to the country rock overlying the sill (Plot C), the muscovite-out transition will propagate 1 km after only 3.5×10^4 years. The exposed portion of the Mafic Complex south of Val Strona di Omega covers an area of over 350 km² (Figure 1.2) and geophysical studies indicate that the complex may project many tens of kilometers into the crust (Giese, 1968; Kissling, 1980; Zingg, 1983). These observations appear to require the unlikely combination of extremely high magma supply rates to the mafic complex (higher than $0.4 \frac{\text{km}^3}{\text{yr}}$) coupled with limited heating of the overlying country rock as indicated by the relatively short distance the muscovite-out transition propagated from the contact. For comparison, estimates of the average effusion rates for Hawaii and the Columbia River Basalt Group are on the order of $0.1 \frac{\text{km}^3}{\text{yr}}$ (Swanson et al., 1989). We believe

that it is more likely that the temperature of the overlying country rock reached a steady state temperature lower than one might expect given the volume of magma that made up the Mafic Complex. This indicates that magmatism during the emplacement of the Mafic Complex was probably episodic punctuated by long periods of stagnation.

CONVECTIVE VELOCITIES AND THE RHEOLOGICAL AND THERMAL ENVELOPE OF CONVECTION

A more rigorous evaluation of convective vigor was undertaken by monitoring the time evolution of the heat absorption ratio (H_{abs}). H_{abs} is defined as the total amount of latent and sensible heat absorbed by the system (H_{conv}) in the presence of convection relative to that calculated by a simulation performed under the same conditions in which the heat transfer was forced to occur by conduction only (H_{cond}).

$$H_{abs} = \frac{H_{conv}}{H_{cond}} \quad (1.1)$$

For the purposes of discussion, simulations in which $H_{abs} = 1$ were termed “conduction dominated” as conduction was the dominant mode of heat transfer in the system. Simulations in which $1 < H_{abs} < 2$ were termed “convection influenced” and those in which $H_{abs} \geq 2$ were termed “convection dominated” as the heat transfer in the presence of convection was at least twice that of conduction alone.

Convective velocities in all simulations in Case 1 and Case 2 were variable, but generally small. Maximum convective velocities in the region of porous flow were on the order of $1 \times 10^{-7} \frac{m}{yr}$ and porous flow transported an insignificant amount of heat. Maximum convective velocities in the region of viscous flow, on the other hand, were on the order of $1 \times 10^{-1} \frac{m}{yr}$. Viscous flow was thus sufficient, in some simulations, to influence the thermal evolution. H_{abs} larger than 5 were observed for simulations in which the rheological parameters were optimum for convection ($\frac{\mu'}{\mu_{Shaw}} = 0.01$, $CMF = 0.35$) in Case 1. Convective vigor, however, was dramatically less in Case 2 simulations where the contact temperature was lower (900 °C). In addition to the contact temperature the influence of convection was observed to be a strong function of time, the CMF, and the viscosity.

Influence of the rheological parameters on convective vigor

The influence of the contact temperature and rheological parameters on convective vigor can be illustrated by plotting H_{abs} over the range of estimates of the viscosity and the CMF 1×10^4 years after the initiation of the simulations (Figure 1.7). Convective velocities high enough for the contact metamorphism to be convection influenced are restricted to a limited range of estimates of the melt viscosity and CMF. More conservative estimates of these parameters tended to yield conduction dominated solutions for all simulations in either case. The maximum magnitude of convective velocities observed was approximately $1 \times 10^{-1} \frac{m}{yr}$, but more commonly,

maximum magnitudes were between 1×10^{-5} - $1 \times 10^{-3} \frac{m}{yr}$. Note in particular the dramatic decrease in convective vigor when the contact temperature was 900 °C. Convection influenced the thermal evolution of only those Case 2 simulations with the most optimal estimates of the rheological parameters ($\frac{\mu^t}{\mu_{Shaw}^t} = 0.01$ and CMF = 0.35). The contact temperatures used in the simulations (1000 °C and 900 °C) are probably higher than in natural systems, so the weak convection observed in these simulations is probably more vigorous than to be expected in natural underplating regions. In general, buoyancy driven convective stirring of a restite charged, partially molten pelitic sequence is unlikely to occur. Such convection appears to require both extreme conditions of sustained, high-temperature magmatism and more optimal estimates of the rheological parameters.

Evolution of convective vigor with time

It is also informative to measure the time that elapsed before H_{abs} exceeded 1.0. We termed that period the “convective rise time” and it was found to be strongly dependent on both the rheological parameters (viscosity and CMF) and the contact temperature ($T_{contact}$). Convective rise times were typically on the order of 1×10^3 yrs for Case 1 and substantially longer ($2-6 \times 10^4$ yrs) for Case 2 (Figure 1.7). These estimates should be taken as the minimum amount of time the contact temperature must be maintained to establish convection with sufficient vigor to influence the regional thermal evolution. Thus, not only does vigorous convective

stirring of the partially molten pelite require high contact temperatures and optimal estimates of the rheology, but it also requires a contact metamorphic event of significant duration. Buoyancy driven viscous flow of partially country rock is likely to be isolated to regions experiencing long periods of sustained magmatism.

The minimum mass of basalt required to maintain the contact temperature through the duration of the convective rise time may be estimated assuming that the composition of the basalt was that of a typical MORB and was intruded at a temperature of 1200 °C and cooled to the contact temperature (1000 °C or 900 °C). Latent heat released during crystallization through this temperature range was accounted for by estimating the percent crystallization of the basalt with the MELTS algorithm (Ghiorso and Sack, 1995). The mass of basalt was calculated by equating the amount of heat absorbed by the country rock to that released by the simulated intrusion (Figure 1.7). These values should be regarded as minimum estimates of the mass of basalt. In evaluating Figure 1.7, one might consider a sill about the dimensions of recent estimates of the size of mid-ocean ridge magma chamber (Sinton and Detrick, 1992). If one assumes a sill 2 km in width and a thickness of 100 m, it contains approximately 3×10^8 kg of basalt per meter of sill width in each limb. Cooling this amount of basalt would not yield the minimum amount of energy required to initiate viscous flow during the course of any simulation.

An application to the Ivrea-Verbano Zone

Temperatures of between 750 - 800 °C have been estimated for the kinzigites and stromalites in the IVZ (Sills and Tarney, 1984; Zingg, 1983). It should be noted that these estimates place the temperature of the kinzigites close to that of the biotite dehydration reaction (I2). Although the kinzigites near the contact with the Mafic Complex in Val Sesia have probably undergone a large degree of partial melting (Zingg, 1980), they commonly retain a significant amount of biotite. In addition, the maximum temperatures estimated for the paragneisses in the Kinzigite Formation is on the order of 850 °C (Zingg, 1983). It is thus unlikely that contact temperatures between the Kinzigite Formation and the underlying Mafic Complex were as high as 1000 °C or 900 °C for significant periods of time. If the melting systematics of the model pelite are representative of the melting of a typical IVZ metagreywacke, the simulations indicate that it is likely that heat transport in both the kinzigites and stromalites was dominated by conduction and convection played a limited role in the transport of heat. In addition, given the relatively low temperatures indicated by the thermometry and the extremely limited convection observed in Case 2 ($T_{\text{contact}} = 900 \text{ °C}$) simulations, conduction is likely the case whether or not enough melt was produced to exceed the CMF.

MELT EXTRACTION

Convective velocities in the region of porous flow were insufficient to drive significant melt extraction during the course of any simulation. Maximum convective velocities observed in the region of viscous flow were about $1 \times 10^{-7} \frac{m}{yr}$. The simulations were conducted over a period of 10^5 years so the maximum distance melt migrated from the source during the course of the simulations was on the order of centimeters. Given that the duration of a typical crustal melting event is on the order of 10^5 - 10^7 years (Sawyer, 1994), the *maximum* distance that melt could be expected move within a partially molten pelite overlying a sill is probably less than a meter. These velocities are a maximum estimate because the contact temperature was held constant throughout the simulations. This cannot be the case in a natural underplating sill because, among other reasons, basalt would be nearly solidified and cooling conductively at 900 °C and 10 kbar. The observed convective velocities are thus an end-member estimate of the natural system. In conclusion, the simulations indicate that the buoyancy of the melt alone is not sufficient to drive a significant extraction of melt from the porous skeleton. Deformation, fracturing or both may be the dominant mechanism for melt extraction in the continental crust and that buoyancy-driven porous flow is, at best, a second-order process.

The existence of a low melt fraction window of extractable melt

In cases where melt extraction at low melt fraction (Sawyer, 1991) is determined to be significant, it is possible to estimate from which region melt is most likely to be extracted. Given the nonlinear variations in the viscosity (Figure 1.3) of the melt residing within the porous skeleton, however, the propensity for melt extraction is unclear. Darcy's Law implies that the propensity for melt extraction under a given pressure gradient can be estimated from the ratio of the permeability of the porous medium to the viscosity of the melt ($\frac{k}{\mu}$) if melt movement is pervasive. Higher values of $\frac{k}{\mu}$ would indicate a higher propensity for melt extraction and $\frac{k}{\mu}$ should be directly proportional to the differential velocity between the melt and porous skeleton. A two order of magnitude increase in $\frac{k}{\mu}$ thus indicates a two order of magnitude increase in average differential velocities. A plot of $\frac{k}{\mu}$ with liquid fraction using the model permeability and viscosity relationships is shown in Figure 1.8.

Melt existing in regions of a partially molten pelite that possess a melt fraction between 0.05 and 0.15 appears to have a relatively high propensity to undergo melt movement. In fact, the $\frac{k}{\mu}$ value predicted to exist within this melt fraction range is not exceeded until the system reaches a melt fraction of nearly 0.35. This melt fraction range was also correlated with a peak in the magnitudes of convective velocities in all simulations. Although the observed velocities were extremely small ($1 \times 10^{-7} \frac{m}{yr}$), the pressure gradient that generated the melt movement was due solely to

the buoyancy of the melt and neglected other possible modes of transport. If, for example, diking were to occur in the region, the velocity of the melt in the porous skeleton might be much higher. In such a circumstance we postulate that the melt existing in the range of melt fraction between 0.05 and 0.15 is the most likely to be extracted barring the accumulation of a substantial percentage of melt (>40%) in the region.

CONCLUSIONS AND SUMMARY

Phase relations for the dehydration melting of pelitic rocks have been parameterized for use in a thermo-mechanical model. Numerical simulations of the dehydration melting and subsequent buoyant melt migration of a sequence of pelitic rocks following the underplating of mafic magma in the lower crust have been performed. The total amount of melt produced is critically dependent on the dynamics of melt movement in the pelite/melt mixture.

Important factors influencing the vigor of melt and melt plus restite movement are the value of the critical melt fraction (CMF), viscosity, and the temperature of the igneous contact. Recall that the CMF, as used in this study, does not provide an abrupt transition from porous dominated to suspension dominated drag. Instead, the CMF is a reference value for the initiation of this transition. Simulations in which conservative estimates of the $CMF \approx 0.5$ and the melt viscosity calculated by the Shaw model were used tended to yield conduction-dominated solutions. Other

estimates of the melt viscosity yielded weak convection that influenced the thermal evolution of crustal rocks to a varying degree.

The simulations demonstrate that vigorous convective stirring in the region of viscous flow and a significant amount of melt extraction within the porous skeleton will probably not occur except under extreme conditions (i.e.; long, sustained periods of magmatism; large amounts of very high temperature magma. Kilometer-scale buoyancy-driven convective stirring is, in general, unlikely to occur given current rheological models and heating rates. In addition, buoyancy-driven extraction of melt at low melt fraction appears to be a second-order process. Shear, extensional fracturing, or some other mechanism appears to be required to achieve significant melt extraction.

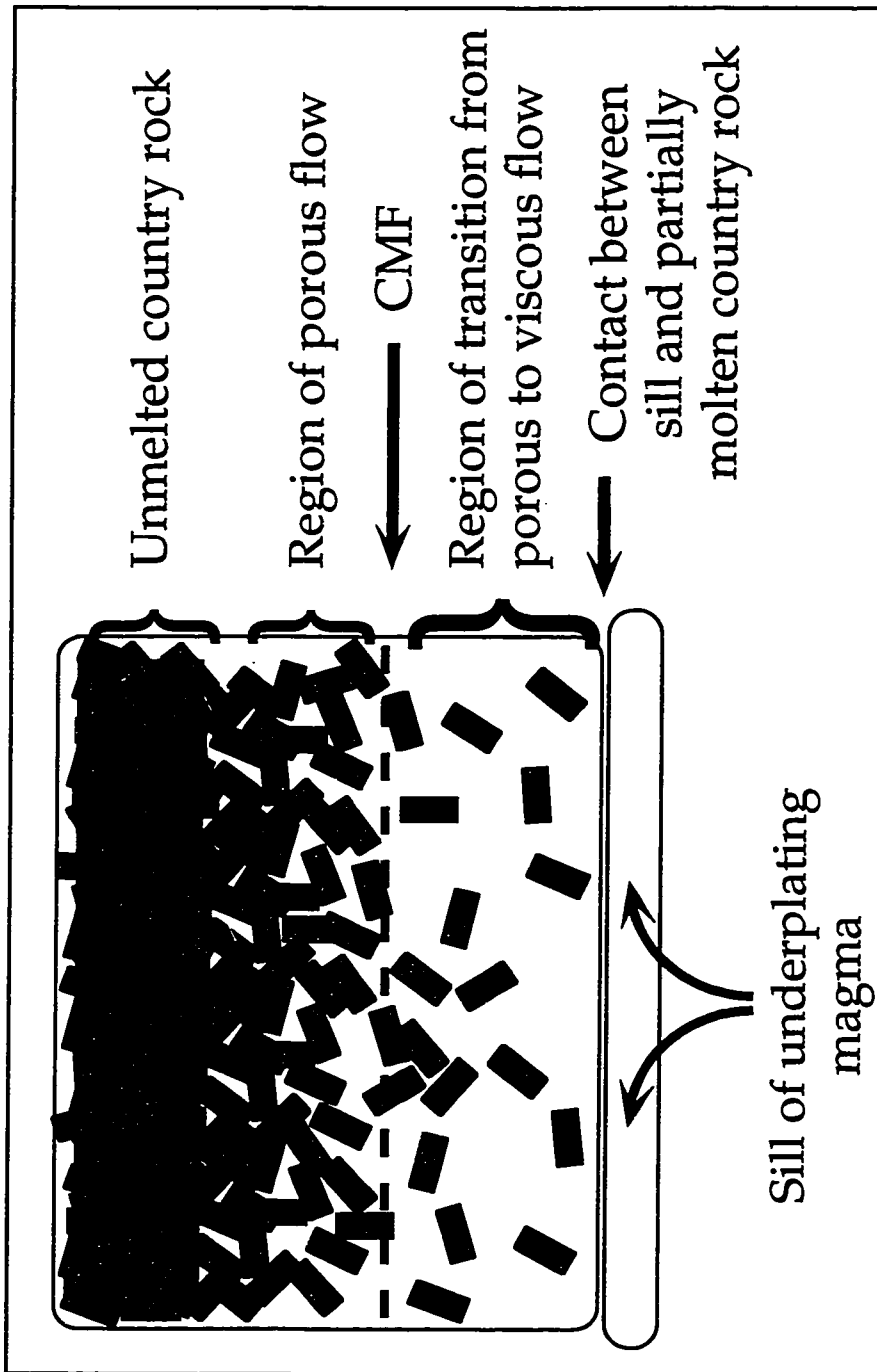


Figure 1.1. Schematic diagram for melting model. A sill of mantle-derived magma is intruded at the base of a sequence of pelitic rocks. Heat transfer to the sequence causes the melting of the pelitic rocks and results in buoyant instabilities in the pelite/melt mixture. These instabilities cause the upward flow of material from the region near the contact with the sill, further enhancing the heating and melting of the pelitic sequence above. When the local volume fraction of melt exceeds the CMF, the rheological transition between the porous and viscous flow end-member regimes is initiated.

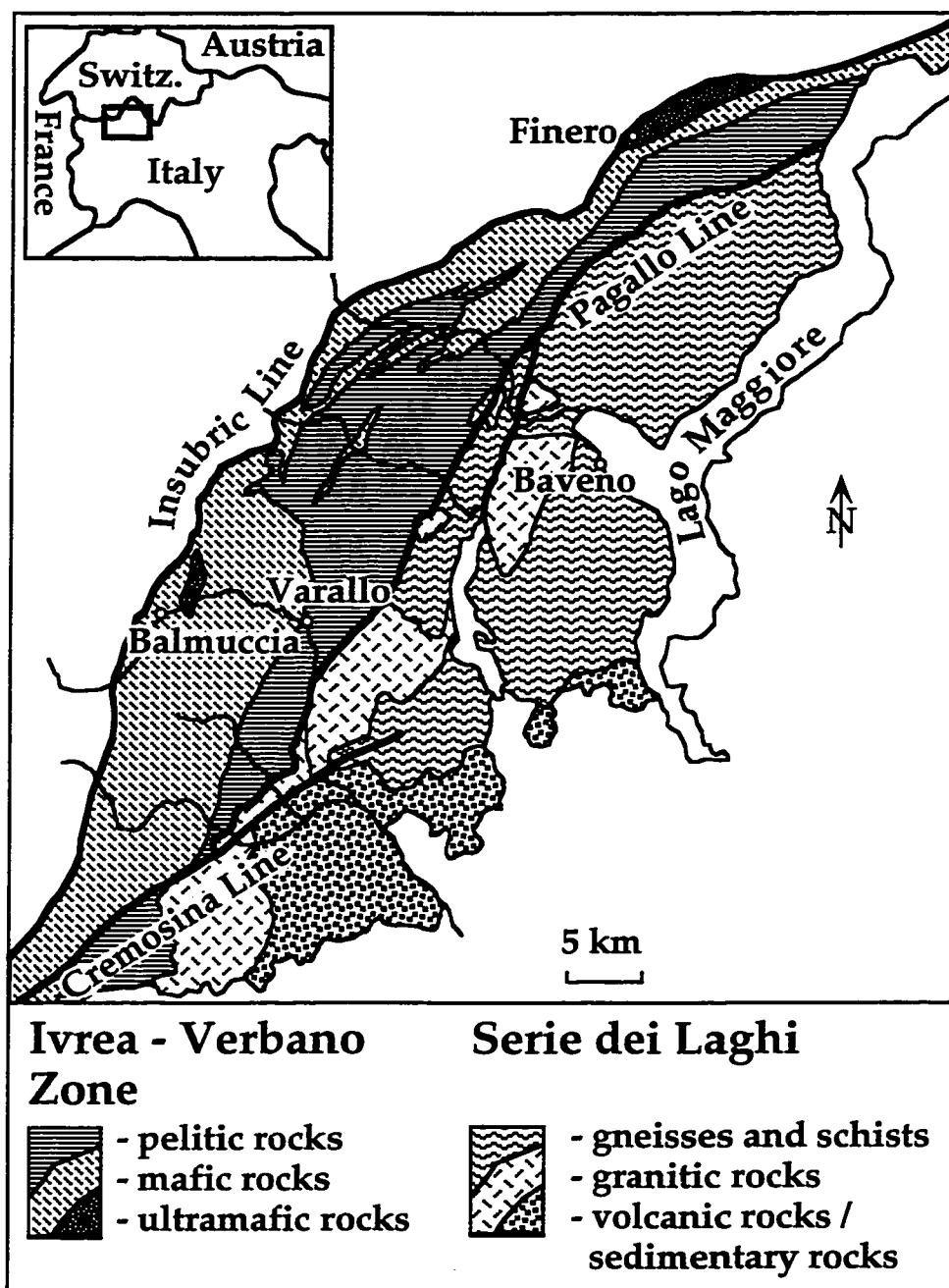


Figure 1.2. Geologic sketch map of the Southern Alps west of the Lago Maggiore (modified from Zingg, 1980). Inset shows location of area in northern Italy.

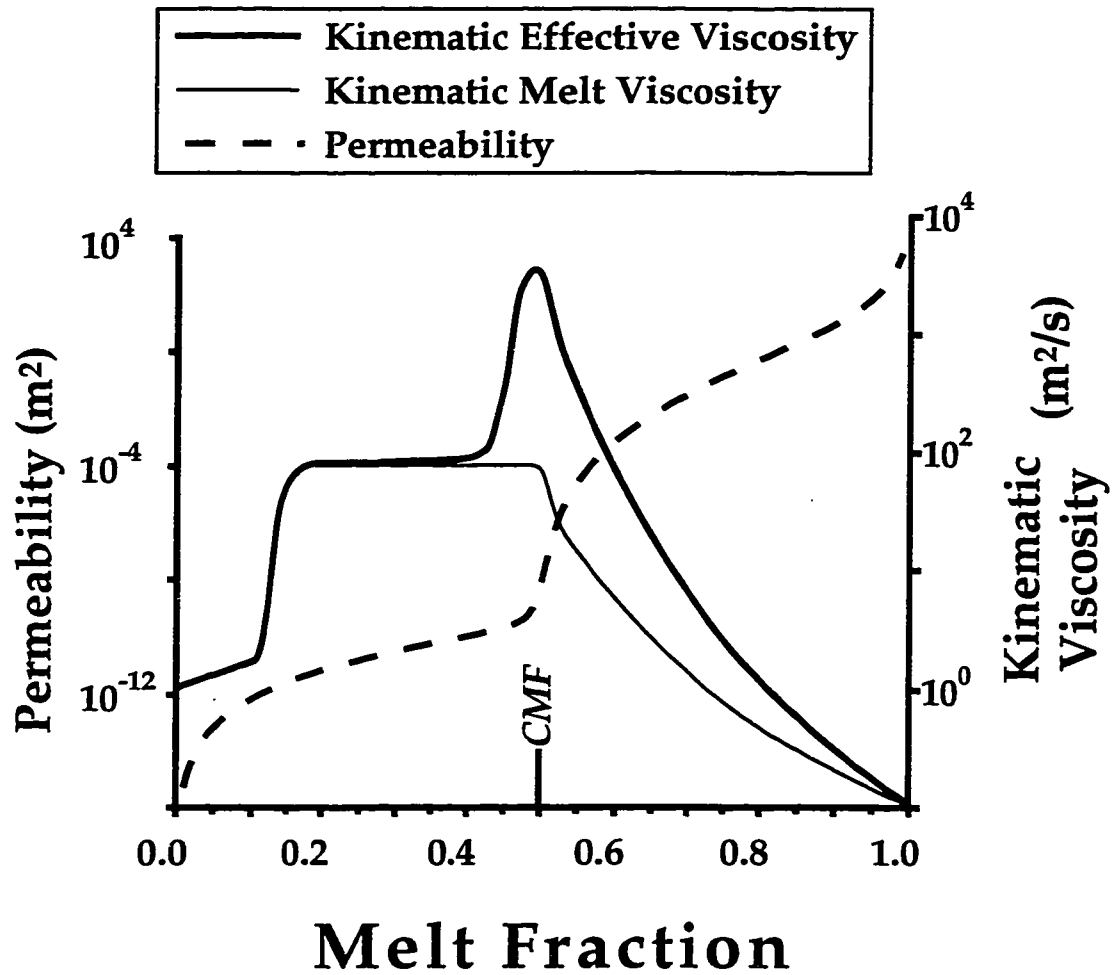


Figure 1.3. Plot of the model relationships of the kinematic viscosity and permeability as a function of the melt fraction. The light solid curve gives the variation of the viscosity of the melt only and the heavy solid curve is the model mixture viscosity which includes the influence of suspended solids. The low viscosities at low melt fractions arise because of the high water content of the experimental melts (Vielzeuf & Holloway, 1988). The critical melt fraction (CMF) is the melt fraction at which the transition from porous to viscous flow is initiated. Shaded region highlights the transition region. The CMF, in this case, is 0.5. Simulations using different values for CMF had qualitatively similar relationships.

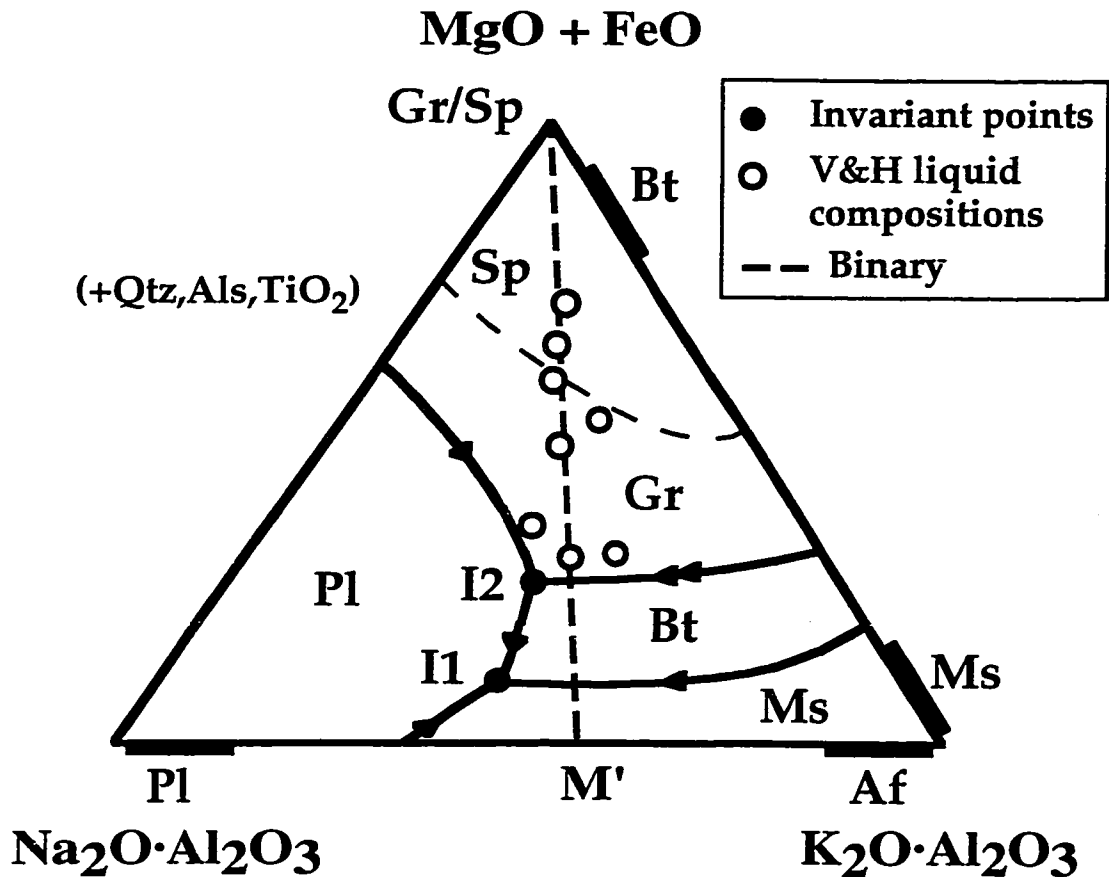


Figure 1.4. 10 kbar NKM silica, alumina, and titania saturated pseudo-ternary liquidus phase relations projected from the KNMH volume (Patiño Douce and Johnston, 1990). Filled circles are the biotite dehydration invariant point (I2) and the muscovite dehydration invariant point (I1). Open circles are the projections of the Vielzeuf and Holloway (1988) experimental liquid compositions. Heavy dashed line is the pseudo-binary used in the model. Mineral abbreviations are as follows: Sp=spinel; Gr=garnet, Pl=plagioclase feldspar; Af=alkali feldspar; Ms=muscovite; Qtz=quartz; Als=aluminosilicate; Bt=biotite.

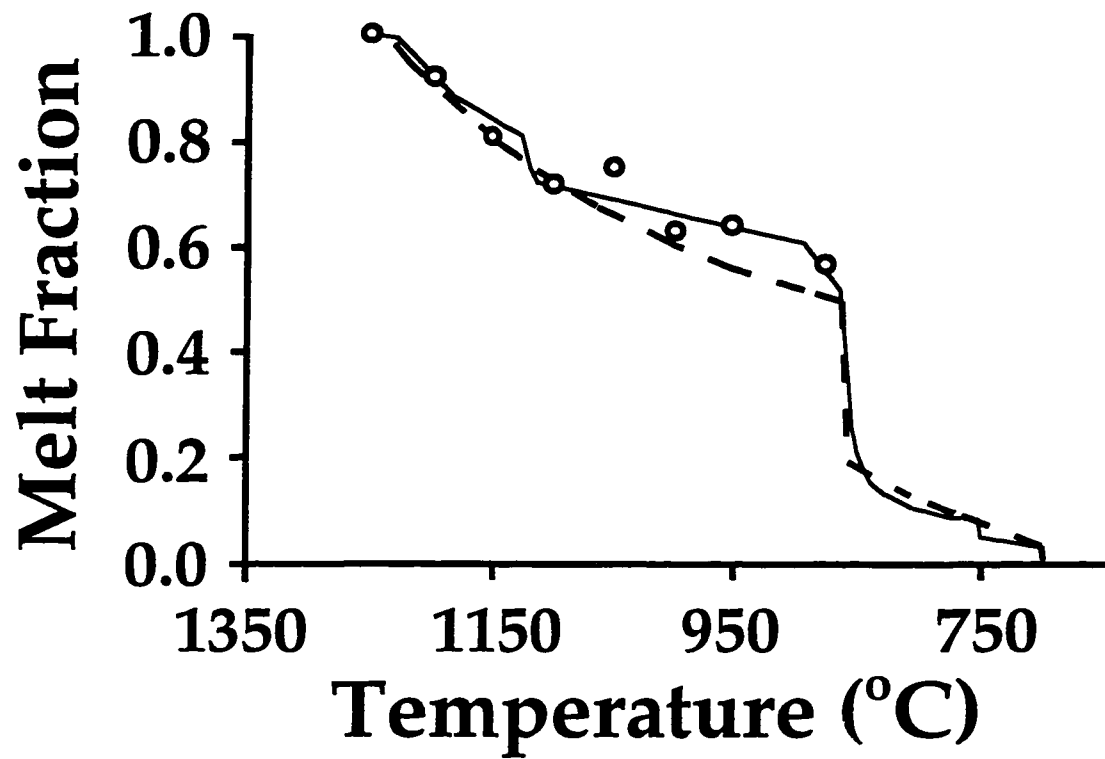


Figure 1.5. Predicted variation of melt fraction as a function of temperature using a lever rule formulation and the pseudo-binary phase relationships depicted in Figure 5. Dashed line is the model melt fraction curve, the solid line is that calculated by Vielzeuf and Holloway (1988) using inferred melting relationships, and the open circles are the melt fractions observed in the melting experiments (Vielzeuf and Holloway, 1988).

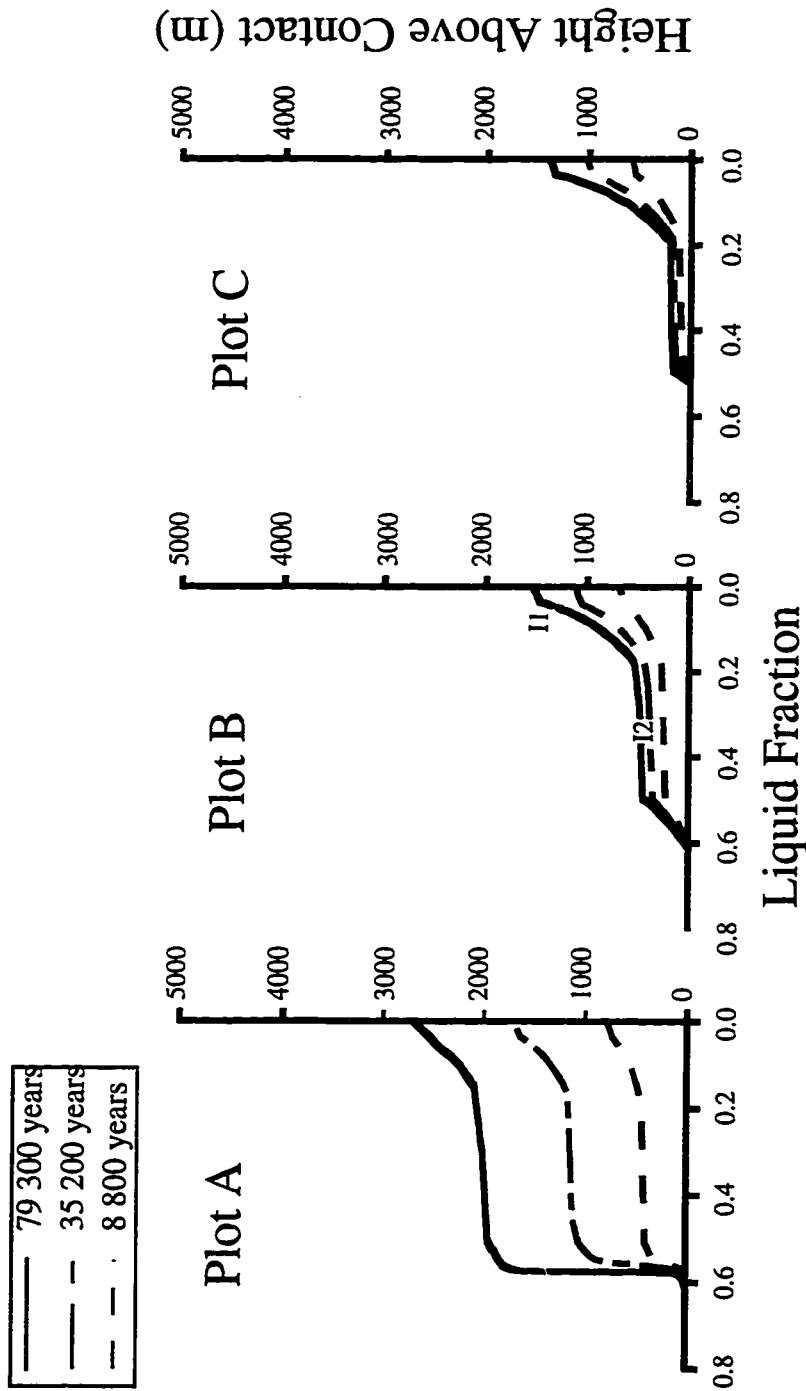


Figure 1.6. Evolution of melt distribution. Plot A is a plot of the distribution of melt within the pelite/melt mixture with height above the apex of the underplating sill during a convection-dominated simulation. Plot A is a Case 1 simulation (see text) in which $\text{CMF} = 0.1$ and $\text{CMF} = 0.45$. Three curves are shown Plot A depicting the melt fraction at different times during the simulation. Plot B and Plot C are conduction-dominated simulations from Case 1 and Case 2 respectively. The sharp increase in melt fraction furthest from the contact is the location of the muscovite melting reaction (I1). The second large increase in liquid fraction closer to the contact is that of the biotite melting reaction (I2). Abbreviations: CMF = critical melt fraction; is the viscosity used in a particular simulation divided by the calculated viscosity using the Shaw model.

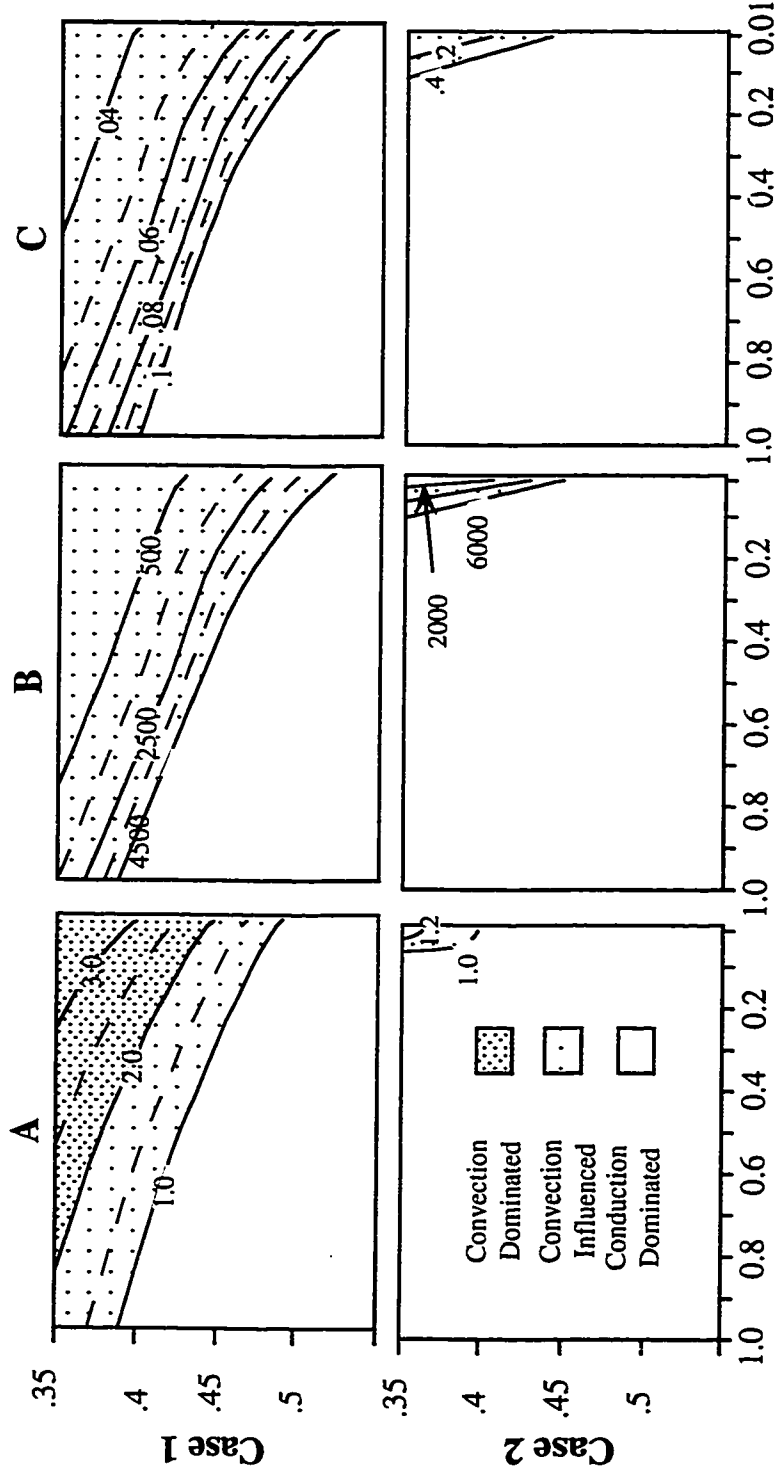


Figure 1.7. Contours of three parameters for Case 1 ($T_{contact} = 1000\text{ }^\circ\text{C}$) and Case 2 ($T_{contact} = 900\text{ }^\circ\text{C}$) simulations. *Plot A.* Contours of the range of heat absorption ratios (H_{abs}) after 1.0×10^4 years. Simulations in which $H_{abs} = 1.0$ were termed "conduction dominated", those with $1.0 < H_{abs} \leq 2.0$ were termed "convection influenced", and those with $2.0 < H_{abs}$ were termed "convection dominated". *Plot B.* Contours of the time (years) the contact temperature must be maintained in order for convection to influence the regional thermal evolution. *Plot C.* Contours of the minimum mass (in $\text{kg}/10^{10}$) of basalt per unit length of sill required for convection in the pelite/melt mixture to influence the thermal evolution of the domain. Abbreviations as in Figure 7.

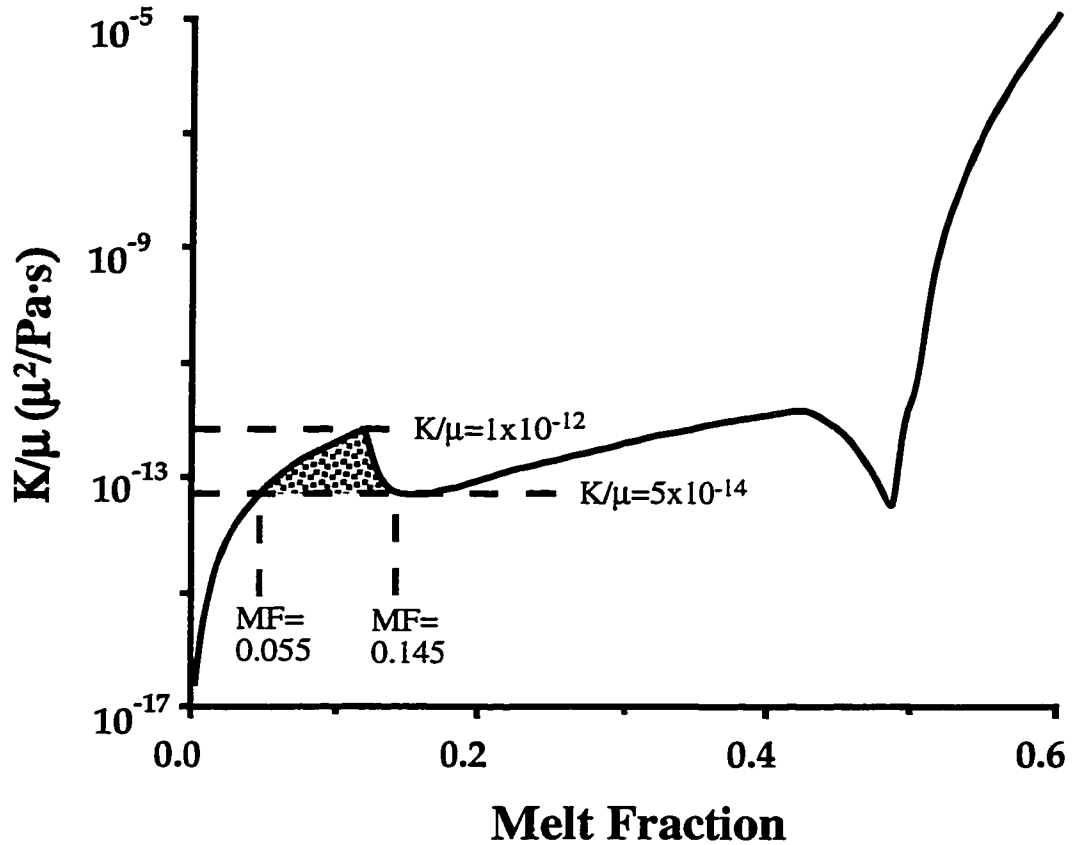


Figure 1.8. Plot depicting the relative propensity for melt movement within the porous skeleton as a function of the melt fraction. Higher values indicate a higher propensity for melt movement. Note that the values reached between melt fractions of 0.05 and 0.15 is not exceeded until after nearly 40% of the pelites has been melted. Shaded region is the "low melt fraction window of extractable melt" discussed in the text. Dashed lines are reference values.

Table 1.1: Data for the model.

| Property (units) | Numerical value |
|--|-----------------------------------|
| Property data | |
| Specific heat ($J/kg.K$) | 1.04×10^3 |
| Thermal conductivity ($W/m.K$) | 1.9 |
| Density (kg/m^3) | 2.507×10^3 |
| Kinematic viscosity (m^2/s) | see text |
| Schmidt number (μ'/D) | 1.0×10^6 |
| Latent heat (J/kg) | 1.0×10^5 |
| Permeability coefficient (m^2) | 5.56×10^{-10} |
| Thermal expansion coefficient (K^{-1}) | 1.05×10^{-4} |
| Solutal expansion coefficient (C^{-1}) | 1.55×10^{-1} |
| Initial conditions | |
| Pelite starting composition | 0.325 |
| Initial temperature ($^{\circ}C$) | 600.0 |
| Contact temperatures and rheological parameters used in simulations | |
| Contact temperature ($^{\circ}C$) | Case 1 = 1000.0 Case 2 = 900.0 |
| Range of CMF | 0.35, 0.4, 0.45, 0.5, 0.55 |
| Range of μ'/μ'_{Shaw} † | 1.0, 0.5, 0.1, 0.01 |

† μ'/μ'_{Shaw} is the ratio of the melt viscosity used in the simulations to that predicted by the Shaw model using MELTS.

CHAPTER 2: MELT PRODUCTIVITY AND RHEOLOGY: COMPLEMENTARY INFLUENCES ON THE PROGRESS OF MELTING

INTRODUCTION

The equations governing the transport of heat and mass in solid-liquid, phase-change systems require thermodynamic functions that link the enthalpy and mixture composition to the local melt fraction (Bennon and Incropera, 1987a). Previous studies have utilized a binary-eutectic phase diagram with a single invariant point and solid solution between the components of the system to provide the necessary equations (Bennon and Incropera, 1987b; Oldenburg and Spera, 1992; Prakash and Voller, 1989). However, the phase-change systematics of naturally occurring rock compositions can be complex. As an example, experimental studies have shown that, as long as feldspar (a tectosilicate) is not a limiting reactant, some rock compositions may exhibit large increases in melt fraction with increasing temperature as the solidi of the phyllosilicates are exceeded (Vielzeuf and Holloway, 1988). This non-linear melt production may have a significant influence on heat and mass transfer as the constitutive equations for the mixture depend explicitly on the melt fraction. However, the effect of the interdependence of melt production and the constitutive equations on heat and mass transfer is poorly understood.

We present a continuum-mixture model for binary systems with two invariant points - a eutectic and a peritectic. Notable features of this numerical study

include variable viscosity and rheological switching functions with melting a natural rock composition. The example simulations illustrate that the dynamics of heat and mass transport in systems with multiple invariant points differ significantly from that of binary-eutectic systems. Thus, caution is urged when applying the results of continuum simulations utilizing binary-eutectic, phase-change models to systems with more complex phase relationships.

CONTINUUM MODEL

This study adopts the two-phase mixture formulation developed by Bennon and Incropera (1987a). The nomenclature referred to in the study is provided in Table 2.1. The interested reader is directed to Prakash and Voller (1989) and Bennon and Incropera (1987a) for a complete derivation and a discussion of the model assumptions. Our formulation differs from theirs in that our model has additional terms in the governing equations that account for the variation of mixture viscosity as a function of temperature, concentration, and solid fraction. Only the final forms of the dimensional equations to be solved are presented here. The variable viscosity form of the mixture continuum-conservation equations for phase change and convection in two-dimensions are:

$$\frac{\partial v_j}{\partial x_j} = 0 \quad (2.1)$$

$$\frac{\partial}{\partial t}(\rho v_i) + \frac{\partial}{\partial x_j}(\rho v_j v_i) = -\frac{\partial p}{\partial x_i} + \frac{\partial}{\partial x_j} \left(\mu' \frac{\rho}{\rho'} \frac{\partial v_i}{\partial x_j} \right) + \frac{\rho}{\rho'} \frac{\partial v_i}{\partial x_j} \frac{\partial \mu'}{\partial x_j} + \quad (2.2)$$

$$g' \gamma_o' g_i \left[\beta_T' (T - T_o) + \beta_C' (C' - C_o') \right] + \frac{\mu'}{K_i} (f' v_i')$$

$$\frac{\partial}{\partial t}(\rho T) + \frac{\partial}{\partial x_i}(\rho v_i T) = \frac{\partial}{\partial x_i} \left(\frac{k}{c_p'} \frac{\partial T}{\partial x_i} \right) - \rho \frac{L}{c_p'} \frac{\partial f'}{\partial t} + \rho \frac{(c_p' - c_p^s)}{c_p'} \frac{\partial}{\partial t} (f^s T) \quad (2.3)$$

$$\frac{\partial}{\partial t}(\rho C) + \frac{\partial}{\partial x_i}(\rho v_i C) = \frac{\partial}{\partial x_i} \left(\rho f' D' \frac{\partial C}{\partial x_i} \right) + \frac{\partial}{\partial x_i} \left[\rho f' D' \frac{\partial}{\partial x_i} (C' - C) \right] \quad (2.4)$$

$$- \frac{\partial}{\partial x_i} [\rho v_i (C' - C)]$$

The influence of microscopic geometry on macroscopic transport is modeled by semi-empirical source terms incorporated with the governing equations. For example, the last term on the right hand side of Equation 2.2 is the Darcy drag source, which accounts for the viscous drag exerted by the solid phase on the percolating interstitial fluid. The term to its left is the buoyancy source that accounts for the density variation of the mixture as a function of temperature and composition gradients. The magnitudes of these density changes are given by the size of the thermal (β_T') and compositional (β_C') expansion coefficients. The method used in determining these coefficients for the model composition is discussed in Barboza & Bergantz (1996). The source terms which appear in the energy and solute conservation expressions (Equations 2.3 and 2.4) account for the enthalpy to temperature relationships and the difference between the diffusion of components

through the solid and the liquid, respectively. Diffusion of species in the solid is taken to be negligible relative to that in the liquid in this analysis. A complete derivation of all of the source terms is given in Prakash & Voller (1989) and Bennon & Incropera (1987a).

In this model formulation, terms such as the Darcy drag source are, themselves, a function of the local melt fraction. However, there is no universal agreement on the most appropriate constitutive relations that span the full range of melt fraction (Beckermann and Viskanta, 1993). At low melt fraction, the melt flows within a rigid solid matrix whose velocity is either fixed (static phase change) or prescribed to be that of free body translation (continuous phase change) (Bennon and Incropera, 1987a). At high melt fraction, bulk viscous flow of the mixture occurs and there is no relative motion between the melt and the suspended solids. We use the model of Oldenburg & Spera (1992) in which arctangent switching functions are employed to shift between the end-member constitutive relations at a stipulated critical melt fraction (CMF). An illustration of this rheological model is shown in Figure 2.1.

We assume the CMF is an abrupt transition in the rheology of the system. At low melt fraction, the rheology of the system is that of a static solid with a percolating interstitial melt, while above the CMF it is of a fluid with suspended solids. Several studies have indicated a CMF of approximately 0.5 for some silicate systems (Marsh, 1981; Miller et al., 1988). However, it is important to acknowledge recent experiments that indicate that the notion of a distinct CMF requires substantial revision for geological systems undergoing partial melting (Rushmer, 1995; Rutter and

Neumann, 1995). Barboza and Bergantz (1996) adopted a ramped switching function where the transition between the end-member transport types was initiated at the CMF to recognize this result. That approach is not adopted in this study because an abrupt rheological transition better illustrates the influence of the thermodynamics of phase change on the dynamics of the system.

The rheological switching functions are incorporated directly into the relationships for permeability and the influence of suspensions on the mixture viscosity. The permeability is related to the local melt fraction by the Blake-Kozeny-Carman equation (Beckermann and Viskanta, 1988a). The melt viscosity is calculated by the Shaw model (Shaw, 1972) and the influence of suspensions is modeled by the Krieger and Dougherty relation (Wildemuth and Williams, 1984). The permeability and viscosity relationships along with their associated switching functions are:

$$K = \Gamma K_o \left[\frac{(f')^3}{(1-f')^2} \right] \quad (2.5)$$

$$\Gamma = \left\{ 0.5 + \frac{1}{\pi} \arctan \left[100 (f'_{crit} - f') \right] \right\}^{-10} \quad (2.6)$$

$$\mu(T, C, f') = \left[1 - \Phi \left(\frac{1-f'}{f'_{crit}} \right) \right]^{-2} \mu'(T, C) \quad (2.7)$$

$$\Phi = 0.5 - \frac{1}{\pi} \arctan \left[100 (f'_{crit} - f') \right] \quad (2.8)$$

The model rheological functions are illustrated in Figure 2.2.

PHASE DIAGRAM

The material chosen for the example calculations is a natural meta-sedimentary rock composition rich in phyllosilicate minerals (metapelite) whose predominate major element composition is within the system KFMASH (SiO_2 - Al_2O_3 - MgO - FeO - K_2O - H_2O). The exact composition and mineralogy is described in Vielzeuf & Holloway (1988). A metapelite was chosen because of its importance in the earth sciences as a potential source of granitic melt (Bergantz and Dawes, 1994). One notable melting feature of this pelite composition is that it exhibits large jumps in melt fraction at two invariant points. The phase relationships were experimentally derived by Patiño Douce and Johnston (1991) using their own data along with that of Vielzeuf and Holloway (1988) and Le Breton and Thompson (1988).

The temperatures and compositions of the melts produced in the experiments and the deduced invariant points were then projected onto a pseudo-binary to derive the model binary phase diagram. The justification, methodology, and assumptions involved in making this projection is provided elsewhere (Barboza, 1995; Barboza and Bergantz, 1996). One should note, however, that the two invariant-point, phase diagram presented below is easily adapted for the phase relationships of any two invariant-point binary system. Some important geological examples include the systems Mg_2SiO_4 - SiO_2 (forsterite - silica), KAlSi_2O_6 - SiO_2 (leucite, silica), and $\text{NaAlSi}_3\text{O}_8$ - $\text{NaAlSi}_3\text{O}_8$ (nepheline - albite).

Closure of the governing equations for the solid-liquid mixture requires additional relations which link the mixture enthalpy and composition to the melt fraction (Bennon and Incropera, 1987a). This information is obtained by assuming local thermodynamic equilibrium and consulting the model phase diagram. Note that macroscopic disequilibrium is not precluded even though local equilibrium is assumed. The procedure for deriving the lever rule expressions for binary eutectic systems have been discussed elsewhere (Prakash and Voller, 1989). However, numerous additional mathematical relationships are required to describe the new phase diagram due to the additional complexity resulting from the presence of a second invariant point (the peritectic). Our approach was to divide the temperature - composition (T-X) space of the phase diagram into regions. Separate univariant (solidus and liquidus) lines with different slopes were then assigned to each T-X region. The values of the parameters required to fix the geometry of the univariant lines and the size of the regions were derived by fitting the observed variation in melt fraction with temperature in experiments (Barboza and Bergantz, 1996) to that predicted by the model. The fit between the model predictions and the experimental observations is illustrated in Figure 2.3. A schematic of the two-invariant point binary used in the simulations is shown in Figure 2.4. The phase diagram terminology and associated equilibrium lever-rule expressions are listed in Table 2.2, 2.3, and 2.4 and the values of the constants are provided in Table 2.5. Although the geometry of this model is considerably more complex than previous phase diagrams, we attempted to maintain consistency with previously used terminology as much as possible (Prakash

and Voller, 1989). Note, however, that much of the adopted terminology no longer has a meaningful physical interpretation and the constants should be regarded only as geometric parameters which define the orientation of the phase diagram in T-X space.

One issue with this approach is the thermodynamic behavior of the system at the invariant points. Specifically, accounting for the transport of heat in phase-change systems requires careful consideration of the influence of phase change at the invariant points on the local temperature due to the isothermal consumption or release of latent heat. However, stipulating a constant temperature and accounting for the latent heat exchange at the invariant points renders a discontinuity in the temperature field and results in difficult numerical instabilities. Our solution was to allow the system to change a few degrees in temperature during invariant point phase change (Figure 2.4). This permits the use of a separate univariant lines for the invariant-point region and lever-rule type expressions may be used to account for the variation of melt fraction with enthalpy exchange. This approach also ensures proper accounting of the transfer of energy through the latent heat of fusion yet prevents discontinuities from appearing in the temperature field. An illustration of the geometry of these relations in the vicinity of the eutectic and peritectic (I1 and I2) is shown in Figure 2.4.

Care must also be taken to ensure a smooth transition between each of the univariant lines for the separate regions. Discontinuities in the overall liquidus or solidus will result in numerical instabilities and convergence is no longer assured. Expressions are therefore required which link the univariant lines from the different

regions. In other words, the univariant lines for the adjacent regions must precisely intersect at the specified temperature and composition at which transition between the T-X regions occurs. The required linking expressions for the model phase diagram are provided in Table 2.4.

NUMERICAL SOLUTION

The governing equations (Equations 1-4) are in a form similar to the standard governing equations for single-phase systems and any established numerical procedure may be employed to solve them. The methodology used in this study is that of the control volume formulation (Patankar, 1980). The PHOENICS algorithm (Rosten and Spalding, 1987) was employed to carry out the solution of the governing equations and the mass fractions were updated iteratively following the procedures outlined in Prakash and Voller (1989). Details of the numerical procedures and aspects of the particular application of the PHOENICS algorithm have been provided elsewhere (Barboza, 1995; Prakash and Voller, 1989). The major differences between the previous studies and this one are that this study includes: (1) variable viscosity and the addition of the required terms in the governing equations; (2) the two invariant-point phase diagram has been developed and employed; (3) additional relations for enthalpy exchange at the invariant points have been included; (4) switching functions for the permeability and viscosity following Oldenburg & Spera (1992) have been

incorporated; (5) the geometry of the simulations reflects melting from below, rather than solidification from the side; and (6) a natural rock composition is considered.

EXAMPLE PROBLEM

We consider melting of a sequence of metapelitic rocks in a two dimensional, 200 m x 200 m computational domain heated from below (Figure 2.5). This configuration was chosen because it is thought to be important in the generation of some classes of igneous rocks (Bergantz and Dawes, 1994). The results are then compared to the melting of a hypothetical material that possesses identical thermo-physical properties, but whose melting relationships are best characterized by a binary eutectic. The equilibrium melt fraction vs. temperature curves for the pelite and the hypothetical binary material is shown in Figure 2.3. The heated strip was stipulated to be 100 m in width and long enough that the important features of the convection could be captured in two dimensions. The computational domain was oriented such that the right wall was normal to, and intersected the center of, the heated strip (Figure 2.5). A 60 x 60 variable spaced grid, slightly biased in both dimensions toward the heated strip, was employed. A grid refinement study was undertaken to ensure that the solutions were independent of spatial and temporal grid spacing.

The simulations were performed using a geometry and set of initial and boundary conditions characteristic of the melting of crustal rock in analogous geological systems. Justification for these conditions is provided in Barboza &

Bergantz (1996). At time $t=0$, the temperature along the heated strip was elevated to a value of T_{contact} . This contact temperature was maintained through the duration of the simulations. The remainder of the boundaries were thermally insulated. No-slip boundary conditions were employed on the left wall, roof, and floor and free-slip conditions were permitted on the right wall. A summary of the various model parameters used in the simulations is given in Table 2.5 and on Figure 2.5.

Bennon & Incropera (1987b) have argued that the irregular time-dependent geometry of the solid, liquid, and multiphase regions and the dependence of solidus and liquidus temperatures on the mixture composition precludes the establishment of meaningful universal length, temperature, and composition scales. Moreover, the additional dependence of the transport mechanism on the local melt fraction and the temperature, composition, and melt-fraction dependent viscosity considered in our model increases the scaling complexity. However, a scaling investigation is unneeded to demonstrate the influence of complex melting relationships on the dynamics of melt movement and the progress of melting. For our purposes, we consider the total duration of the simulations (approximately 160 years) to be equal to the period of the temperature perturbation. In other words, we assume that the duration reflects a reasonable characteristic time over which a constant temperature boundary condition may be maintained in analogous geological systems. The perturbation period and the associated conductive diffusion length over which the temperature fluctuations propagate, thus, provide a useful time and length scale with which to generalize the results.

We acknowledge that this approach to scaling the results is somewhat arbitrary. However, there is some geological justification for using the stated period as a basis for characteristic scales. A horizontal intrusion (sill) of mafic magma beneath a sequence of meta-sedimentary rocks is thought to have a role in the generation of some igneous rocks (Bergantz and Dawes, 1994). This configuration is also analogous to the system under consideration in this study. A simple calculation shows that the total enthalpy absorbed by the one invariant-point would require the heat released from the cooling and solidification of an underlying sill of mafic magma that was approximately 100 m thick. This sill thickness has been shown to be characteristic in several important geological systems, including those resembling that under consideration here (Oldenburg and Spera, 1991; Sinton and Detrick, 1992). Accordingly, we define the non-dimensional time to be:

$$t^* = \frac{t}{t_f} \quad (2.9)$$

where t_f is the total time duration of the simulations (5×10^9 s).

The thermal and dynamical state of the one and two invariant point systems are shown in Figures 2.6A and 2.6B, respectively. The figures illustrate the state of the two systems at $t^* = 0.2$ after the initiation of the simulations. The progression of the style of convection was similar in both cases. Convection was initially characterized by numerous small convection cells over the heated strip. The

wavelength of the initial instabilities as defined by the separation of the upwellings was approximately 20 - 25 m. As the cavity aspect ratio grew, certain cells grew at the expense of others until convection was dominated by a single, counter-clockwise rotating convection cell. However, the temporal evolution of convective style proceeded much more rapidly in the two invariant point case. As a result, higher convective velocities, a more rapidly propagating temperature perturbation, and more efficient melt generation was observed than in the one invariant point system. This is evident in Figure 2.6 where it can be seen that the height of the convecting cavity (defined by the CMF) in the two invariant point case (Figure 2.6B) has propagated nearly three times further than in the one invariant point case (Figure 2.6A). In addition, convection in the two invariant point case is fully developed (i.e. a single counter-clockwise rotating cell) at the selected time whereas five convection cells are still evident in the single invariant point case.

The enhanced convection in the two-invariant point system resulted from the fact that more melt was generated at lower temperatures. Due to the elevated low-temperature melt productivity, the two invariant-point system exceeded the CMF approximately 100 °C lower in temperature than the one invariant-point case (Figure 2.3). Bulk viscous flow of the mixture, consequently, occurred earlier in the course of the simulations and was more vigorous in the two invariant-point case. Since the buoyant porous flow of melt is an inefficient mechanism for transporting heat in this system (Barboza and Bergantz, 1996), any reduction in convective vigor of the mixture may have a substantial impact on heat transport and the progress melting.

The increase in convective vigor concomitant with the increase in melt productivity is further illustrated in Figures 2.7 and 2.8. Figure 2.7 depicts the evolution of the flux ratio (ϑ) as a function of time in the one and two invariant point systems. We define ϑ as the ratio of the transient instantaneous average heat flux across the heated strip measured in a convection simulation relative to that predicted by conduction alone. ϑ is thus analogous to the Nusselt number (Nu), which is often used to characterize the efficiency of convection for steady-state convective heat transport problems. The variability in the instantaneous heat flux in the convection simulations resulted in some scatter in ϑ . This observation is consistent with other experiments and simulations where such irregularities have been attributed to the unsystematic time-dependent nature of the solidus front growth rate (Bennon and Incropera, 1987b). Accordingly, the plots in Figures 2.7 and 2.8 are best fits to the measured data. Statistical data regarding the goodness of fit is given in the figure captions.

At $t^*=0.2$, coincident with the example simulation shown in Figure 2.6, $\vartheta=3.625$ in the two-invariant point case. At the same time, $\vartheta=1.603$ in the one-invariant point case. The efficiency of convective heat transport was, accordingly, increased by approximately 225% due to the enhanced low-temperature melt productivity in the two-invariant point case. The increased efficiency is also illustrated by the ratio of ϑ in the two-invariant point case to that of the one-invariant

point case $(\vartheta_2/\vartheta_1)$, also depicted in Figure 2.7. ϑ_2/ϑ_1 grows to a high of $\vartheta_2/\vartheta_1=4.962$ at $t^*=0.88$, then begins to decay. The decay in ϑ beginning at $t^*=0.9$ was due to thermal interaction of the temperature perturbation with the insulated walls. The simulations indicate that heat transport between the two systems will continuously diverge until the temperature gradient begins to decrease when the temperature perturbation preceding the convective upwelling reaches the roof of the computational domain.

Numerous experiments of natural convection in enclosures have been conducted which have resulted in empirical equations relating the steady-state thermal Rayleigh number (Ra_s) to an instantaneous average Nu. The experiments most relevant to the present study are those of Chu and Hickox (1990), who considered natural convection using a medium which possessed strongly variable viscosity and a geometry analogous to that used in this investigation. Chu and Hickox (1990) observe that

$$Nu_m = 0.54(Ra_m)^{0.25} \left(\frac{\mu_o}{\mu_h} \right)^{-0.035} \quad (2.10)$$

where the subscripts m , o , and h indicate that the properties are measured at the mean, upper surface, or heated strip temperatures respectively. It is a simple matter to ignore density change as a function of composition, assume that the convection is quasi-steady state, calculate Ra_s , and use the empirical relationship given in Equation 2.10 to

predict Nu. However, such calculations yield a Nu that is approximately an order of magnitude higher than the observed ϑ . We have determined that, for this case, the variation of density due to the composition gradient is significant and the compositional Ra (Ra_c) is typically the same order of magnitude as Ra_t . Additionally, the density variation resulting from the gradient in the melt composition is in the opposite sense of that resulting from the temperature gradient. As a result, convection is more sluggish than one would expect by applying relevant non-dimensional parameters based on thermal convection alone. To confirm this hypothesis, we have conducted steady-state simulations using the same algorithm, in which Ra_c was set to zero. In this analysis, ϑ was found to closely correspond with Nu obtained from Equation 2.10 despite the geometric differences between the studies due to curvature of the solidus front.

Figure 2.8 illustrates the relative difference in the increase in the global kinetic energy (KE) of the systems. The global KE was defined as

$$\sum KE_i = \frac{1}{2} \rho V_i (v_i^2 + u_i^2). \quad (2.11)$$

First, the KE was calculated for each control volume (i). The global KE was then calculated by summing the KE for the control volumes over the computational domain. The data in Figure 2.8 was obtained by taking the ratio of the global KE for the two-invariant point case to that of the one-invariant point case. The KE ratio

decayed from an initial high value of approximately 10^4 at $t^*=0.05$ exponentially, approaching a value of approximately 10^2 asymptotically. At $t^*=0.9$ the KE ratio began to decay again corresponding with the decay in ϑ previously discussed. The high initial values of the KE ratio at low t^* are attributed to the two-invariant point system exceeding the critical Ra and convection initiating earlier than the one-invariant point case. The asymptotic decay to a value exceeding one indicates that, all else being equal, convective vigor in the two-invariant point system will always exceed that of the one-invariant point case.

CONCLUSIONS

A new phase-change model for use with the continuum mixture formulation has been introduced and tested. The new model features two invariant points - a eutectic and a peritectic - and was used in a series of two-dimensional simulations of melting with variable viscosity. The results of these simulations were compared to those obtained from another series of numerical experiments which used a one invariant-point, phase-change model. The solidus front was observed to propagate away from the heated contact much more rapidly in the two invariant-point case. For example, at $t^*=0.2$, the solidus front had propagated over three times further. Additionally, the efficiency of convective heat transport and the global kinetic energy was found to be greater by over 200% and two orders of magnitude respectively. This comparison demonstrates that the complementary relationship

between melt productivity and the rheology of partially molten systems may have a large impact on the progress of melting and vigor of convection. The two invariant-point model permits the extension of the mixture formulation to systems with more complex melt productivity where such coupling may be significant.

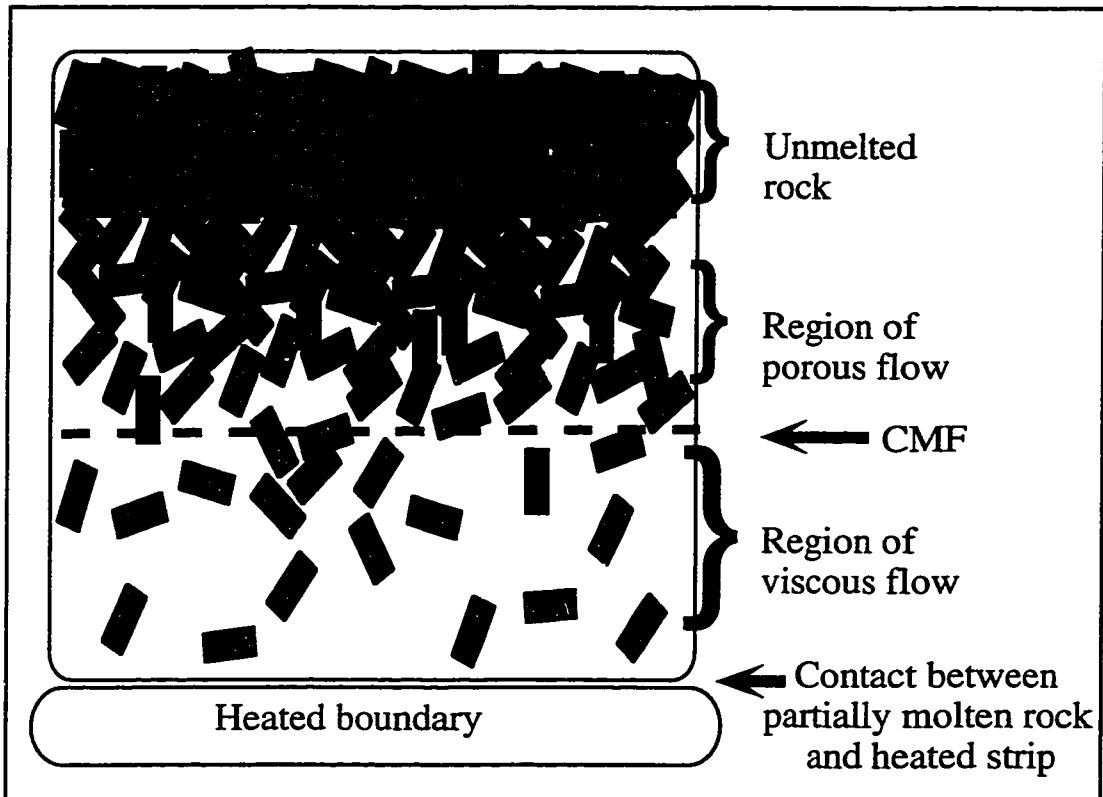


Figure 2.1. Schematic diagram of the rheological model. The base of a sequence of meta-sedimentary rocks is held at a constant temperature. Heat transfer to the sequence initiates partial melting and gives rise to double-diffusive convection of the mixture. Where the fraction of melt exceeds the critical melt fraction (CMF), bulk viscous flow of the partially molten mixture occurs. The suspended solids increase the bulk-mixture viscosity. Where the fraction of melt is less than the CMF, the solid is assumed to form a static-rigid matrix through which the melt flows.

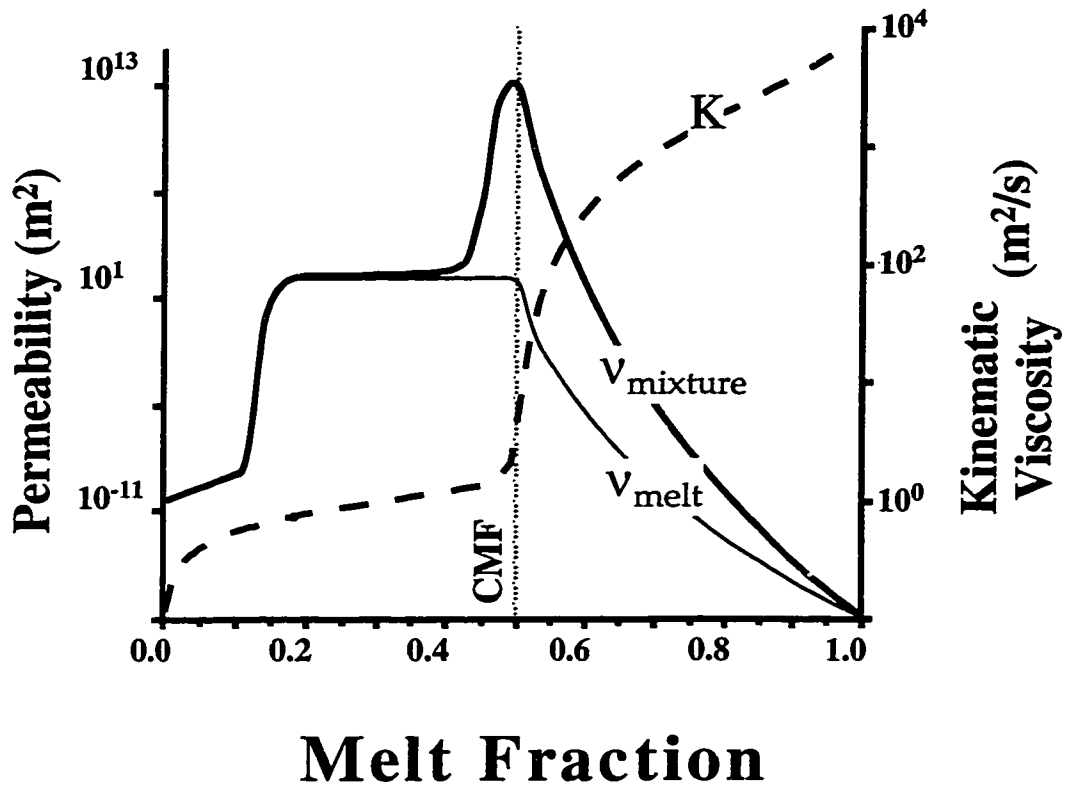


Figure 2.2. Plot of the kinematic viscosity of the mixture (heavy-solid line) and the melt (thin-solid line). The permeability (broken line) is also shown. For >0.5 , the switching function ensures that the Darcy drag source is negligible relative to the body-force source term. The influence of the presence of suspensions in the melt on the mixture viscosity modeled by the Krieger and Dougherty relation (Wildemuth and Williams, 1984). For <0.5 , the permeability is related to the porosity by the Blake-Kozeny-Carman equation (Beckermann and Viskanta, 1988a) and the mixture viscosity is that of the melt as calculated by the Shaw model (Shaw, 1972).

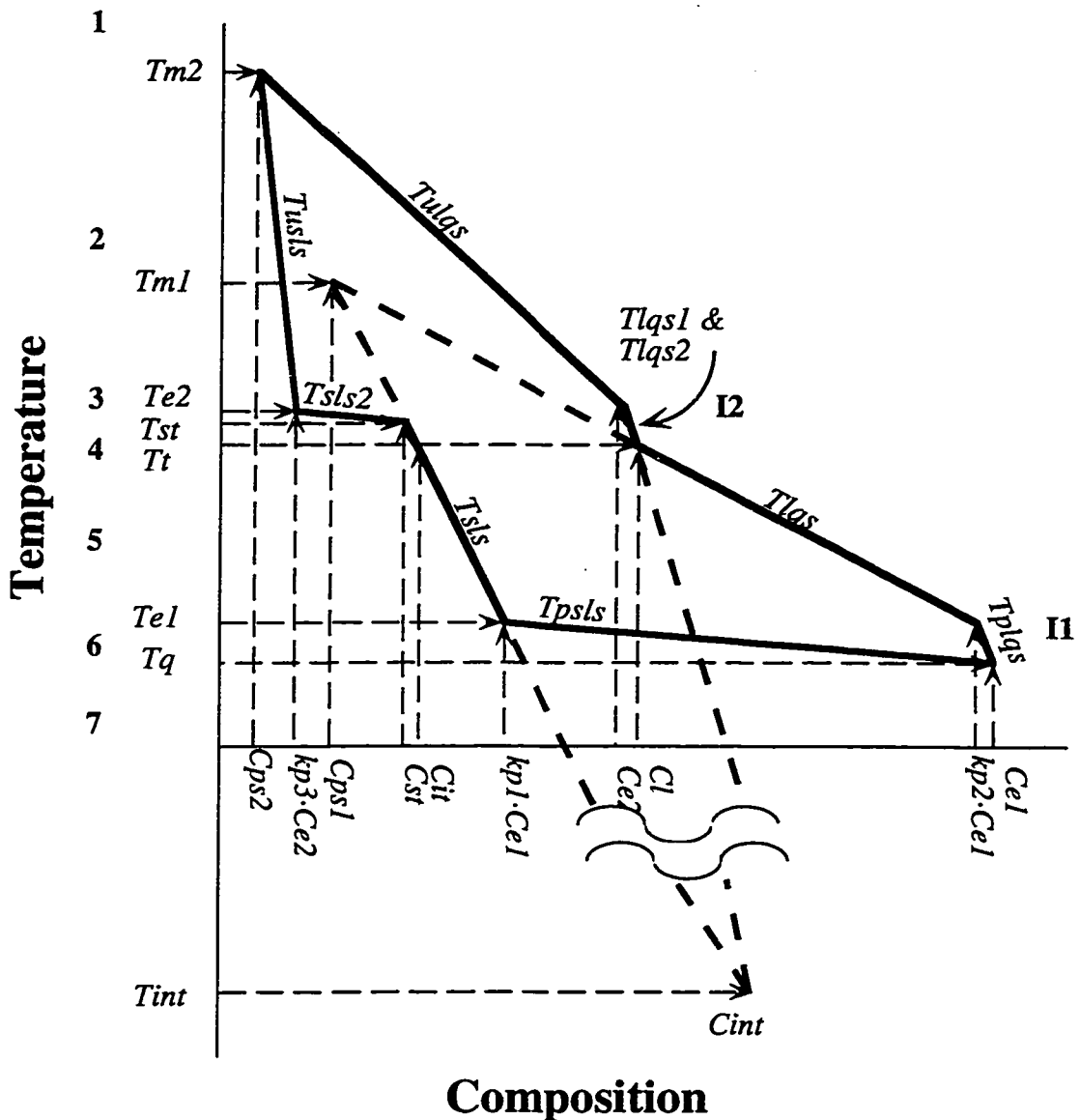


Figure 2.3. Schematic of the two invariant-point binary phase diagram. The parameters in italics listed along the temperature and composition axis fix the geometry of the univariant lines in temperature-composition (T-X) space. The values of these parameters are either constant (Table 2.5) or prescribed by linking functions (Table 2.4). The linking functions ensure that there is a smooth transition between univariant lines in each of the T-X regions. The T-X regions are defined by the intervals between the temperature parameters and are indicated by the numbers printed in bold along the temperature axis. These numbers correspond to the T-X regions listed in Tables 2.2, 2.3, and 2.4. I1 and I2 indicate the eutectic and peritectic respectively. The formulae specifying the slope of the univariant lines (T_{lqs} , T_{sls} , etc...) are given in Table 2.2.

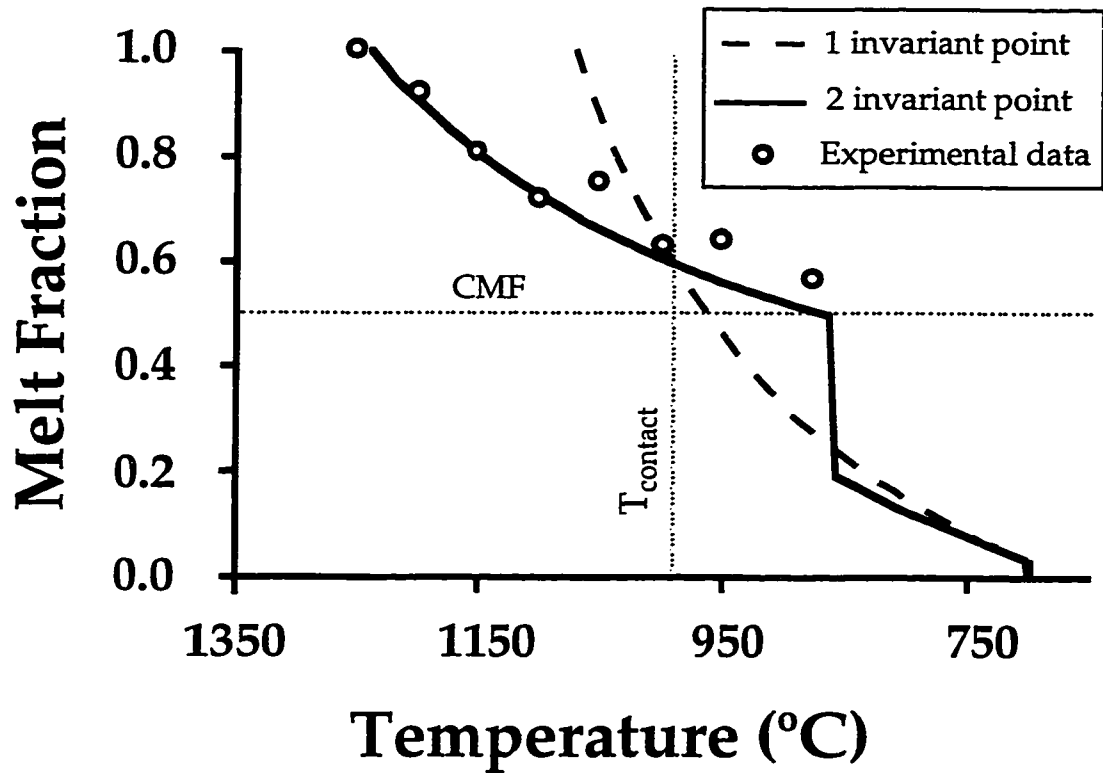


Figure 2.4. Plot of the melt productivity for the two cases. Solid line illustrates the variation of melt fraction with temperature of the two invariant-point system and the broken line is that of the one invariant-point system. The circles are the experimental data used to derive the geometry of the two invariant-point phase diagram. The melt productivity of the one invariant-point system was constructed so that both systems had the same melt fraction at the contact temperature (T_{contact}).

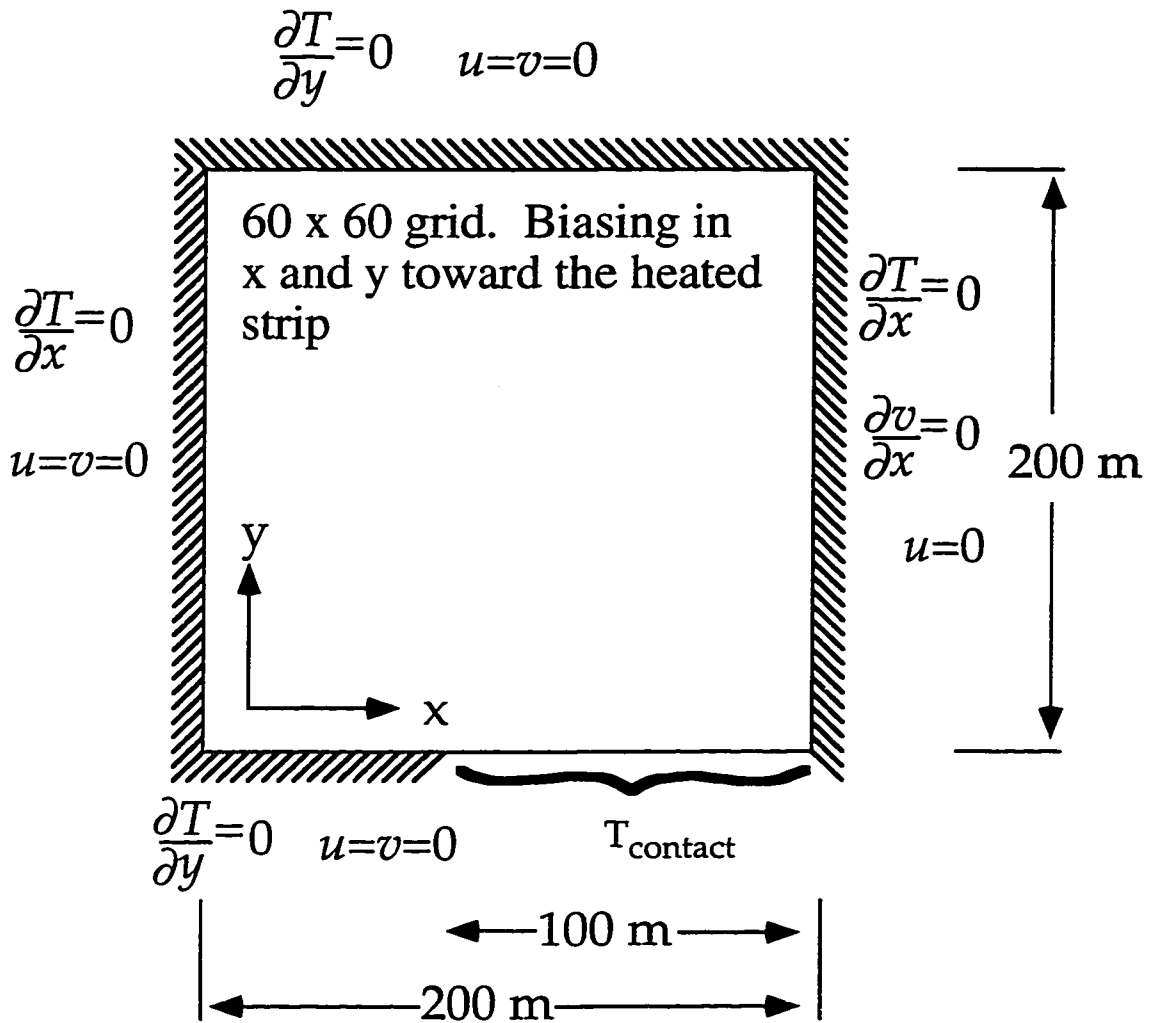


Figure 2.5. Schematic of computational domain.

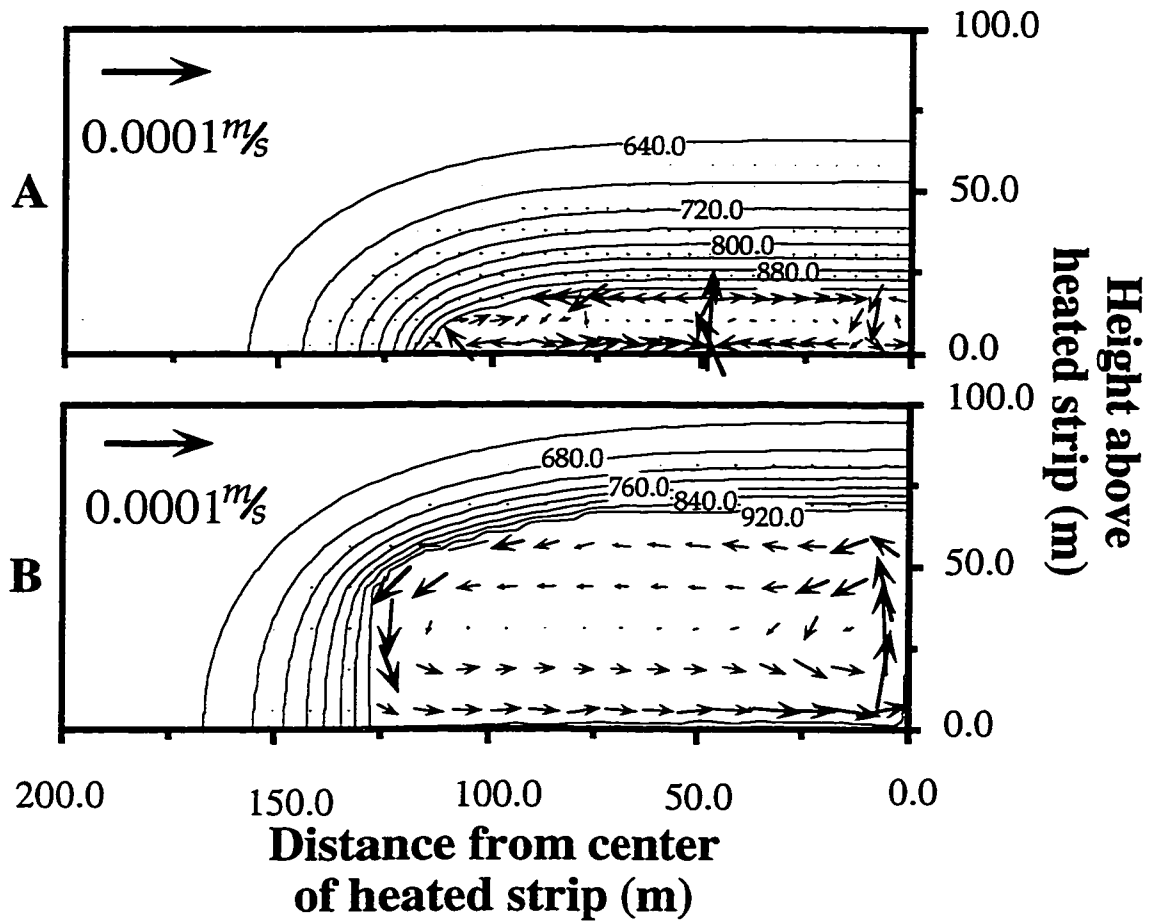


Figure 2.6. The mixture velocity (arrows) and temperature (contours in $^{\circ}\text{C}$) of the two models at $t^* = 0.2$. Plots A and B refer to the one and two invariant-point systems, respectively. The CMF (≈ 0.5) approximately bounds the limits of significant convection in both plots.

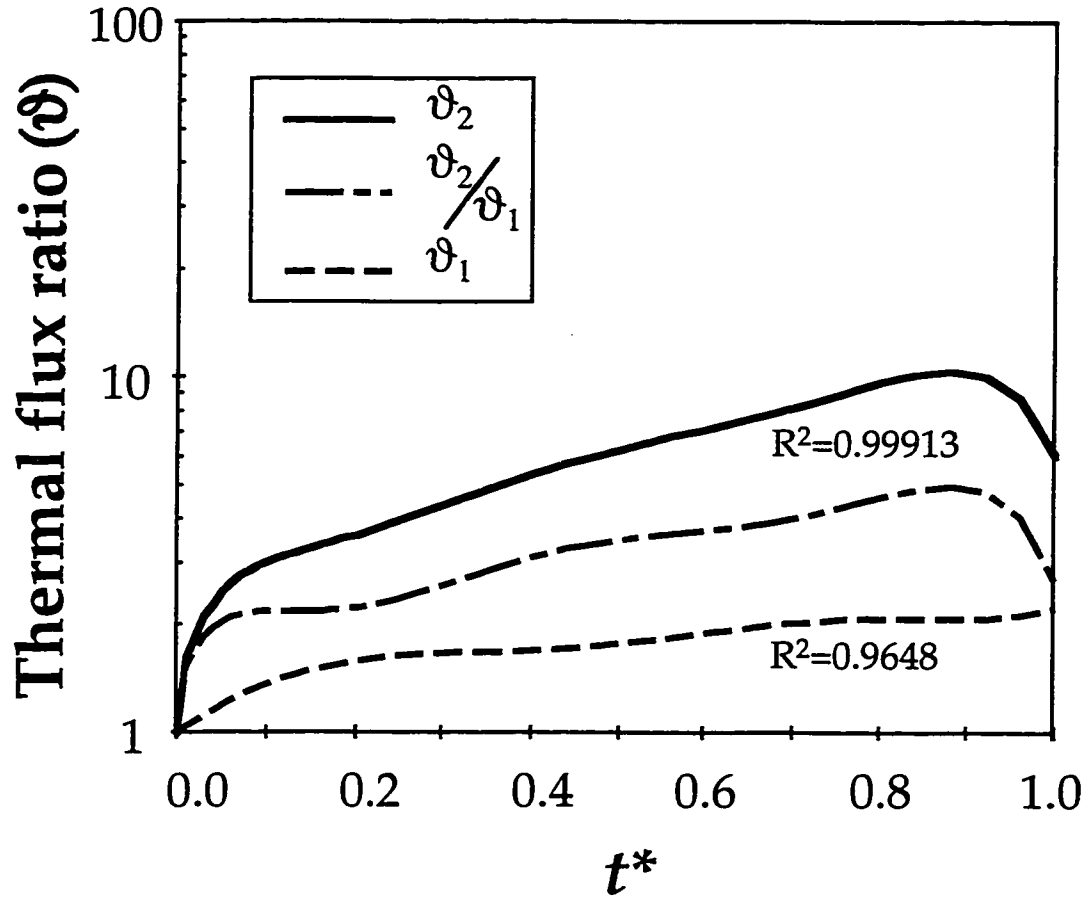


Figure 2.7. Plot of the flux ratio (ϑ). R^2 values on the chart indicate the statistical goodness-of-fit of the curves to the data. Variability in the data is attributed to time-dependent irregularities in the growth of the solidus front. The decay in ϑ at $t^* \approx 0.9$ results from the decrease in the temperature gradient due to sidewall heating in the two invariant-point case.

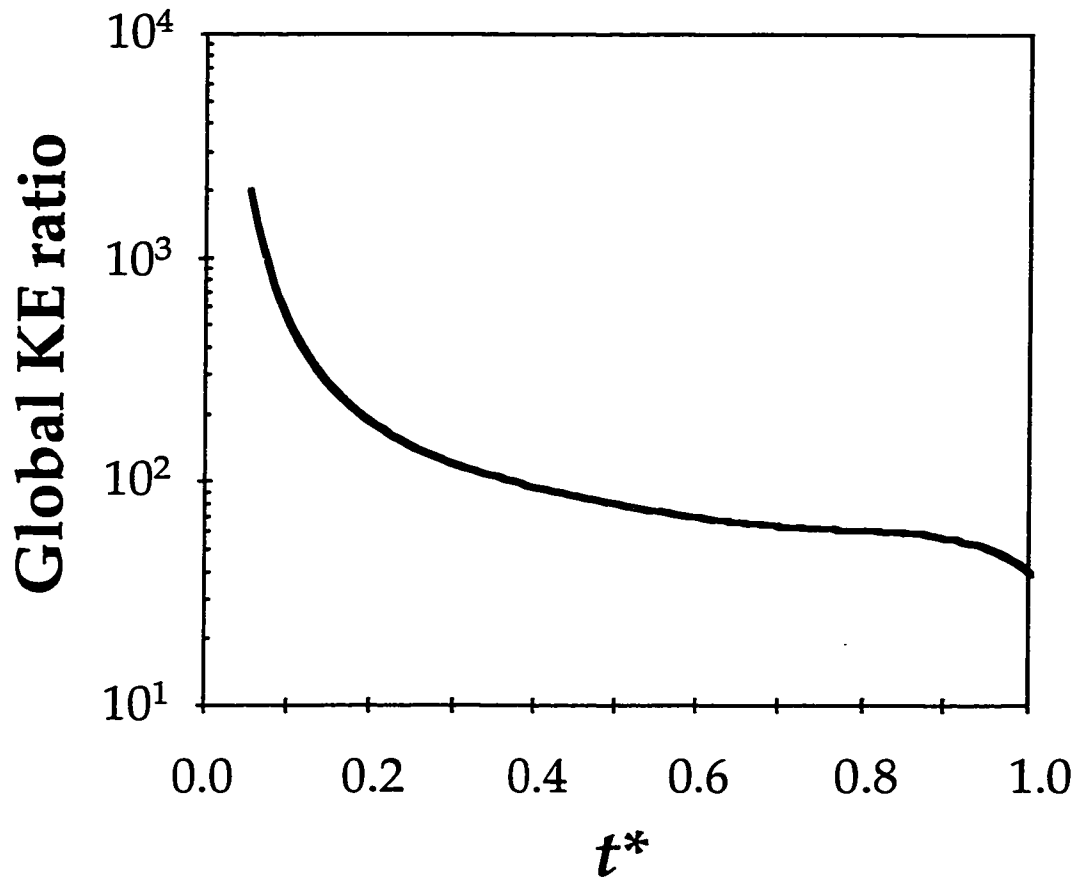


Figure 2.8. Plot of the ratio of the global kinetic energy (KE) of the two invariant-point system to that of the one-invariant point system. High values at low t^* indicate that convection in the two-invariant point case initiated earlier than in the one invariant-point case. Increasing decay at $t^* \approx 0.9$ is due to sidewall heating in the two-invariant point case.

Table 2.1: Nomenclature.

| | | | |
|-------------|---|--------------|--|
| c_p^a | heat capacity constituent a , J/kg·K | β_T^a | coefficient thermal expansion constituent a , 1/K |
| C, C^a | solute concentration in the mixture and constituent a , respectively, dimensionless | γ^a | mass constituent a per unit volume constituent a , kg/m ³ |
| D^a | diffusion coefficient constituent a , m ² /s | Γ | permeability switching function, dimensionless |
| f^a | mass fraction constituent a , dimensionless | ϑ | flux ratio, dimensionless |
| g^a | volume fraction constituent a , dimensionless | μ, μ^a | mixture viscosity and viscosity constituent a respectively, Pa·s |
| g_i | i th component gravitational acceleration, m/s ² | ρ | mass mixture per unit volume of mixture, kg/m ³ |
| k | thermal conductivity, J/(s·m·K) | ρ^a | mass constituent a per unit volume mixture, kg/m ³ |
| K_i | i th component anisotropic permeability, m ² | Φ | viscosity switching function, dimensionless |
| L | specific latent heat, J/K | | |
| p | static pressure or isotropic stress mixture, Pa | | |
| t | time, s | | |
| T | temperature, °C | | |
| v_i^a | i th component mixture velocity constituent a , m/s | o | Subscripts reference value |
| V_i | i th partial volume of computational domain, m ³ | ℓ | Superscripts liquid phase |
| β_C^a | coefficient of solutal expansion constituent a , 1/K | s | solid phase |

Table 2.2. Geometry of phase diagram

| Region | Slope of liquidus | Slope of solidus | Temperature Range | Notes |
|--------|--|---|--------------------------|----------------------------------|
| 1 | na | na | $T > T_{m2}$ | above liquidus for all C_{mix} |
| 2 | $T_{lqs} = T_{m2} + (T_{e2} - T_{m2}) \left(\frac{C_{mix} - C_{ps2}}{C_{e2} - C_{ps2}} \right)$ | $T_{s1s} = T_{m2} + (T_{e2} - T_{m2}) \left(\frac{C_{mix} - C_{ps2}}{k_{p3} \cdot C_{e2} - C_{ps2}} \right)$ | $T_{m2} \geq T > T_{e2}$ | |
| 3 | $T_{lqs2} = T_{e2} + (T_t - T_{e2}) \left(\frac{C_{mix} - C_{e2}}{C_{lt1} - C_{e2}} \right)$ | $T_{s1s2} = T_{e2} + (T_t - T_{e2}) \left(\frac{C_{mix} - k_{p3} \cdot C_{e2}}{C_{lt1} - k_{p3} \cdot C_{e2}} \right)$ | $T_{e2} \geq T > T_{st}$ | peritectic region |
| 4 | $T_{lqs1} = T_{e2} + (T_t - T_{e2}) \left(\frac{C_{mix} - C_{e2}}{C_{lt1} - C_{e2}} \right)$ | $T_{s1s1} = T_{m1} + (T_{e1} - T_{m1}) \left(\frac{C_{mix} - C_{ps1}}{k_{p1} \cdot C_{e1} - C_{ps1}} \right)$ | $T_{st} \geq T > T_t$ | peritectic region |
| 5 | $T_{lqs} = T_{m1} + (T_{e1} - T_{m1}) \left(\frac{C_{mix} - C_{ps1}}{k_{p2} \cdot C_{e1} - C_{ps1}} \right)$ | $T_{s1s} = T_{m1} + (T_{e1} - T_{m1}) \left(\frac{C_{mix} - C_{ps1}}{k_{p1} \cdot C_{e1} - C_{ps1}} \right)$ | $T_t \geq T > T_{e1}$ | |
| 6 | $T_{plqs} = T_{e1} + (T_q - T_{e1}) \left(\frac{C_{mix} - k_{p2} \cdot C_{e1}}{C_{e1} - k_{p2} \cdot C_{e1}} \right)$ | $T_{ps1s} = T_q + (T_{e1} - T_q) \left(\frac{C_{mix} - C_{e1}}{k_{p1} \cdot C_{e1} - C_{e1}} \right)$ | $T_{e1} \geq T \geq T_q$ | eutectic region |
| 7 | na | na | $T > T_q$ | below solidus for all C_{mix} |

Table 2.3. Melt fractions and phase compositions

| Region | Melt fraction | Liquid composition | Solid composition |
|--------|--|---|--|
| 1 | $f' = 1$ | $C_{liq} = C_{mix}$ | $n a$ |
| 2 | $f' = \left[\frac{1}{1 - \left(\frac{kp3 \cdot Ce2 - Cps2}{Ce2 - Cps2} \right)} \right] \left[\frac{T - T_{ulqs}}{T - T_{m2}} \right]$ | $C_{liq} = \left(\frac{f' - 1}{f'_{max4} - 1} \right) (Ce2 - C_{mix}) + C_{mix}$ | $C_{sol} = \left(\frac{f' - 1}{f'_{max4} - 1} \right) (kp3 \cdot Ce2 - C_{mins}) + C_{mix}$ |
| 3 | $f' = \left[\frac{1}{1 - \left(\frac{kp4 - 1}{kp3 - 1} \right)} \right] \left[\frac{T - T_{sls2}}{T - T_t} \right]$ | $C_{liq} = \left(\frac{f' - f'_{max4}}{f'_{max3} - f'_{max4}} \right) (C_{lt2} - Ce2) + Ce2$ | $C_{sol} = \left(\frac{f' - f'_{max4}}{f'_{max3} - f'_{max4}} \right) (C_{st} - kp3 \cdot Ce2) + kp3 \cdot Ce2$ |
| 4 | $f' = \left[\frac{1}{1 - \left(\frac{kin2 - 1}{kin1 - 1} \right)} \right] \left[\frac{T - T_{sls1}}{T - T_{int}} \right]$ | $C_{liq} = \left(\frac{f' - f'_{max3}}{f'_{max2} - f'_{max3}} \right) (C_{lt1} - C_{lt2}) + C_{lt2}$ | $C_{sol} = \left(\frac{f' - f'_{max3}}{f'_{max2} - f'_{max3}} \right) (C_{it} - C_{st}) + C_{st}$ |
| 5 | $f' = 1 - \left[\frac{1}{1 - \left(\frac{kp1 \cdot Ce1 - Cps1}{kp2 \cdot Ce1 - Cps1} \right)} \right] \left[\frac{T - T_{lqs}}{T - T_{m1}} \right]$ | $C_{liq} = \left(\frac{f' - f'_{max2}}{f'_{max1} - f'_{max2}} \right) (kp2 \cdot Ce1 - C_{lt1}) + C_{lt1}$ | $C_{sol} = \left(\frac{f' - f'_{max2}}{f'_{max1} - f'_{max2}} \right) (kp1 \cdot Ce1 - C_{it}) + C_{it}$ |
| 6 | $f' = \left[\frac{1}{1 - \left(\frac{kp2 - 1}{kp1 - 1} \right)} \right] \left[\frac{T - T_{psls}}{T - T_q} \right]$ | $C_{liq} = \left(1 - \frac{f'}{f'_{max1}} \right) (Ce1 - kp2 \cdot Ce1) + kp2 \cdot Ce1$ | $C_{sol} = \left(1 - \frac{f'}{f'_{max1}} \right) (C_{mix} - kp1 \cdot Ce4) + kp1 \cdot Ce1$ |
| 7 | $f' = 0$ | $n a$ | $C_{sol} = C_{mix}$ |

Table 2.4. Auxilliary realltions and linking functions

| | | |
|---|---|---|
| $f'_{max1} = \frac{C_{mix} - kp1 \cdot Ce1}{kp2 \cdot Ce1 - kp1 \cdot Ce1}$ | $C_{mix} = Cps2 + (kp3 \cdot Ce2 - Cps2) \left(\frac{T_{ulqs} - T_{m2}}{Te2 - T_{m2}} \right)$ | $C_{st} = kp3 \cdot Ce2 + (Clf1 - kp3 \cdot Ce2) \left(\frac{T_{st} - Te2}{Tt - Te2} \right)$ |
| $f'_{max2} = \frac{C_{mix} - Cit}{Clf1 - Cit}$ | $T_{int} = \frac{Cps1 - Ce2 + Te2 \left(\frac{Clf1 - Ce2}{Tt - Te2} \right) - T_{m1} \left(\frac{kp1 \cdot Ce1 - Cps1}{Te1 - T_{m1}} \right)}{\left(\frac{Clf1 - Ce2}{Tt - Te2} \right) - \left(\frac{kp1 \cdot Ce1 - Cps1}{Te1 - T_{m1}} \right)}$ | $T_{st} = \left(\frac{B}{Tt - Te2} \right) - A$ |
| $f'_{max3} = \frac{C_{mix} - C_{st}}{Clf2 - C_{st}}$ | $C_{int} = Ce2 + (Clf1 - Ce2) \left(\frac{T_{int} - Te2}{Tt - Te2} \right)$ | $A = (Te1 - T_{m1}) \left[\frac{Te2(Cl f1 - kp3 \cdot Ce2)}{+(Tt - Te2)} \right] (Cps1 - kp3 \cdot Ce2)$ |
| $f'_{max4} = \frac{C_{mix} - kp3 \cdot Ce2}{Ce2 - kp3 \cdot Ce2}$ | $K_{int1} = \frac{C_{st}}{C_{int}}$ | $B = T_{m1}(Tt - Te2)kp1 \cdot Ce1 - A$ |
| | $K_{int2} = \frac{Clf2}{C_{int}}$ | $Clf1 = Cps1 + (kp2 \cdot Ce1 - Cps1) \left(\frac{Tt - T_{m1}}{Te1 - T_{m1}} \right)$ |
| | $Cit = Cps1 + (kp1 \cdot Ce1 - Cps1) \left(\frac{Tt - Te2}{Cps1 - kp3 \cdot Ce2} \right)$ | $Clf2 = Ce2 + (Clf1 - Ce2) \left(\frac{T_{st} - Te2}{Tt - Te1} \right)$ |

Table 2.5: Values of constants.

| Parameter | Value |
|--|------------------------|
| <i>Thermophysical and rheological properties</i> | |
| Specific heat (J/kg·K) | 1.04×10^3 |
| Thermal conductivity (W/m·K) | 1.9 |
| Density (kg/m ³) | 2.507×10^3 |
| Kinematic viscosity (m ² /s) | see text |
| Schmidt number (μ'/D) | 1.0×10^6 |
| Latent heat (J/kg) | 1.0×10^5 |
| Permeability coefficient (m ²) | 5.56×10^{-10} |
| Thermal expansion coefficient (K ⁻¹) | 1.05×10^{-4} |
| Solutal expansion coefficient | 1.55×10^{-1} |
| Critical melt fraction | 0.5 |
| <i>Initial and boundary conditions</i> | |
| Pelite starting composition | 0.325 |
| Initial temperature (°C) | 600.0 |
| Contact temperature (°C) | 1000.0 |
| Total time duration of simulations (s) | 5×10^9 |
| <i>Phase diagram parameters</i> | |
| $Tm1$ (°C) | 1250 |
| $Tm2$ (°C) | 1600 |
| Tq (°C) | $Te1 - \epsilon$ |
| $Te1$ (°C) | 700 |
| $Te2$ (°C) | 860 |
| $Ce1$ | 0.873 |
| $Ce2$ | $kp4 \cdot Clt1$ |
| $Cps1$ | 0.1 |
| $Cps2$ | 0.0 |
| $kp1$ | 0.35 |
| $kp2$ | 0.999 |
| $kp3$ | 0.0001 |
| $kp4$ | 0.999 |
| ϵ (°C) | 10.0 |
| Tt (°C) | 860 |

CHAPTER 3: RHEOLOGICAL TRANSITIONS AND THE PROGRESS OF MELTING OF CRUSTAL ROCKS

INTRODUCTION

The rheological transition between solid and melt may strongly influence the thermal evolution of high-temperature igneous and metamorphic systems. Changes in the viscosity and density, as a function of the local melt fraction, contribute to the efficiency of convective heat transfer. Quantitative thermo-physical models for such systems require constitutive equations that include the variability in rheological properties over the full range of melt fraction. Two end-member rheological states can be recognized in natural systems: 1) fully fluid behavior and 2) a nearly rigid solid with a crystal-supported pore structure. The transition between these end-members need not be abrupt, but will vary as a function of the system properties and the strain rate. In this study, we demonstrate that the choice of the melt fraction interval for the rheological transition can significantly influence the predicted thermal evolution of crystal-melt mixtures during melting or solidification.

One model for the rheological transition from crystal-supported to fully fluid behavior is an abrupt transition over a small melt-fraction interval. The melt fraction at which this transition takes place has been termed the rheological critical melt percentage (Arzi, 1978), or critical melt fraction (CMF) (van der Molen and

Paterson, 1979). The CMF model assumes that a large change in rock strength occurs over a small melt-fraction interval that falls between 28% and 50% melt. This model was inferred from the results of low-melt-fraction deformation studies in which this transition may have been observed (Arzi, 1978; van der Molen and Paterson, 1979). The CMF model is also in agreement with theoretical calculations and the results of experiments with dilute suspensions (Jeffrey and Acrivos, 1976; Roscoe, 1952; Wildemuth and Williams, 1984). Figure 3.1 schematically depicts the CMF model for the transition from a crystal-supported system to a suspension with the concomitant increase in the viscosity of the mixture. Empirical relationships for the viscosity of suspensions and data from relevant deformation experiments are illustrated in Figure 3.2.

However, the results of several low-melt-fraction deformation experiments (Figure 3.2) are not in accord with those of the earlier studies (Rushmer, 1995; Rutter and Neumann, 1995). These experimental results indicate that there may be a melt-fraction interval over which local variations in melt fraction, composition, microscopic pore geometry, and strain rate dictate local variations in the rheological response of the mixture. In addition, Vigneresse et al. (1996) and Wildemuth and Williams (1984), based on experimental results and field observations, suggested that the rheological transition may proceed through two or more stages rather than occur at a single melt fraction. Sawyer (personal communication) observed that the experimental work supporting the CMF model was conducted in the brittle deformation regime. The majority of crustal melts are generated in the plastic

deformation regime, which may obscure an abrupt rheological transition. These experiments and observations document the uncertainty in the applicability of the CMF model for a wide range of geological conditions.

This uncertainty may be significant, because the general validity of the CMF model is often assumed when inferring crustal magmatic processes from geological data. For instance, the periodic loss of grain-grain contiguity during heating has been used to explain the episodicity of deformation, metamorphism, and granitoid magmatism in low-pressure, high-temperature metamorphic terranes (Stüwe et al., 1993). Tectonic surges, or the rapid displacement of high-grade crustal blocks, have been ascribed to weakening of the crust where the regional melt fraction exceeds the CMF (Hollister and Crawford, 1986). The CMF model has been used to explain why basaltic magmas preferentially enter fissures as dikes and why rhyolites are most often represented by ash flows rather than lavas (Pitcher, 1993). The agmatic and schlieric structures in migmatites, localized magmatic shear zones, the contact relationships between granitoid intrusive suites, and the phenocryst content in lava flows and dikes have all been attributed to the loss of solid contiguity at the CMF (Marsh, 1981; van der Molen and Paterson, 1979; Wickham, 1987).

A rheological model consistent with the experimental work of Rushmer (1995) and Rutter and Neumann (1995) would include a wider melt-fraction interval than assumed in the CMF model. However, the degree to which a more gradual rheological transition may influence interpretations of crustal magmatic processes is unknown. Crustal melting is one process in which the progress of melting and rate of

heat transfer has been ascribed to the rheological transition between a partially molten solid and a viscous suspension (Bittner and Schmeling, 1995; Cruden et al., 1995). We have conducted a series of transient numerical simulations of crustal melting in which we quantify the impact of the alternative rheological model on convective heat transfer and melting progress. Our results indicate that the form of the rheological transition may be one of the dominant controls on the dynamics of heat and mass transport during crustal anatexis.

CONTINUUM MODEL

We have adopted a two-phase continuum-mixture formulation to model crustal melting. This approach permits constitutive equations to be included in the governing equations which model the mechanical behavior of the mixture with increasing melt fraction. A comprehensive discussion of the continuum equations for double-diffusive heat and mass transfer in phase-change systems is available (Barboza and Bergantz, 1997; Beckermann and Viskanta, 1988b; Bennon and Incropera, 1987a; Ni and Beckermann, 1991; Oldenburg and Spera, 1991). The variable viscosity form of the mixture continuum-conservation equations for phase change and convection in two dimensions are:

$$\frac{\partial v_j}{\partial x_j} = 0 \quad (3.1)$$

$$\frac{\partial}{\partial t}(\rho v_i) + \frac{\partial}{\partial x_j}(\rho v_j v_i) = -\frac{\partial p}{\partial x_i} + \frac{\partial}{\partial x_j} \left(\mu \frac{\partial v_i}{\partial x_j} \right) + \frac{\rho}{\rho'} \frac{\partial v_i}{\partial x_j} \frac{\partial \mu}{\partial x_j} + \quad (3.2)$$

$$g' \gamma'_o g_i \left[\beta'_T (T - T_o) + \beta'_C (C' - C'_o) \right] + \frac{\mu'}{K_i} (f' v'_i)$$

$$\frac{\partial}{\partial t}(\rho T) + \frac{\partial}{\partial x_i}(\rho v_i T) = \frac{\partial}{\partial x_i} \left(\frac{k}{c'_p} \frac{\partial T}{\partial x_i} \right) - \rho \frac{L}{c'_p} \frac{\partial f'}{\partial t} + \rho \frac{(c'_p - c_p^s)}{c'_p} \frac{\partial}{\partial t} (f^s T) \quad (3.3)$$

$$\frac{\partial}{\partial t}(\rho C) + \frac{\partial}{\partial x_i}(\rho v_i C) = \frac{\partial}{\partial x_i} \left(\rho f' D' \frac{\partial C}{\partial x_i} \right) \quad (3.4)$$

$$+ \frac{\partial}{\partial x_i} \left[\rho f' D' \frac{\partial}{\partial x_i} (C' - C) \right] - \frac{\partial}{\partial x_i} [\rho v_i (C' - C)]$$

The nomenclature for the formulae is presented in Table 3.1.

The continuum-mixture governing equations (Equations 3.1-3.4) require thermodynamic functions that link the enthalpy and composition to the local melt fraction. A pseudo-binary was projected from the 10 kbar NKM ($\text{Na}_2\text{O}\cdot\text{Al}_2\text{O}_3$ - $\text{K}_2\text{O}\cdot\text{Al}_2\text{O}_3$ - MgO + FeO) silica-, alumina-, and titania-saturated pseudo-ternary to generate this data. A discussion of the theory, limitations, and assumptions of this projection is presented elsewhere (Barboza and Bergantz, 1996; Barboza and Bergantz, 1997).

The rheology of the mixture is implemented by source terms that account for the different flow regimes as a function of the local melt fraction. For example, the last term on the right-hand side of the momentum conservation expression (Equation 3.2) is the Darcy drag source term (Bennon and Incropera, 1987a). This relationship accounts for viscous drag between the solid and the

interstitial melt as a function of the permeability, and provides the dominant balance between buoyancy and pressure when the melt fraction is low. According to the CMF model, with increasing melt fraction the solid grains lose contiguity over a small melt-fraction interval and form a viscous suspension with the melt. In our new physical model the Darcy source imparts a drag on the mixture over a wider melt-fraction interval. In this way we account for the additional drag resulting from the local variability in flow regimes within the melt-fraction interval over which the mechanical transition for the mixture occurs.

The dynamic viscosity of the suspension must include the contribution of the crystals, as well as the variable temperature and composition of the melt. Following Oldenburg and Spera (1992), the permeability and dynamic viscosity relationships are:

$$K = \Gamma K_o \left[\frac{(f')^3}{(1-f')^2} \right] \quad (3.5)$$

$$\Gamma = \left\{ 0.5 + \frac{1}{\pi} \arctan[100(f'_{crit} - f')] \right\}^{-5} \quad (3.6)$$

$$\mu(T, C, f') = \left[1 - \Phi \left(\frac{1-f'}{f'_{crit}} \right) \right]^{-2} \mu'(T, C) \quad (3.7)$$

$$\Phi = 0.5 - \frac{1}{\pi} \arctan[100(f'_{crit} - f')] \quad (3.8)$$

We assume that, at low melt fraction, the permeability is related to the local melt fraction by the Blake-Kozeny-Carman equation (Equation 3.5) (Voller and Prakash, 1987). K_o is a constant dependent on the multiphase region morphology (Asai and Muchi, 1978). This relationship is considered generally valid in the laminar flow regime and for melt-volume fractions less than 0.5 (Bird et al., 1960). At high melt fraction, the dynamic viscosity of the melt is calculated using the Shaw model (Shaw, 1972) and the drag from suspended crystals is modeled by the Krieger-Dougherty relation (Krieger and Dougherty, 1959) (Equation 3.7) as presented in Wildemuth and Williams (1984).

Following Oldenburg and Spera (1992), mechanical differences between the solid and melt are implemented by arctangent switching functions (Equations 3.6 and 3.8) multiplied to the relevant terms in the governing equations (Oldenburg and Spera, 1992). Both the permeability and the dynamic viscosity are switched in this manner. These switching functions ensure that the Darcy drag source is included when the local melt fraction (f') is low and the viscosity contribution of suspensions is included for $f' \geq 0.5$. We initiate the transition between crystal-supported and fully fluid behavior at $f' = 0.5$ in all simulations as this value may be important in magmatic systems (Marsh, 1981; Miller et al., 1988). The permeability switching-function power law (ζ in Equation 3.6) determines melt-fraction interval over which the rheological transition takes place. We do not smooth the viscosity switching function, as a more gradual transition to a viscous suspension would

increase the local mixture viscosity at a given melt fraction. Therefore, our results are an upper end-member for convective heat transfer with respect to the mixture viscosity. The remaining source terms accounting for the energy of phase change are discussed elsewhere (Barboza and Bergantz, 1997; Bennon and Incropera, 1987a; Prakash and Voller, 1989).

We consider six values of ζ which span a range of possible gradations of the rheological transition. At one limit is the traditional CMF model that requires the Darcy drag source vanishes over a small increase in melt fraction between 28% and 50% melt. The CMF model is implemented in the $\zeta = 10$ simulations where the Darcy drag source approaches zero between $0.5 < f' < 0.57$. More abrupt rheological transitions ($\zeta > 10$) were tested, but did not produce appreciably different results than the $\zeta = 10$ simulations. The rheological transition occurs over a wider melt fraction interval for smaller values of ζ . The permeability and kinematic viscosity ($=\mu/\rho$), modified by the switching functions with the various power laws, are illustrated in Figure 3.3. The shapes of the viscosity profiles in Figure 3.3 are discussed in detail elsewhere (Barboza and Bergantz, 1996).

MODEL ASSUMPTIONS

We assume that the source region remains undrained through the duration of the simulations (160 yrs). Also, our implementation of the mixture model does not allow us to consider diapiric instabilities of the growing melt layer into the unmelted roof. Newhouse and Pozrikidis (Newhouse and Pozrikidis, 1990) have carried out a linear stability analysis of the growth rate of diapiric instabilities. The amount of time before the amplitude of the diapiric instabilities double is approximately an order of magnitude longer than the duration of the simulations. Therefore, diapiric instabilities are unlikely to be significant on the time scales considered in the simulations.

The mixture model does not allow for relative motion between phases in the viscous flow regime, so processes such as crystal settling are not considered. This assumption does not limit the utility of the mixture model if the flow field of the carrier fluid dominates the particle motion. This is likely to be the case as long as typical velocities of the crystal-melt mixture exceed the predicted Stokes settling velocities of the dispersed crystals. Assuming the particle Reynolds number is less than one, the settling velocity of crystals can be obtained by equating the Stokes drag formula to the gravitational buoyancy force (Turcotte and Schubert, 1982). Stokes settling velocities calculated for 1-10 cm crystals are less than typical average velocities of the crystal-melt mixture in the viscous flow regime. Therefore, differential motion between the crystals and melt is unlikely to significantly influence the flow of the mixture.

In the development of the governing equations (Equations 3.1-3.4) we assume: (i) the velocity of the solid phase is zero ($v_s = 0$); (ii) the mixture is fully saturated ($g' + g^s = 1$); (iii) the flow of the melt is laminar and Newtonian; (iv) the Boussinesq approximation is valid; (v) local thermodynamic equilibrium ($T' = T^s = T$) is maintained; (vi) the phase specific heats are constant, though not necessarily equal; (vii) the diffusion of species in the solid phase is negligible; (viii) the solid phase is rigid and free of internal stresses; and (ix) the permeability of the partially molten solid is isotropic (Bennon and Incropera, 1987b). The assumption of mixture saturation and a stress-free solid also implies that the phase densities and thus the phase volume and mass fractions are equal ($\rho^s = \rho'$, $f^i = g^i$).

MODEL DESCRIPTION AND GEOLOGICAL MOTIVATION

We defined a model protolith with a nonlinear relationship between temperature and melt fraction (melt productivity) based on the metapelite used in the experiments of Vielzeuf and Holloway (1988). Dehydration melting of biotite in this rock composition may produce up to ~55% melt over a small temperature interval near 850 °C, thereby exceeding the CMF. This lithology thus provides a useful mechanical end-member for our calculations, as the CMF is exceeded at lower temperatures than for many crustal rocks (Bergantz and Dawes, 1994). The phase relations were experimentally derived by Patiño Douce and Johnston (1991) using their own data

along with those of Vielzeuf and Holloway (1988) and Le Breton and Thompson (1988). The model equilibrium melt productivity curve is compared to the experimental data in Figure 3.4.

The model dimensions and boundary conditions are based on conditions expected in the vicinity of a 200 m wide basaltic sill in the mid-to-lower continental crust (underplating) (Barboza and Bergantz, 1996). The 200 m x 200 m computational domain was represented by a 70 x 70 node, variable-spaced grid, refined in both dimensions toward the heated boundary (Figure 3.5). The solutions are assumed to be symmetric around the right margin of the computational domain. A grid refinement study was undertaken to ensure that the simulations were independent of the spatial and temporal grid discretization. Particular attention was paid to the grid dependence at the initiation of convection. Heat flux over the first two years of the CMF model simulations ($\zeta = 10$) varied less than 1% after increasing the density of the vertical distribution of grid points by a factor of four.

At the start of the simulations, the temperature of the country rock was uniform with a value of 600 °C. The roof and walls were thermally insulated. We implemented basaltic underplating by fixing the temperature along a 100 m strip from the center of the lower boundary to the right wall to 1000 °C. Free-slip conditions were assigned to the right wall and no-slip conditions on the remaining boundaries. A summary of the various model parameters and boundary conditions used in the simulations is given in Table 3.2 and Figure 3.5.

We based the numerical algorithm on the control-volume formulation (Patankar, 1980) and used the PHOENICS algorithm (Rosten and Spalding, 1987) to solve Equations 3.1-3.4. The mass fractions were updated iteratively following the procedures outlined in Prakash and Voller (1989). Details of the numerical procedures and other aspects of this application of the PHOENICS algorithm are provided elsewhere (Barboza and Bergantz, 1996; Barboza and Bergantz, 1997; Prakash and Voller, 1989).

RESULTS AND DISCUSSION

In previous studies we demonstrated the sensitivity of convective heat transport on the melt productivity (increase in melt fraction with temperature) of the protolith, viscosity of the melt, and the melt fraction at which the rheological transition takes place (CMF) (Barboza and Bergantz, 1996; Barboza and Bergantz, 1997). In the ensuing sections, we demonstrate the influence on convective heat transfer of the rheological transition between a partially molten solid and a viscous suspension. Five sets of simulations were performed, using the same values for the CMF and K_o but with different values of ζ . The CMF model is approximated in the simulations in which $\zeta = 10$, where the rheological transition occurred over the smallest melt fraction interval.

INITIATION OF CONVECTION

In all of the simulations, convection initiated with buoyant instabilities along the contact adjacent to the right margin of the computational domain. As convection developed, the instabilities propagated toward the left edge of the heated strip. The initial separation between the upwellings was approximately 20-25 m. Upward propagation of the melting front led to merging of the buoyant crystal-melt plumes. In all cases, when the cavity aspect ratio was approximately 1:1, convection was dominated by a single counterclockwise-rotating convection cell. This evolution in the style of convection proceeded most rapidly in the $\zeta = 10$ simulations.

We defined the initiation of convection to be when the heat flux across the heated strip was elevated by 1% relative to conduction. In the $\zeta = 10$ simulations (our closest approximation for the CMF model), convection began approximately 0.8 years after initiation when the boundary enclosing the region which exceeded the CMF had propagated 1.1 m from the contact. This is somewhat further than would be predicted based on buoyant thermal instabilities alone. The critical Rayleigh number (Ra_{crit}) for the onset of thermal convection in a fluid heated from below is approximately 1000 or 2000 (Turcotte and Schubert, 1982). We assume a Ra_{crit} of 2000 and invert the Rayleigh number to obtain the theoretical thickness of the melt lens at the onset of convection:

$$h = \sqrt[3]{\frac{\mu \kappa R a_{crit}}{\rho^o g \alpha \Delta T}} \quad (3.9)$$

Using typical values obtained in the simulations, we calculate the theoretical thickness of the melt lens prior to convection to be between 0.3 and 0.7 m. We have found that, for the pelite system during underplating, double-diffusive effects can delay the onset of convection and impede convective vigor (Barboza and Bergantz, 1996). Therefore, theoretical estimates based on thermal buoyancy alone may underestimate the time to the onset of convection and overestimate convective vigor during the anatexis of some crustal rocks.

We found the time duration prior to the initiation of convection was sensitive to the melt-fraction interval for the rheological transition in addition to double-diffusive effects. More gradual transitions ($\zeta < 10$) increased the amount of time and the minimum height of the melt lens before convection began. For instance, 160 years after initiation of the simulation with the most gradual rheological transition ($\zeta = 5$), the boundary enclosing the region exceeding the CMF had propagated approximately 35 m from the simulated contact with the sill. Although this is over 100 times more distant than would be predicted by Equation 3.9 for convection to begin by thermal buoyancy alone, the temperature profile in the crustal rocks was conductive. Our results indicate that classical dimensionless analysis and numerical

simulations that assume an abrupt rheological transition may significantly underestimate the time required before the onset of convection.

INFLUENCE OF RHEOLOGICAL TRANSITIONS ON THE PROGRESS OF MELTING

Figure 3.6 depicts the thermal state of the system, after 79.3 years, for simulations using three different rheological models. Viscous flow of the crystal-melt mixture, indicated by the velocity vectors, is enclosed within the region that exceeds the CMF ($f' = 0.5$). The CMF is approximately coincident with the biotite dehydration-melting isopleth. The distance above the heated strip that the isopleth propagated as a function of time is illustrated in Figure 3.7 for the three simulations. Along the right wall of the computational domain, the height was 137 m after 79.3 years for the $\zeta = 10$ simulations. For $\zeta = 8$ and $\zeta = 6$ the isopleth had propagated 120 m and 61 m respectively. The distance between the predicted positions increased as a function of time. Therefore, the relationship between convective heat transfer and the melt fraction interval for the rheological transition can change the predicted positions of isotherms by up to a factor of two.

Figure 3.8 depicts the efficiency of melt generation (E) as a function of time for the five series of simulations. $E = 2.0$ indicates that twice as much melt was generated as was predicted to have been produced at the same time by conduction alone. After 95 years, E was approximately 3.0 in the $\zeta = 10$ simulations. The

simulations using $\zeta = 5$, however, at no time produced more melt than would be predicted by conduction alone. We conclude that predictions of melting progress in high-grade igneous and metamorphic terranes may vary significantly within the range of the uncertainty in the rheological transition between solid and melt.

SENSITIVITY OF THERMAL EVOLUTION TO RHEOLOGICAL TRANSITIONS

Figure 3.9 depicts the change of the thermal flux ratio (ϑ) as a function of time for the various values of ζ . We define ϑ as the ratio of the average heat flux across the heated strip measured in a convection simulation relative to conduction. The flux ratio is thus analogous to the Nusselt number, which is often used to characterize the efficiency of convection for steady-state convective heat transport. For example, $\vartheta = 2.0$ indicates that the heat flux is twice that of conduction. Convective heat flux did not monotonically increase, which resulted in some scatter in ϑ . This observation is consistent with other experiments and simulations, where such irregularities have been attributed to the time-dependent nature of the solidus front growth rate (Bennon and Incropera, 1987b). Accordingly, the curves in Figure 3.9 are a best fit to the computed flux ratio.

After 79.3 years, $\vartheta = 5.6$, 4.6, and 2.0 for the simulations with $\zeta = 10$, 8, and 6, respectively. The $\zeta = 8$ and $\zeta = 6$ simulations resulted in a 17% and 65%

reduction, respectively, in the efficiency of convective heat transfer relative to the $\zeta = 10$ simulation. The flux ratio continuously diverged as a function of time. However, the largest change in ϑ occurred for $\zeta = 5, 6,$ and 7 . For instance, after approximately 143 years, ϑ was 7.35 and 7.13 in the $\zeta = 10$ and $\zeta = 9$ simulations, respectively. Thus, a factor of one decrease in ζ caused a 4.3% reduction in the efficiency of heat transfer. However, decreasing ζ from 8 to 7 resulted in a 33% reduction in heat transfer. Therefore, ϑ was more sensitive to changes in ζ in systems with a more gradual rheological transition.

RELATIVE IMPORTANCE OF MELT PRODUCTIVITY AND THE RHEOLOGICAL TRANSITION

In another study, we evaluated changes in the heat transfer and progress of melting as a function of the melt productivity of the protolith (increase in melt fraction with temperature) (Barboza and Bergantz, 1996). We compared the convective heat transfer during anatexis of two protolith compositions: 1) the pelitic composition adopted in this study with a non-linear increase in f' with temperature, and 2) a hypothetical composition with a linear melt productivity. The melt productivity curves for the two lithologies are compared in Figure 3.4. The melt productivity of many crustal rocks fall between these extremes (Bergantz and Dawes, 1994). The two compositions thus represent end-members for a continuum of possible

melt productivities from crustal rocks. The various boundary and initial conditions of the simulations were identical to those of this study.

Figure 3.9 depicts ϑ as a function of time for the hypothetical composition with linear melt productivity and $\zeta = 10$. This figure illustrates that convective heat transfer may be significantly suppressed during melting of less fertile protoliths. For example, after 79.3 years $\vartheta = 2.0$ for the hypothetical protolith with the linear melt productivity. For the model pelite at the same time, ϑ was 280% larger. However, the variability in ϑ resulting from the tested rheological transitions exceeds the predicted variability as a function of protolith composition. Adopting $\zeta = 5$ for the model protolith composition, for example, suppressed convection to the extent that the calculated heat flux was equivalent to conduction through the duration of the simulations. We conclude that, for a wide range of fertile crustal rocks, the rheological transition between solid and melt may be one of the dominant factors controlling convective vigor in crustal magmatic systems.

CONCLUSIONS

The results of low-melt fraction deformation experiments indicate that the rheological transition between crystal-supported to fully fluid behavior may be more gradual than stipulated by the CMF model. However, it is uncertain what impact

this may have on interpretations of geologic processes that appeal to the loss of contiguity at the CMF.

The hybrid model of Oldenburg and Spera (1992) may be easily adapted to accommodate a more gradual rheological transition. Using the modified Oldenburg and Spera (1992) model, we conducted numerical simulations to evaluate the relationship between crustal anatexis, convective heat transfer, and the rheological transition. A more gradual rheological transition may significantly delay the initiation of convection. An insignificant amount of convective heat transfer was observed in the $\zeta = 5$ simulations, even though the boundary enclosing the region which exceeded 50% melt had propagated 34.7 m from the contact. Heat flux was between one ($\vartheta = 1.0$) and eight times ($\vartheta = 8.0$) that of conduction alone, depending on the selection of rheological models.

Both the rheological transition and the lithology of the protolith contribute to convective heat flux. Two protolith compositions were analyzed which bracket the melt productivity of a wide range of common crustal rocks. We found that convective heat transfer and melting were more strongly influenced by the selection of rheological transition model than by the melt productivity of the protolith. We conclude that the mechanical behavior of high-melt-fraction igneous and metamorphic systems may be a dominant factor influencing the generation of felsic melts.

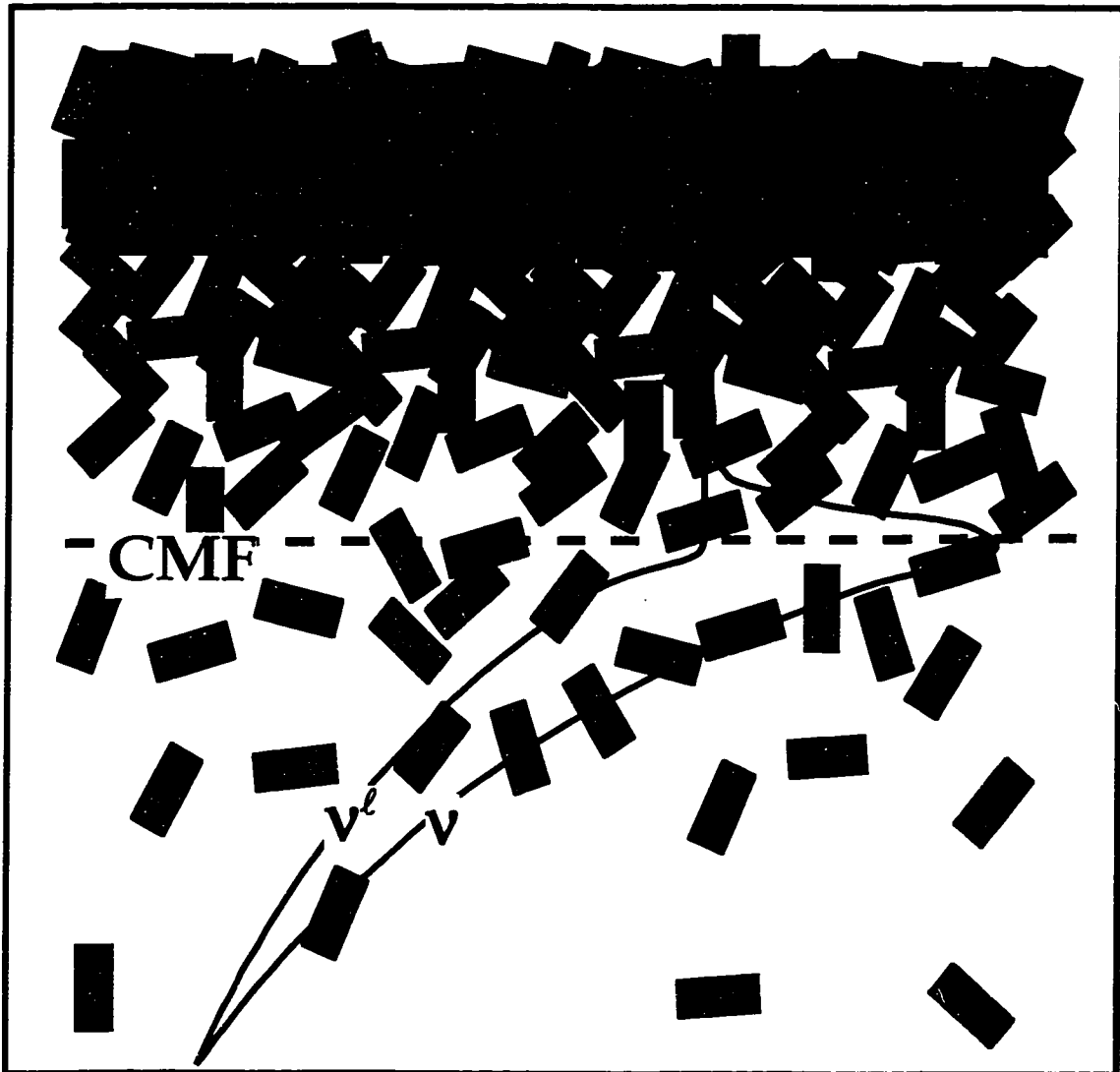


Figure 3.1. Schematic depiction of the CMF model. When the local melt fraction (f^l) is less than the CMF, the melt percolates through a rigid solid matrix. When the CMF is exceeded, the solids are suspended in the melt and increase the effective kinematic viscosity of the mixture (v) relative to the crystal-free melt (v^e).

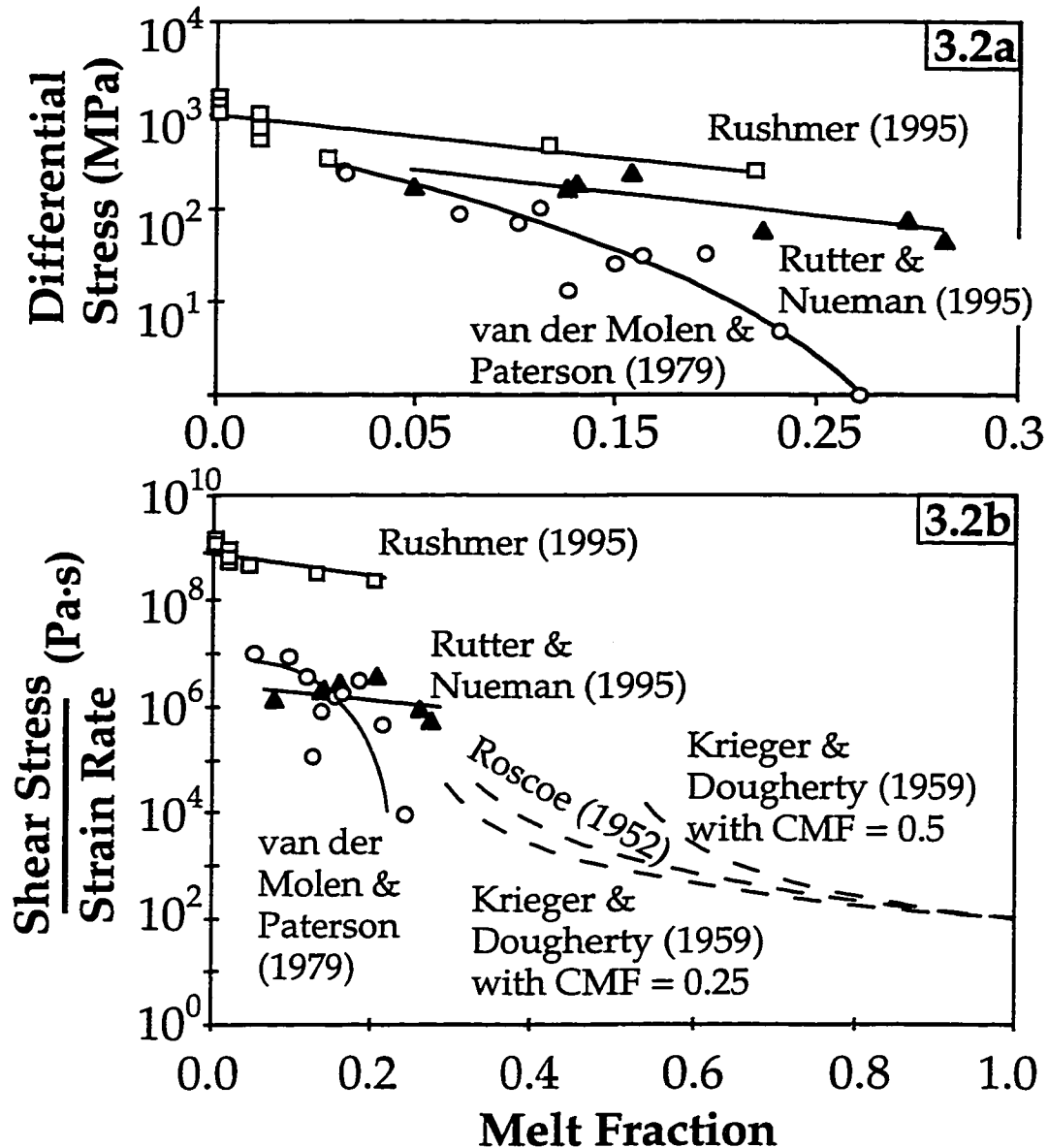


Figure 3.2. Summary of experimental results related to the CMF. Figure 3.2a depicts the maximum differential stress prior to sample failure attained in three low-melt fraction deformation experiments. A large decrease in rock strength as a function of melt fraction was observed in the experiments of van der Molen and Paterson (1979), leading to the inference of the CMF. This change in rheological behavior was not observed in the experiments of Rutter and Nueman (1995) and Rushmer (1995). Figure 3.2b depicts the effective viscosity (shear stress/strain rate) of several experiments. This figure also depicts empirical and theoretical relationships for the viscosity of viscous suspensions (Krieger and Dougherty, 1959; Roscoe, 1952).

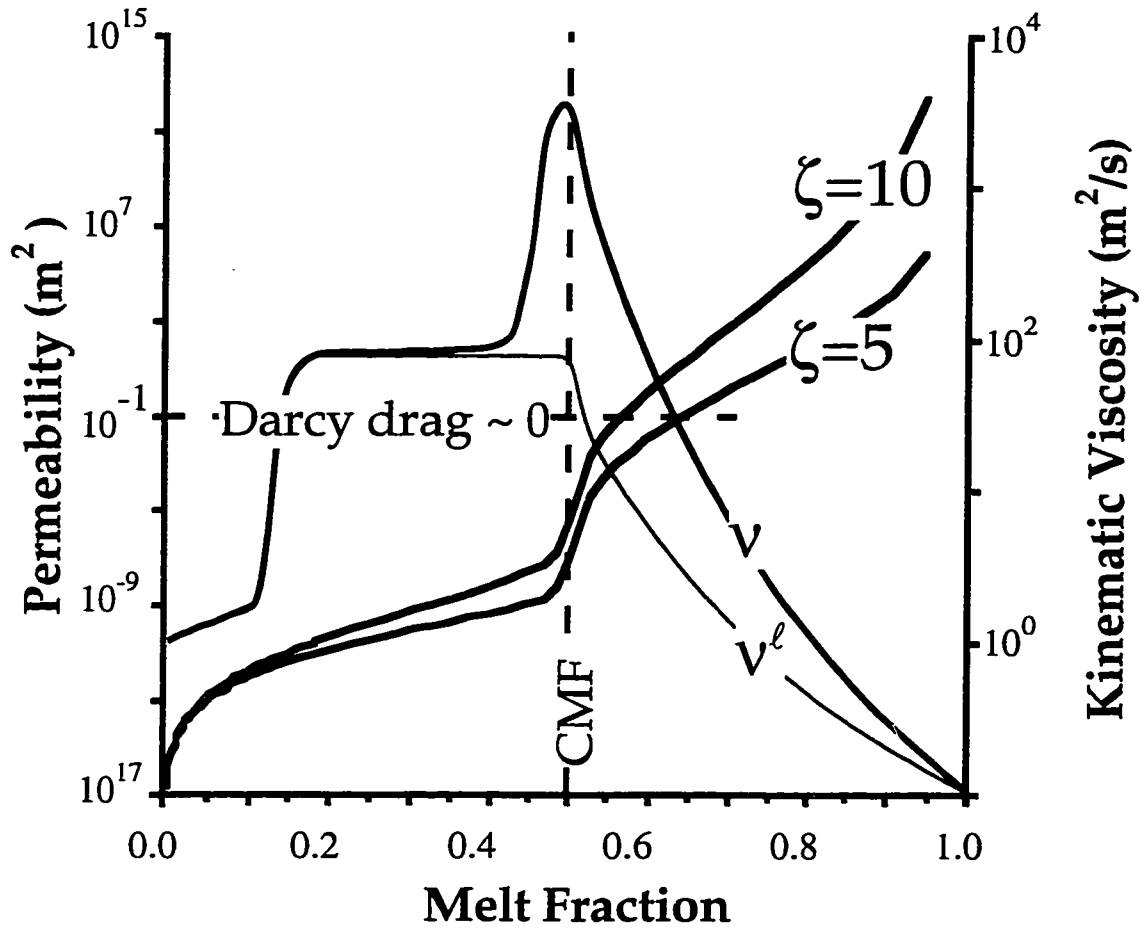


Figure 3.3. Plot of the kinematic viscosity and permeability against melt fraction. The two viscosity curves represent the viscosity of the melt and the effective viscosity of the melt + crystal mixture (v). v^l and f^l are both functions of temperature, whereas v is a function of both temperature and f^l . The two permeability curves represent the CMF model ($\zeta=10$) and the most gradual rheological transition considered ($\zeta=5$). The four other rheological transition models are bounded by these limits. Viscous drag imposed on the interstitial melt approaches zero where the permeability curves intersect the Darcy drag ~ 0 line.

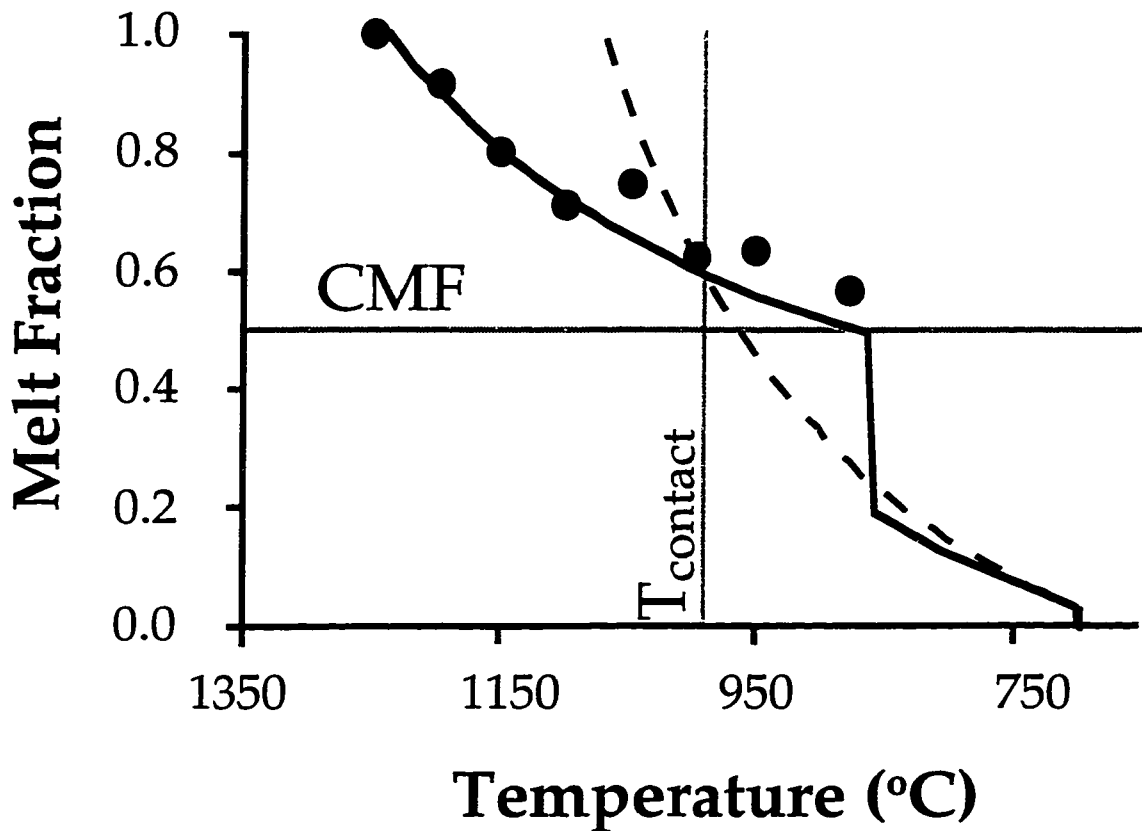


Figure 3.4. Plot of the relationship between temperature and melt fraction (melt productivity) for the two lithologies considered in the study. The solid line illustrates the melt productivity of the model metapelite based on the composition considered by Vielzeuf and Holloway (1988). The dashed line is the hypothetical crustal composition with more linear melt productivity. The circles are the experimental data of Vielzeuf and Holloway (1988). The melt productivity of the hypothetical crustal composition was constructed so that both systems had the same melt fraction at the contact temperature (T_{contact})

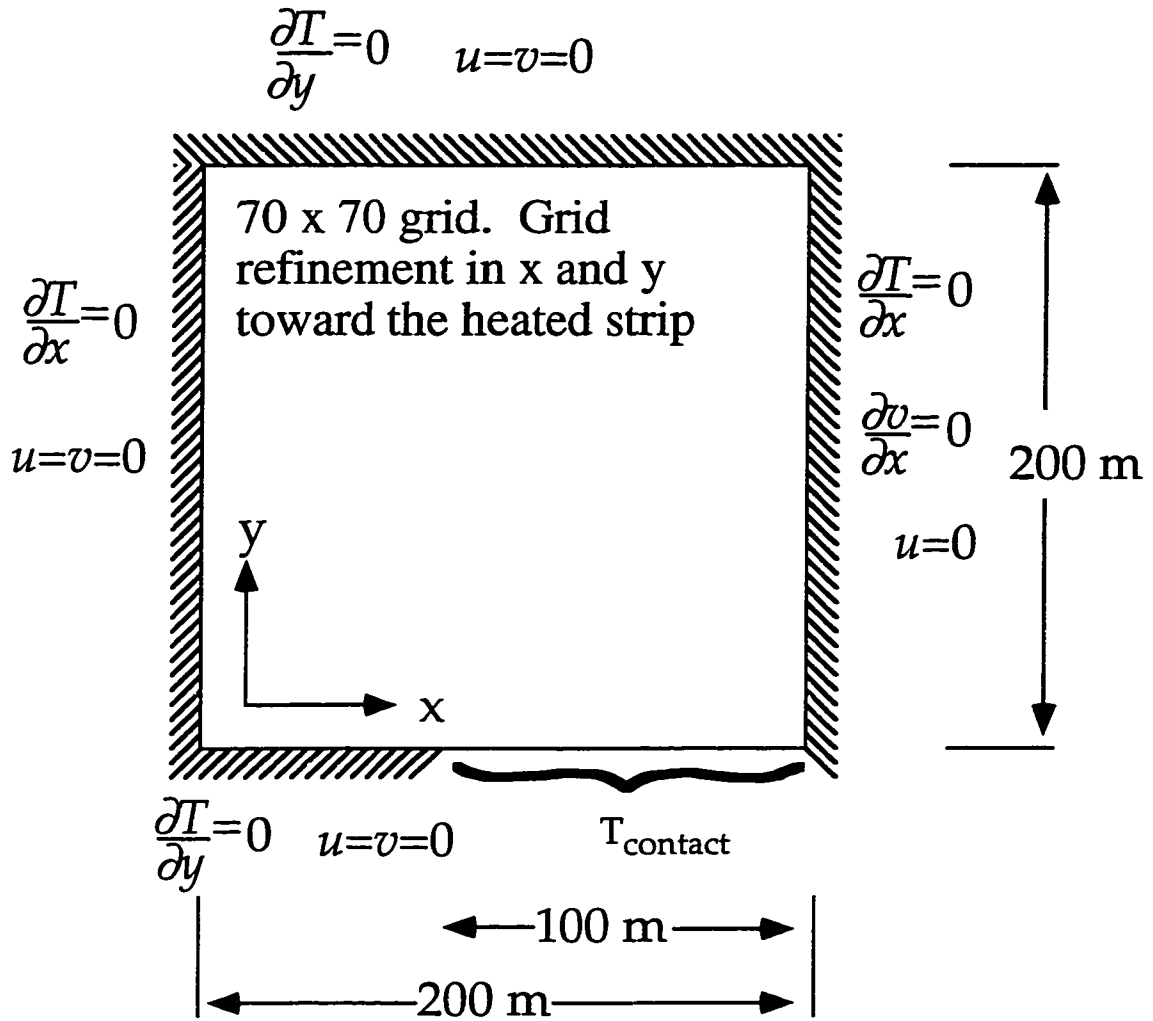


Figure 3.5. Schematic of the computational domain. We used a 70 x 70 node grid with a refinement factor of 1.6 in x and 1.4 in y.

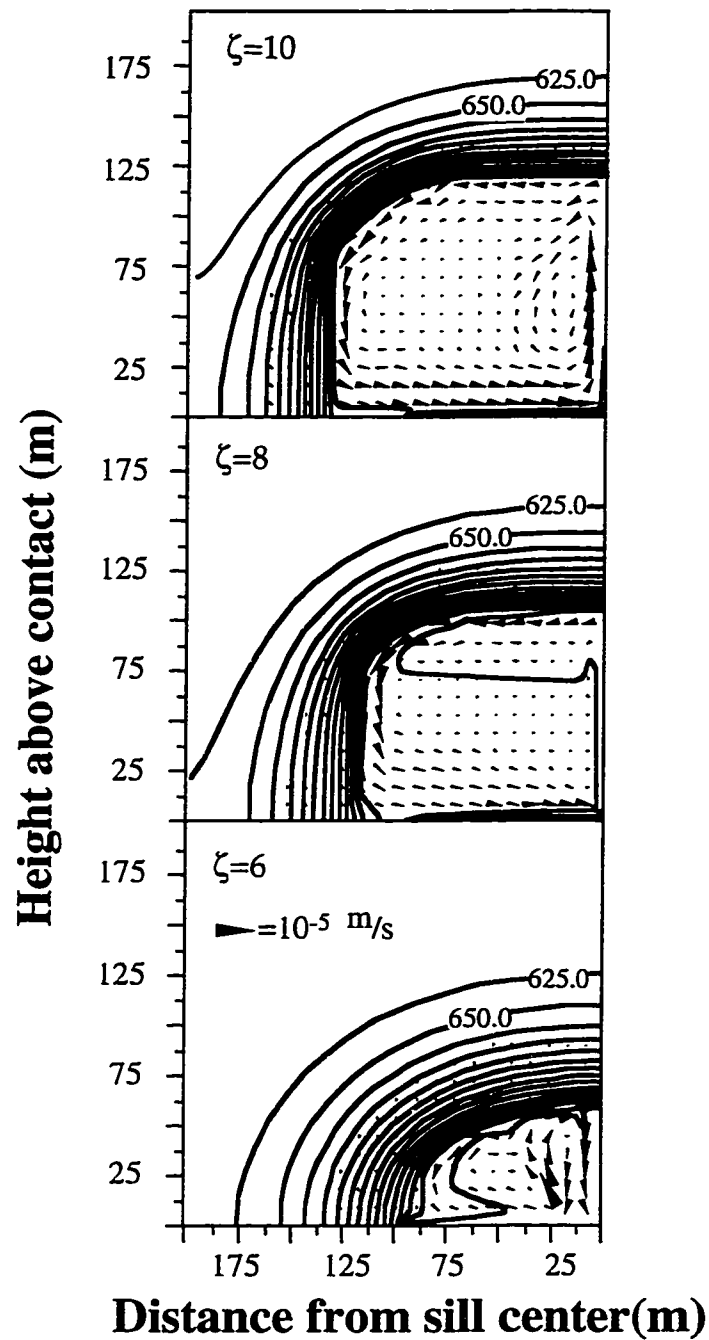


Figure 3.6. Sample results 79.3 years after the initiation of the simulations with $\zeta=10$, 8, and 6. Contours are of temperature in $^{\circ}\text{C}$. Viscous flow, indicated by the velocity vectors, is enclosed by the region exceeding the CMF ($f^l=0$). Typical melt velocities in the porous flow regime are six to eight orders of magnitude less than viscous flow velocities in the mixture.

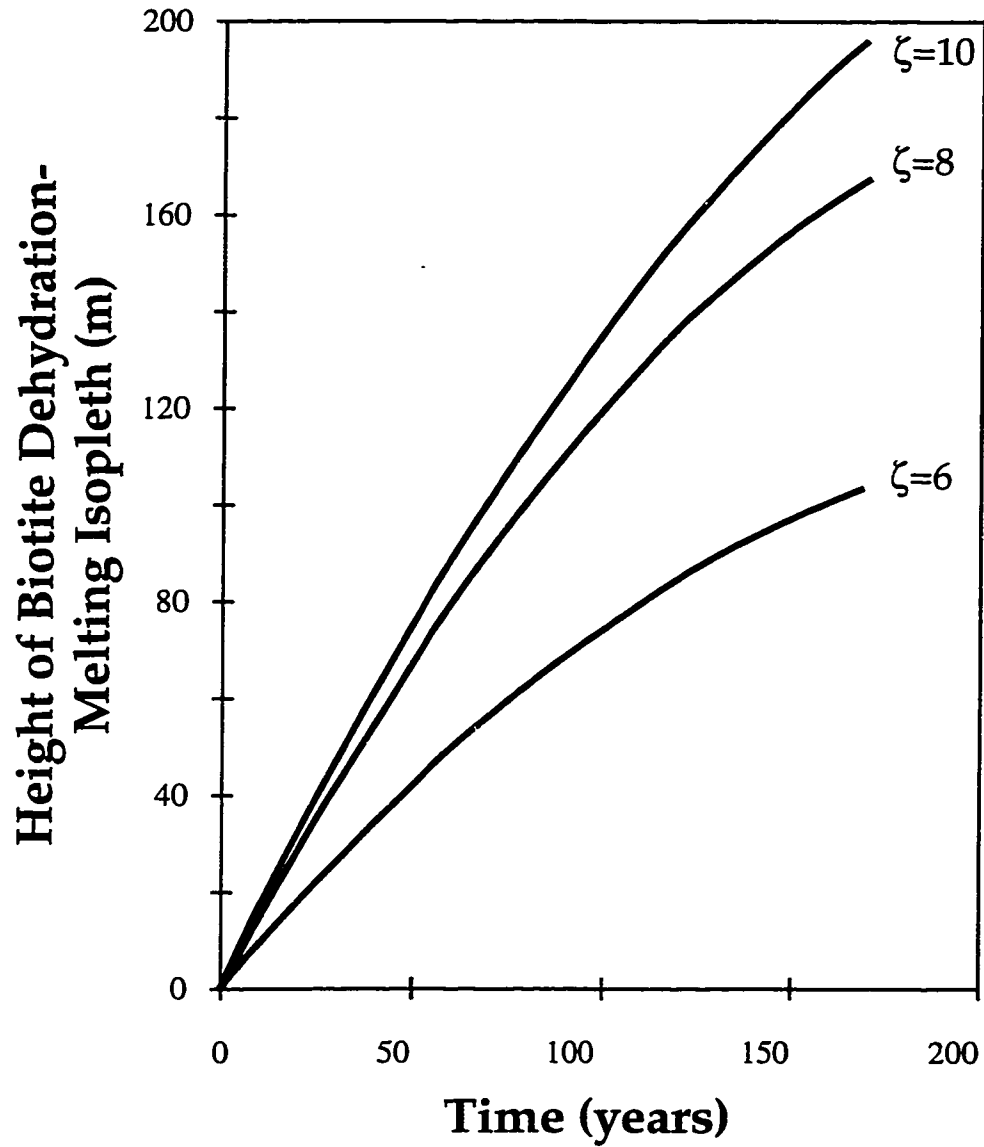


Figure 3.7. Distance the biotite dehydration isopleth had propagated as a function of time, for simulations with $\zeta=10, 8,$ and $6.$

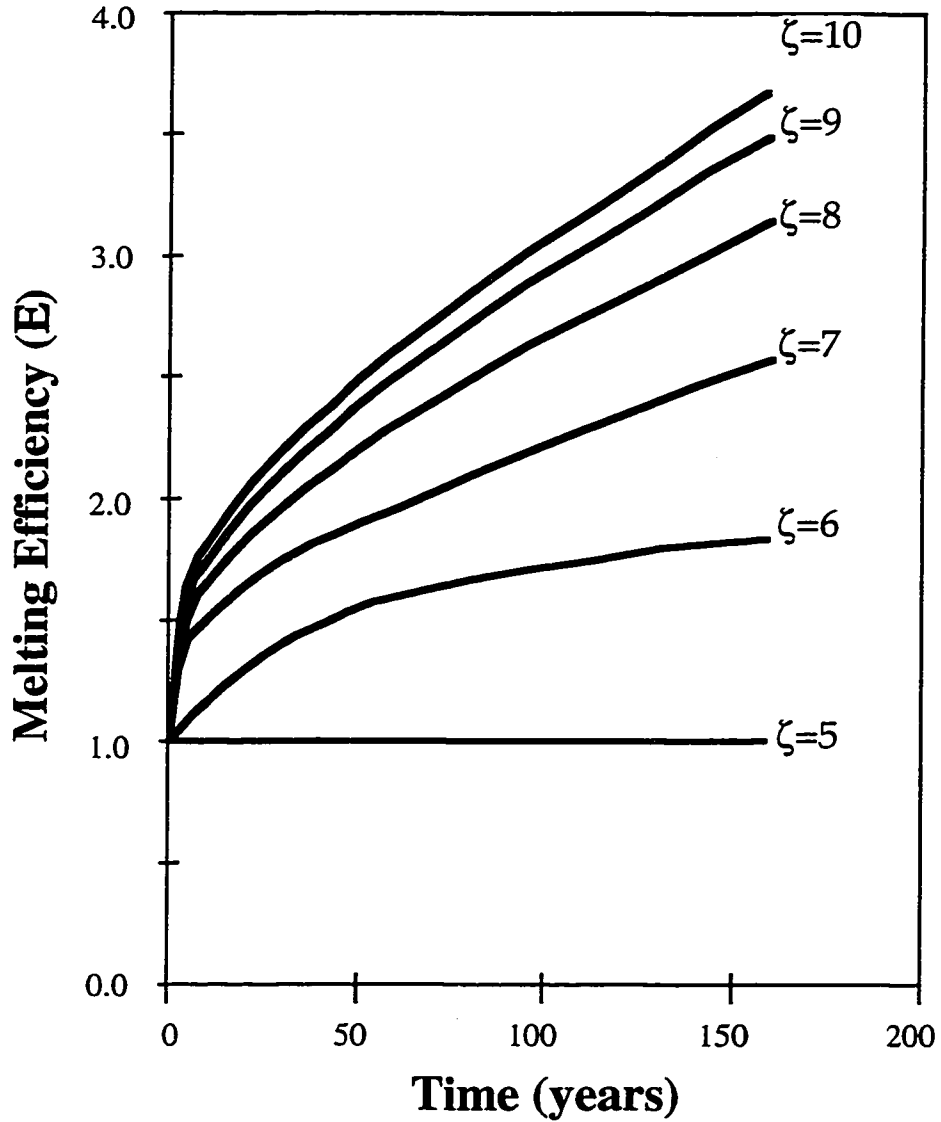


Figure 3.8. Melting efficiency (E) as a function of time predicted by the simulations with the various rheological models. We define E as the mass of melt generated in the simulations relative to the mass of melt predicted to be generated in the absence of convection.

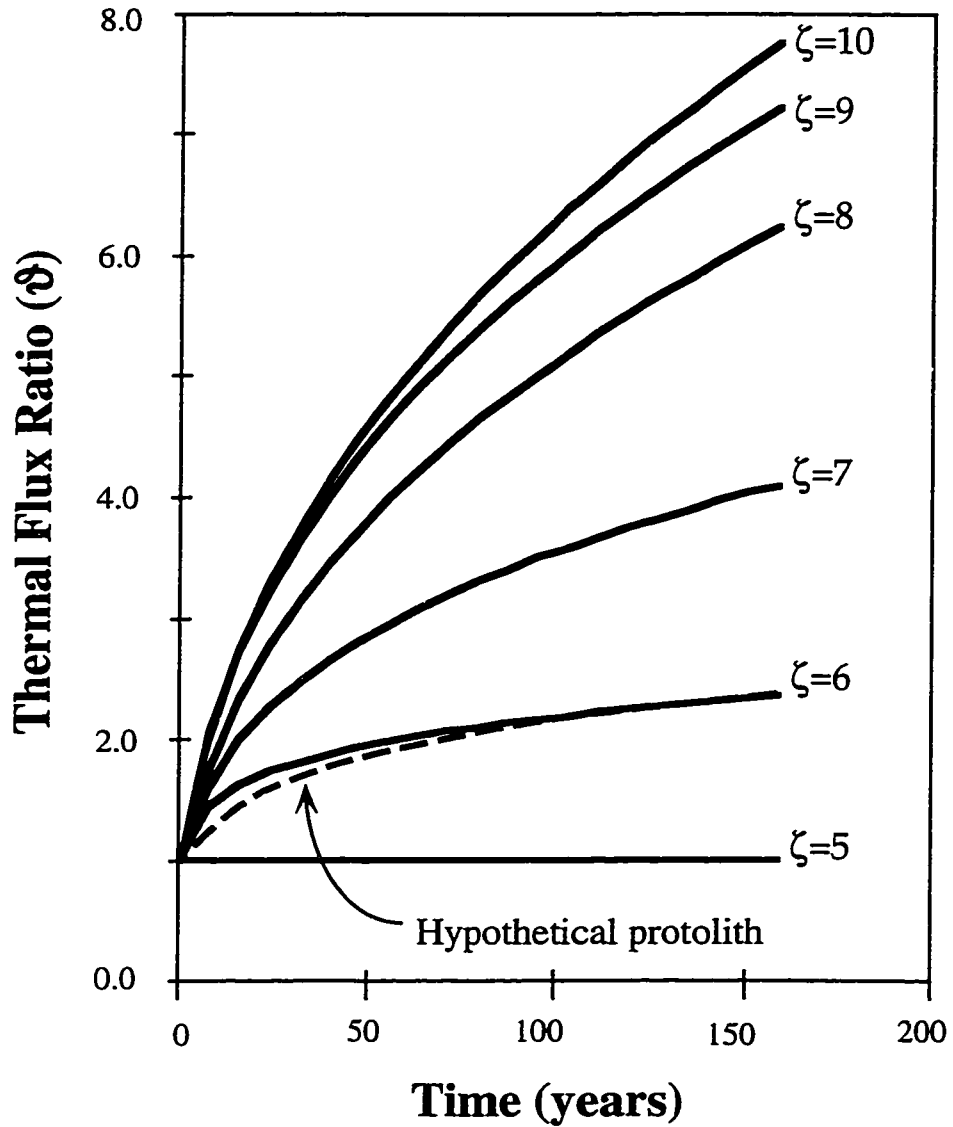


Figure 3.9. Heat flux ratio (ϑ) as a function of time predicted by the simulations with the various rheological models. We define ϑ as the heat flux across the heated strip calculated during the simulations relative to that predicted in the absence of convection. The dashed line indicates ϑ for the hypothetical composition with the linear melt productivity and $\zeta = 10$.

Table 3.1: Nomenclature.

| <i>Symbol</i> | Description | Units |
|---------------|--|-------------------|
| c_p^a | heat capacity at constant pressure constituent a | J/kg·K |
| C | solute concentration in the mixture | dimensionless |
| C^a | solute concentration in constituent a | dimensionless |
| D^a | diffusion coefficient of constituent a | m ² /s |
| f^a | mass fraction constituent a | dimensionless |
| g^a | volume fraction constituent a | dimensionless |
| g_i | i th component of gravitational acceleration | m/s ² |
| k | thermal conductivity | J/s·m·K |
| K_i | i th component of anisotropic permeability | m ² |
| L | specific latent heat | J/K |
| p | static pressure or isotropic stress mixture | Pa |
| t | time | s |
| T | temperature | °C |
| v_i^a | i th component of mixture velocity constituent a | m/s |
| β_C^a | coefficient of solutal expansion constituent a | 1/K |
| β_T^a | coefficient of thermal expansion constituent a | 1/K |
| E | melting efficiency | dimensionless |
| ϑ | heat flux ratio | dimensionless |
| γ^a | mass constituent a per unit volume constituent a | kg/m ³ |
| Γ | permeability switching function | dimensionless |
| κ | thermal diffusivity | m ² /s |
| Φ | viscosity switching function | dimensionless |
| ρ | mass of mixture per unit volume mixture | kg/m ³ |
| ρ^a | mass constituent a per unit volume mixture | kg/m ³ |
| μ | dynamic viscosity mixture | Pa·s |
| μ^a | dynamic viscosity constituent a | Pa·s |
| ν | kinematic viscosity mixture | Pa·s |
| ν^a | kinematic viscosity constituent a | Pa·s |

Table 3.2: Values for the various material properties and for the initial and boundary conditions used in the numerical simulations.

| Thermophysical and rheological properties | |
|--|------------------------|
| Specific heat (J/kg·K) | 1.04×10^3 |
| Thermal conductivity (W/m·K) | 1.9 |
| Density (kg/m ³) | 2.507×10^3 |
| Kinematic viscosity (m ² /s) | see text |
| Schmidt number (v^{ℓ}/D) | 1.0×10^6 |
| Latent heat (J/kg) | 1.0×10^5 |
| Permeability coefficient (m ²) | 5.56×10^{-10} |
| Thermal expansion coefficient (K ⁻¹) | 1.05×10^{-4} |
| Solutal expansion coefficient | 1.55×10^{-1} |
| Critical melt fraction | 0.5 |
| Initial and boundary conditions | |
| Pelite starting composition | 0.325 |
| Initial temperature (°C) | 600.0 |
| Contact temperature (°C) | 1000.0 |
| Total time duration of simulations (s) | 5×10^9 |

CHAPTER 4: REGIONAL GRANULITE-FACIES METAMORPHISM IN THE IVREA ZONE: IS THE MAFIC COMPLEX THE SMOKING GUN OR A RED HERRING?

INTRODUCTION

One model for the large-ion lithophile element (LILE) depletion of crustal rocks during granulite-facies metamorphism is that extraction of melt attends emplacement of mafic magma under or near the base of the continental lower crust (magmatic under/intraplating) (Harley, 1989). In this model, mantle magmatism, granulite-facies metamorphism, and crustal anatexis are coupled processes that result in chemical differentiation of continental crust. The Ivrea zone (Southern Alps, northern Italy) is commonly considered to be the pre-eminent example of regional granulite-facies metamorphism and crustal anatexis accompanying magmatic under/intraplating. Within the Ivrea zone, mantle-derived magma intruded metasedimentary and meta-igneous rocks while the section was in the lower crust (Rivalenti et al., 1975; Voshage et al., 1990). Emplacement of mafic magmas into the supracrustal section has been traditionally interpreted as having caused or accompanied the thermal maximum during regional granulite-facies metamorphism (Rivalenti et al., 1980; Schmid and Wood, 1976; Sills, 1984).

In this study, we provide evidence supporting an alternative model in which the emplacement of the Mafic Complex occurred subsequent to the imposition of the regional pattern of metamorphic isograds (Zingg et al., 1990). Therefore, the heat supplied by the exposed portion of the Mafic Complex is unlikely to have caused regional granulite-facies metamorphism in the Ivrea zone. Metamorphism and anatexis of only weakly depleted, amphibolite-facies metasedimentary and meta-igneous rocks that can be associated unequivocally with emplacement of the Mafic Complex occur only within a ~2km wide zone along the upper parts of the intrusion. If the Mafic Complex represents the exposed portion of a magmatic underplate, extensive regional metamorphism and anatexis may not inexorably accompany magmatic under/intraplating. Studies postulating that such regional effects necessarily accompany magmatic under/intraplating (Campbell and Turner, 1987; Huppert and Sparks, 1988) may underestimate the amount of basalt required to achieve the degree of melt depletion inferred in regional granulite terrains such as the Ivrea zone.

GEOLOGIC FRAMEWORK

Most regional studies interpret the Ivrea zone as a cross-section through attenuated continental lower crust (Burke and Fountain, 1990). There are three major lithologic divisions in the Ivrea zone (Figure 4.1): 1) supracrustal rocks of the Kinzigite Formation; 2) mantle peridotite; and, 3) the Mafic Complex. The lowest grade rocks crop out along the southeastern margin of the Ivrea zone and contain

upper amphibolite-facies assemblages (Zingg, 1980). Granulite-facies rocks are exposed in Val Strona, indicating that metamorphic grade increases toward the northwest, in accordance with *P-T* estimates derived using geothermobarometry (Henk et al., 1997; Schmid and Wood, 1976; Sills, 1984).

The amphibolite-facies portion of the Kinzigite Formation consists of migmatitic metapelite and metapsammite, with subordinate metacarbonate and metabasite (Sills, 1984). The texture of the metapelite changes from lepidoblastic to granoblastic due to replacement of muscovite and biotite by K-feldspar and garnet with increasing grade (Zingg, 1980). In granulite-facies rocks, massive quartz + hypersthene ± garnet granulite ('charnockite'), metacarbonate, and metabasite are interlayered with granoblastic graphite + sillimanite + garnet gneiss ('stronalite'), interpreted to be residual material from the partial melting of metapelite.

The Mafic Complex is up to 10 km thick and comprises gabbroic to leuco-dioritic rocks intercalated with ultramafic rocks and thin layers of supracrustal rocks (Quick et al., 1994). The supracrustal rocks, referred to as septa, consist of < 1 m to ~100 m thick layers of depleted granulite interpreted to be rocks excavated from the roof of the Mafic Complex during emplacement (Sinigoi et al., 1996). Four main rock types are recognized in the septa: a) 'stronalite'; b) 'charnockite'; c) calc-silicate rock; and, d) minor metabasite (Rivalenti et al., 1975). Lenses of tonalite to granodiorite diatexite (≤ 200 m thick) containing blocks and schlieren of metabasite and metapelite separate the Mafic Complex from the overlying Kinzigite Formation (Bürgi and Klötzli, 1990; Quick et al., 1994). The composition of the diatexite may be

the product of chemical interaction between melts of the Mafic Complex and the roof zone wall rocks (McCarthy and Patiño Douce, 1997).

THE RELATIONSHIP BETWEEN BASALTIC MAGMATISM, CRUSTAL ANATEXIS, AND GRANULITE-FACIES METAMORPHISM

FIELD AND PETROLOGIC EVIDENCE

Field and petrologic observations motivate an interpretation that the Mafic Complex intruded late relative to the imposition of the regional pattern of metamorphic isograds. Based on a compilation of previous petrographic work, Zingg (1980) mapped mineral isograds that represent prograde reactions produced during regional metamorphism up to granulite facies (Figure 4.1). Two of these isograds are the muscovite to K-feldspar isograd in sillimanite-bearing paragneiss and the first appearance of clinopyroxene + orthopyroxene in metabasite (Figure 4.1). Zingg (1980) noted that the distribution of mineral assemblages in metapelite and metabasite within septa in the Mafic Complex is not continuous with the regional isograd pattern. Thus, the northeastern margin of the Mafic Complex cuts across the strike of the prograde metamorphic isograds at a high angle. We concur with the inference of Zingg et al. (1990), that the disposition of the prograde metamorphic isograds in the Ivrea zone is consistent with granulite-facies conditions imposed prior to the emplacement of the upper parts of the Mafic Complex.

Additionally, if emplacement of the Mafic Complex supplied the heat for regional metamorphism in the Kinzigite Formation, granulite-facies mineral assemblages should characterize rocks close to the contact. However, granulite-facies assemblages are predominantly confined to crustal levels that record P of > 6 kbar in the Val Strona region on the NE side of the Mafic Complex. In Val Sesia (Figure 4.1), plagioclase-bearing metabasite contains the upper amphibolite-facies assemblage hornblende \pm biotite \pm clinopyroxene (Zingg, 1980). The regional increase in metamorphic grade thus correlates with the across strike increase from ~ 4 to ~ 9 kbar between the southeastern (CMB Line) and northwestern (Insubric Line) tectonic boundaries of the Ivrea zone (Henk et al., 1997; Sills, 1984), rather than proximity to the Mafic Complex. Thus, the distribution of granulite-facies rocks in the Ivrea zone is inconsistent with the emplacement of the Mafic Complex having caused regional granulite-facies metamorphism.

Finally, cordierite, hercynite, and relict andalusite appear in an approximately 2km wide zone (Figure 4.1) surrounding the upper parts of the Mafic Complex south of Val Sesia (Zingg, 1980). In this zone, cordierite and hercynite overprint the assemblage biotite + garnet + sillimanite in metapelite. This suggests that the rocks proximal to the Mafic Complex south of the Val Sesia region reached final equilibration at a lower pressure than those along strike in lower Val Strona. We infer the local thermal event associated with emplacement of the upper parts of the Mafic Complex overprinted the former amphibolite- to granulite-facies regional

metamorphic zonation during decompression of the region from pressures attained during the regional thermal maximum.

GEOCHEMICAL EVIDENCE

The composition of 'stronalite' can be explained by extraction of 20-40 wt% of a granite component from the amphibolite-facies metasedimentary rocks (Schnetger, 1994; Sighinolfi and Gorgoni, 1978). As these rocks exhibit a limited range in bulk chemical composition, variability in protolith chemistry probably was not a first order control on anatexis (Schnetger, 1994). The extent of depletion of 'stronalite' correlates with the across-strike increase in metamorphic grade (Schmid and Wood, 1976; Sighinolfi and Gorgoni, 1978; Zingg, 1980) and original crustal depth to the northwest in Val Strona (Henk et al., 1997; Sills, 1984).

There is no apparent increase in the extent of depletion of 'stronalite' with proximity to the Mafic Complex. Plots of wt.% K versus K/Rb ratios of 'stronalite' and amphibolite-facies metapelite are shown in Figure 4.2. In agreement with general compositional trends in granulite-facies rocks (Rudnick and Presper, 1990), the K/Rb ratio varies inversely with K content below 1.0 wt.% K, reflecting the partitioning of K and Rb between crystalline and fluid or melt phases (Fowler, 1986). K/Rb ratios in 'stronalite' with > 2.0 wt. % K are similar to amphibolite-facies metapelite. 'Stronalite' with < 2.0 wt. % K possess K/Rb ratios approaching 1000, reflecting depletion relative to more fertile metapelite. Significant compositional overlap exists,

however, for 'stronalite' contained within septa in the Mafic Complex and within the granulite-facies portion of Val Strona (Figure 4.2). Assuming 'stronalite' represents the residues after anatexis of metapelite (Schnetger, 1994; Sighinolfi and Gorgoni, 1978), the similar elevation in the K/Rb ratio may reflect similar levels of melt extraction. According to this view, there is no significant increase in the amount of melt extracted from 'stronalite' with proximity to the Mafic Complex.

IMPLICATIONS - BOTH REGIONAL AND CONTACT MELTING

The inferred composition of crustal component assimilated by the parental magmas for the Mafic Complex is consistent with regional metamorphism predating emplacement. Nd, Sr, and $\delta^{18}\text{O}$ data indicate that the magmas of the Mafic Complex were contaminated by assimilation of variable proportions of crustal material (Sinigoi et al., 1994; Voshage et al., 1990). Sinigoi et al. (1994) suggest that this crustal contaminant was likely derived from metapelitic rocks excavated from the supracrustal section and incorporated as septa within the Mafic Complex during emplacement. The unusually high Ba/K and Ba/Rb ratios of the Mafic Complex require a contaminant from the overlying supracrustal section that was depleted in Rb^+ and K^+ prior to emplacement of the Mafic Complex (Sinigoi et al., 1994). Sinigoi et al. (1994) suggested that depletion may have occurred during regional metamorphism prior to emplacement, or that heat released during crystallization of the Mafic Complex parental magmas may have induced anatexis of the overlying crustal rocks

(Voshage et al., 1990). However, if granulite similar to that in Val Strona were partially assimilated by the Mafic Complex, it would be unnecessary to call on syn-intrusion anatexis as the progressive removal of Rb⁺ and K⁺ with increasing grade in the granulites is well-documented (Sighinolfi and Gorgoni, 1978).

Bulk compositions of the regional granulite-facies rocks ('stronalite') of upper Val Strona are consistent with the extraction of 20-40 vol.% granite melt (Schnetger, 1994) during regional granulite-facies metamorphism. In contrast, leucosomes within metapelitic migmatite proximal to the roof of the Mafic Complex are leucotonalite in composition (Figure 4.3). The contrast in leucosome composition proximal to the Mafic Complex with the putative composition of melt lost from 'stronalite' suggests multiple episodes of anatexis in the Kinzigite Formation. Lensoidal bodies of tonalite to granodiorite diatexite ≤ 200 m thick are conformable with the contact between the Mafic Complex and the Kinzigite Formation (Quick et al., 1994) suggesting an increase in the volume of melting closer to the local heat source. We infer that heat released from the Mafic Complex caused the melting that produced the lensoidal tonalite to granodiorite diatexite and the leucotonalite leucosomes in the Kinzigite Formation. The K-poor compositions of these products of metapelite anatexis could imply either high $a(\text{H}_2\text{O})$ melting (Conrad et al., 1988; Whitney and Irving, 1994) or hybridization of crustal rocks with melt from the Mafic Complex (McCarthy and Patiño Douce, 1997). In either case, leucotonalite leucosomes are not volumetrically significant and are restricted to Kinzigite Formation overlying the Mafic Complex coincident with the appearance of cordierite, hercynite and andalusite in the restite

assemblage. Thus, although a granite melt is inferred to have been extracted from the Kinzigite Formation to produce 'stronalite', only local anatexis that produced tonalite to granodiorite diatexite along the contact and leucotonalite leucosomes in the migmatites above can be directly linked to the emplacement of the Mafic Complex.

DISCUSSION

Five observations suggest that emplacement of the Mafic Complex did not cause regional granulite-facies metamorphism in the Ivrea zone. First, the northeastern margin of the Mafic Complex cuts across the strike of regional prograde metamorphic isograds at a high angle. Along with the regional distribution of granulite-facies rocks, this observation indicates supracrustal rocks in the Ivrea zone equilibrated under amphibolite- to granulite-facies conditions prior to emplacement of the Mafic Complex. Second, mineral assemblages in metapelite proximal to the intrusion preserve evidence of a low-pressure, high-temperature metamorphic overprint of the former amphibolite- to granulite-facies regional metamorphic zonation. Third, the extent of depletion of metasedimentary rocks in the Ivrea zone correlates with increasing crustal depth, while there is no apparent increase in the depletion of granulite with proximity to the Mafic Complex. Fourth, the composition of the Mafic Complex contaminant is consistent with anatexis and melt extraction in the supracrustal rocks having occurred prior to final emplacement of the Mafic Complex. Finally, the composition of leucosomes overlying the Mafic Complex is

inconsistent with the composition of the melt inferred to have been extracted from the Kinzigite Formation to form the depleted granulite-facies rocks in upper Val Strona. These observations are explained if regional granulite-facies metamorphism preceded emplacement of the Mafic Complex.

CONCLUSIONS

In the Ivrea zone, the regional granulite-facies episode, producing widespread anatexis preceded emplacement of the Mafic Complex and was not necessarily related to magmatic underplating. Emplacement of the Mafic Complex appears to have generated only a modest volume of melt that produced tonalite to granodiorite diatexite and leucotonalite leucosomes during contact metamorphism in a spatially restricted zone overlying the intrusion. This narrow zone of contact metamorphism and anatexis suggests that calculated amounts of basaltic input to magmatic systems based on mass and enthalpy balances from continental magmatism (Grunder, 1995) likely are minimum estimates. If the localized partial melting and metamorphism we associate with emplacement of the Mafic Complex is representative of magmatic under/intraplating, voluminous intrusion of mantle-derived magma does not inexorably imply regional-scale metamorphism and anatexis of the lower continental crust. Reference to studies that call on widespread anatexis and regional granulite-facies metamorphism to accompany magmatic under/intraplating (Campbell and Turner, 1987; Huppert and Sparks, 1988) should be tempered by an awareness

that such effects are not apparent in the Ivrea zone, which has been regarded as the putative example of such a process.

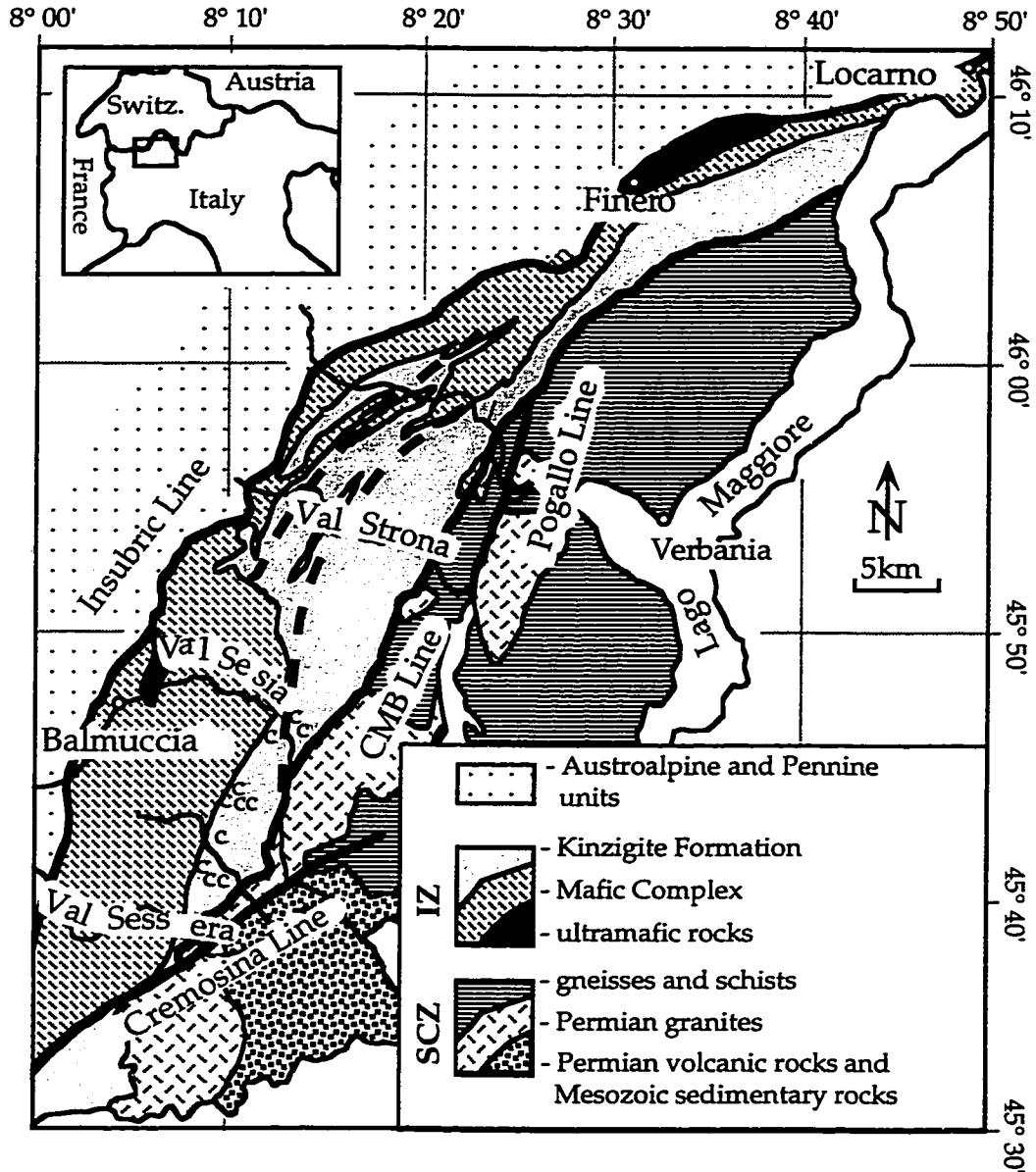


Figure 4.1. Simplified geologic map of the Southern Alps west of Lago Maggiore (Zingg, 1980). Inset shows location of study area in northern Italy. The abbreviations "IZ" and "SCZ" refer to the Ivrea zone and Strona-Ceneri zone, respectively. The symbol "Mu - out" represents muscovite - K-feldspar isograd in metapelite, and "Opx - in" represents first appearance of orthopyroxene in metabasite (Zingg, 1980). "C" indicates cordierite occurrences. The "CMB Line" indicates the Cossato-Mergozzo-Brissago Line, a purported late Paleozoic fault separating the Ivrea and Strona-Ceneri zones (Boriani et al., 1977).

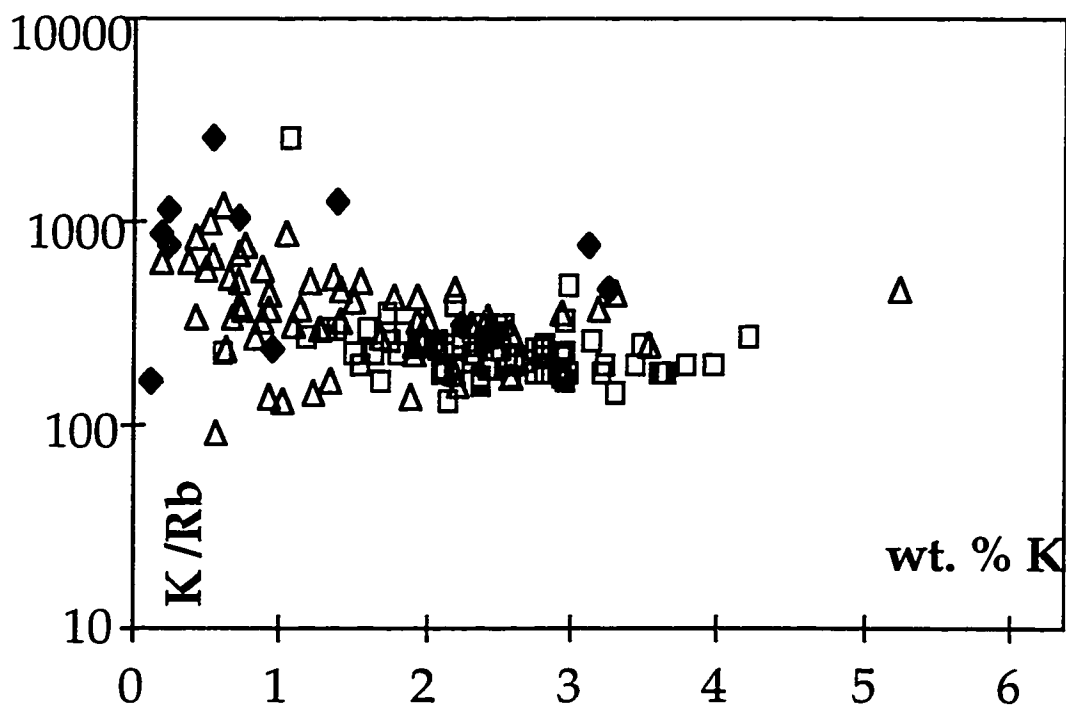


Figure 4.2. K/Rb ratio vs. wt.% K. K: "Stronalite" in Val Strona (open triangles); "stronalite" within the Mafic Complex (filled diamonds); and amphibolite-facies, sillimanite-bearing metapelite (open squares). See text for details. Data include our own analyses, along with those of Sighinolfi (1969), Mehnert (1975), Rivalenti et al. (1975), Dostal and Capedri (1979), Schnetger (1994), Sinigoi et al. (1994), and Sinigoi et al. (1996).

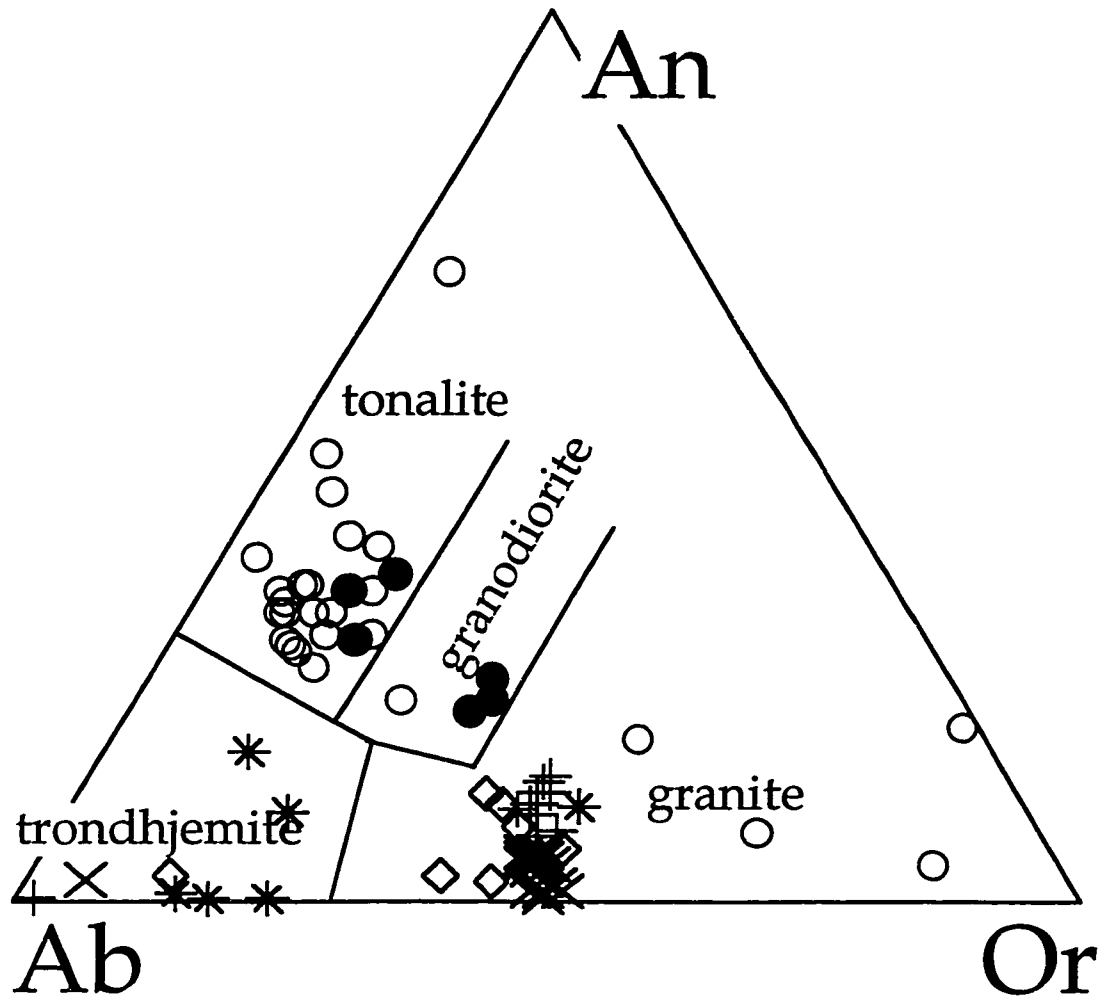


Figure 4.3. Classification of granitoid rocks in the Ivrea and Strona-Ceneri zones according to normative An-Ab-Or compositions. Open and closed circles represent leucotonalite leucosomes and tonalite to granodiorite diatexite, respectively. The composition of Permian granites within the Strona-Ceneri zone ("◊" = Roccapietra granite, "X" = Baveno pink granite, "+" = Montorfano granite, and "*" = Mergozzo granite) are similar to the inferred composition of crustal melt extracted during regional metamorphism (Schnetger, 1994). Data include our own analyses along with those of Boriani et al. (1992).

CHAPTER 5: METAMORPHISM AND ANATEXIS IN THE MAFIC COMPLEX CONTACT AUREOLE, IVREA ZONE, NORTHERN ITALY

INTRODUCTION

One model to enhance the total thermal budget of the lower continental crust resulting in regional granulite-facies metamorphism and generation of Y- and HREE depleted granitoids (Ellis, 1987) involves the accretion of mantle-derived magmas at or near the base of the crust (Bohlen, 1987; Wells, 1980). A consequence of this model is the production and extraction of partial melt, which results in internal stratification and chemical differentiation of continental crust and large-ion-lithophile element (LILE) depletion. In tectonic settings such as Phanerozoic extensional terranes (Fountain, 1989; Gans, 1987; Jarchow et al., 1993; Lister et al., 1986; Mareschal and Bergantz, 1990) and magmatic arcs (Bohlen, 1987; Hamilton, 1981; Hamilton, 1988; Hildreth and Moorbath, 1988; Kay and Kay, 1981) magmatic accretion has been invoked to provide the heat and mass necessary for sustained magmatism.

However, as few exposed sections of lower continental crust are continuous between mafic intrusion and regional granulite terrain, estimates of the extent of anatexis and metamorphism accompanying magmatic accretion have relied on numerical and analog simulations. These models yield disparate results depending on

whether heat transfer within the mafic intrusion and surrounding country rocks is primarily convective (Campbell and Turner, 1987; Huppert and Sparks, 1988) or conductive (Barboza and Bergantz, 1996; Barboza and Bergantz, 1998; Bergantz and Dawes, 1994; Marsh, 1989). Therefore, a comparison with field evidence is required to discriminate between the model results. Of the few exposed lower crustal sections, the Ivrea zone (northern Italy, Southern Alps) commonly is considered to be the preeminent example of regional granulite-facies metamorphism and crustal anatexis caused by magmatic accretion. In the Ivrea zone, the exposed section of mafic plutonic rocks (the Mafic Complex) has been interpreted to represent deformed cumulates of the accreted magmas which caused regional granulite-facies metamorphism (Pin, 1990; Rivalenti et al., 1980; Rivalenti et al., 1975; Schmid and Wood, 1976; Sills, 1984; Voshage et al., 1990).

However, on the basis of preliminary analysis of field and geochemical data, Barboza *et al.* (1999) provided evidence supporting an alternative model (Schmid, 1993; Zingg et al., 1990) in which regional granulite-facies metamorphism preceded emplacement of the upper parts of the Mafic Complex. In the present paper we present results from analysis of supracrustal rocks proximal to the Mafic Complex: whole-rock major- and trace-element compositional data; inferred sequence of metamorphic reactions; and *PT* estimates derived from thermobarometry. These results demonstrate that emplacement of a major part of the Mafic Complex occurred during 1-3 kbar of decompression from ambient pressures at the thermal maximum during the regional granulite-facies episode.

We propose that, rather than providing the heat for regional metamorphism, final emplacement of the Mafic Complex caused anatexis and metamorphism only within a narrow (ca. 2 km) aureole in proximal supracrustal rocks. Amphibolite-facies metapelite overlying the Mafic Complex re-equilibrated under granulite-facies conditions at 2.5-4.5 kbar and was depleted by 20-30% of granite component. The residue of this anatexis is likely represented by leucotonalite leucosomes within the zone of contact metamorphism. If the anatexis we attribute to emplacement of the Mafic Complex is representative of magmatic accretion, intrusion of large amounts of basaltic magma within the lower crust may not inexorably result in regional metamorphism and extensive anatexis of crustal rocks. Studies that postulate such a relationship (Campbell and Turner, 1987; Huppert and Sparks, 1988; Wells, 1980) may overestimate the extent of metamorphism and anatexis caused by magmatic accretion.

GEOLOGIC SETTING

REGIONAL FRAMEWORK

The Ivrea zone is one of three tectonically bounded sections of Paleozoic basement exposed in the Southern Alps. From the originally deepest to shallowest crustal levels, the Paleozoic Southern Alpine crust comprises the Ivrea, Strona-Ceneri (or Serie dei Laghi in the Italian literature), and Val Colla zones. To the

north and west, the Ivrea zone (Figure 5.1) is separated from rocks of the Penninic belt by the Insubric line, a major, northwest-dipping, Neogene shear zone that juxtaposes pre-Alpine and Alpine structures and rock units (Gansser, 1968; Schmid et al., 1987). To the south and east, the Cremosina, Cossato-Mergazzo-Brissago (CMB) and the Pogallo Lines separate the Ivrea zone from plutonic rocks and amphibolite-facies orthogneiss and paragneiss of the Strona-Ceneri zone (Boriani et al., 1990a; Boriani and Sacchi, 1973; Handy, 1987).

Most regional studies have interpreted the Ivrea zone as a cross-section through attenuated lower continental crust (Burke and Fountain, 1990; Fountain, 1976). This interpretation is motivated by gravity and seismic studies that indicate that the Ivrea zone is the surface expression of a large, high-density body (the Ivrea geophysical body) situated where the fossilized (pre-Alpine) Southern Alpine Moho comes closest to the surface (Giese et al., 1982; Mueller et al., 1980). Geophysical modeling suggests that the Ivrea body may comprise a NNE-SSW striking, SE dipping sliver of Southern Alpine crust and mantle juxtaposed against Austroalpine and Penninic crustal rocks to the north and west (Berckhemer, 1968; Giese et al., 1982; Hirn et al., 1989). This geophysical model is consistent with structural data indicating steep tilting of the section during emplacement in the Tertiary during Alpine collision and closure of the Tethys (Nicolas et al., 1990; Schmid et al., 1987). According to this model, mafic plutonic rocks exposed along the Insubric Line (the Mafic Complex) represent the originally deepest levels of exposed crust, and the shallowest levels are represented by supracrustal rocks (the Kinzigite Formation) juxtaposed with the

Strona-Ceneri zone (Figure 5.1). Although alternative interpretations have been proposed (Boriani et al., 1990b), steep tilting of the Ivrea zone is supported by the regional increase in metamorphic grade to the northwest (Mehnert, 1975; Schmid, 1967; Zingg, 1980) and the regional barometric gradient estimated from geothermobarometry (Demarchi et al., 1998; Henk et al., 1997; Sills, 1984).

LITHOLOGIES

MAFIC COMPLEX

The Mafic Complex, traditionally interpreted to be the heat source for regional metamorphism at the Ivrea zone, consists of mafic plutonic rocks and mantle peridotite forming a belt that spans the length of the Ivrea zone along the western and northwestern margin. We focus our study on the southern Ivrea zone (Figure 5.1) where the Mafic Complex reaches its maximum exposed thickness of 10 km and comprises leuco-dioritic to gabbroic rocks intercalated with ultramafic rocks and layers of banded granulite (Quick et al., 1994; Sinigoi et al., 1995). South of the Val Sesia region, lensoidal bodies of tonalite to granodiorite diatexite ≤ 200 m thick containing blocks and schlieren of metabasite and metapelite separate the Mafic Complex from the Kinzigite Formation (Bürgi and Klötzli, 1990; Quick et al., 1994). Phase relations and *PT* estimates indicate that emplacement of the Mafic Complex occurred at crustal depths between 4-5 kbar and 8-10 kbar (Demarchi et al., 1998).

Based on field relationships (Quick et al., 1994), Sinigoi *et al.* (1996) have revised the former stratigraphic subdivisions (Rivalenti et al., 1984) of the Mafic Complex south of the Val Sesia region. The revised stratigraphy divides the Mafic Complex into the (1) Lower Mafic Complex, (2) Paragneiss – bearing belt, and (3) Upper Mafic Complex (Figure 5.1). The Paragneiss – bearing belt comprises the former “Basal” and “Intermediate” zones and separates the Upper from the Lower Mafic Complex. The Paragneiss-bearing belt and Lower Mafic Complex may represent an earlier phase of magmatism as they may have been derived from a compositionally distinct parent magma (Pin and Sills, 1986) and have undergone a different deformational history than the Upper Mafic Complex (Rivalenti et al., 1975; Zingg et al., 1990). Therefore, as the field relationships between the Lower Mafic Complex, Paragneiss – bearing belt, and the overlying supracrustal sections are obscured by the (possibly) younger intrusion, we confine our conclusions to the timing of regional granulite-facies metamorphism and emplacement of the Upper Mafic Complex.

KINZIGITE FORMATION

The Kinzigite Formation comprises amphibolite-to-granulite facies metapelite and metapsammite, with subordinate metacarbonate and metabasite. Metabasite south of the Val Sesia region (Figure 5.1) occur as 25 cm to 50 m thick, foliation parallel, lenses or layers intercalated with metapelite and minor

metacarbonate. In Val d'Ossola and Val Strona di Omegna, metabasite is more common and thick layers of metabasite and metapelite alternate (Schmid, 1967; Sills and Tarney, 1984; Zingg, 1980). In the amphibolite-facies, nematoblastic metabasite contains the assemblage amphibole + plagioclase \pm clinopyroxene. Orthopyroxene appears in granoblastic amphibole- and plagioclase-bearing metabasite with the transition to the granulite facies. Metacarbonate occurs in lenses and bands \leq 40m thick, which contain a variety of mineral assemblages (Schmid, 1967; Zingg, 1980).

The most common lithology of supracrustal rock is high-Al migmatitic metapelite with sillimanite as the stable aluminosilicate polymorph. New whole-rock, major and trace element compositions of representative metapelite and their adjacent leucosomes analyzed by XRF are listed in Tables 5.1 and 5.2. In lower Val Strona di Omegna, metapelite commonly contains biotite + quartz + plagioclase \pm garnet \pm sillimanite \pm muscovite \pm K-feldspar. Primary muscovite is restricted to the lowest grade rocks in lower Val Strona di Omegna and Val d'Ossola. Toward the northwest in upper Val Strona di Omegna, the modal proportion of garnet and K-feldspar increase at the expense of biotite and muscovite (Schmid, 1978/1979; Schmid and Wood, 1976). Cordierite and hercynitic spinel are restricted primarily to the region south of Val Sesia in metapelite proximal to the contact with the Upper Mafic Complex. We observed orthopyroxene in one Mg-rich and Al-poor metapelite. Accessory minerals include rutile, ilmenite, zircon, graphite, apatite, monazite, pyrite, chalcopyrite, and corundum.

GEOCHRONOLOGY

Geochronologic studies indicate an Early Permian-to-Carboniferous crystallization age for the Upper Mafic Complex. Pin (1986) reported zircon U-Pb data on 6 fractions of a diorite sample from the Upper Mafic Complex nearly concordant with an upper intercept of $285 \pm 7/-5$ Ma, interpreted as the age of a magmatic event during emplacement (Schmid, 1993). Sm-Nd mineral isochrons (Voshage *et al.*, 1990) from mafic and ultramafic dykes in the Paragneiss-bearing belt of ~270 Ma probably represent cooling ages following final emplacement of the Upper Mafic Complex. These Early Permian-to-Carboniferous ages for emplacement are supported by a 274 ± 17 Ma whole-rock Rb-Sr age on the tonalite to granodiorite diatexite conformable with the contact between the Upper Mafic Complex and the Kinzigite Formation (Bürigi and Klötzli, 1990).

Most geochronological evidence is consistent with the imposition of the regional metamorphic zonation during the Carboniferous (c.f. Hunziker and Zingg, 1980). U-Pb ages on monazite (Teufel and Schärer, 1989) and the inferred age of lead loss of 99-85% from discordant zircon populations (Köppel, 1974; Köppel and Grünfelder, 1971) are $274-272 \pm 2$ to 275 ± 5 Ma and 300-285 Ma, respectively. These ages likely reflect cooling below 600 °C (monazite) and close-to-thermal peak conditions (zircon). Henk *et al.* (1997) and Vavra and Schaltegger (1999), who reported decreasing monazite ages from 292 ± 2 Ma near the Pogallo Line to 276 ± 2 Ma near the Insubric Line, support an Carboniferous age for the regional thermal peak of metamorphism. These ages are also consistent with Vavra *et al.* (1996, 1999), who

suggested regional granulite-facies metamorphism occurred in a single event at 299 ± 5 Ma, based on an ion microprobe study of zircons from the Mafic Complex and Val Strona di Omegna. Thus, most geochronologic evidence supports an Early Permian-to-Carboniferous age for both magmatism within the Mafic Complex (270 Ma - 285 Ma) and regional granulite-facies metamorphism (299 ± 5 Ma).

METAMORPHISM

Although Zingg *et al.* (1990), Schmid (1993), and Barboza *et al.* (1999) take an alternative view, most regional studies have presumed or inferred a causal relationship between final emplacement of the Upper Mafic Complex and regional granulite-facies metamorphism (Bürgi and Klötzli, 1990; Hunziker and Zingg, 1980; Schmid and Wood, 1976; Schnetger, 1994; Sills, 1984; Sinigoi *et al.*, 1996). The latter interpretation is based primarily on two observations. First, Schmid and Wood (1976) reported a gradient in peak temperatures across the southeastern margin of the Upper Mafic Complex based on the reaction $\text{biotite} + \text{sillimanite} \Rightarrow \text{garnet} + \text{K-feldspar} + \text{H}_2\text{O}$, assuming $a(\text{H}_2\text{O})$ was just sufficient to cause melting. Second, the Upper Mafic Complex exhibits a textural gradation from hypidiomorphic-granular magmatic fabrics near the stratigraphically highest levels of exposure, to granoblastic textures towards the base of the Upper Mafic Complex in the northwest (Rivalenti *et al.*, 1980; Quick *et al.*, 1994). Rivalenti *et al.* (1980) and Pin (1990) suggested that

this textural gradation is consistent with cooling subsequent to synmetamorphic intrusion.

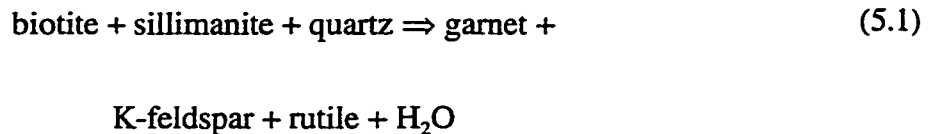
However, some *PT* estimates (Sills, 1984) do not indicate a regional scale temperature gradient with proximity to the Upper Mafic Complex. Alternative interpretations for the origin of the textural gradation within the Mafic Complex (Zingg et al., 1990; Quick et al., 1994) obviate the need for a causal relationship between magmatism and regional metamorphism. Other observations directly indicate that emplacement of the Upper Mafic Complex occurred late relative to the regional granulite-facies episode (Barboza et al., 1999). These observations include: prograde metamorphic isograds cut by the northeastern margin of the Mafic Complex (Zingg et al., 1990); metapelite proximal to the Mafic Complex overprinted with a low-pressure assemblage (Barboza et al., 1999; Schmid, 1993); and no apparent increase in element depletion of granulite with proximity to the Mafic Complex (Barboza et al., 1999).

To provide additional constraints on the relationship between emplacement of the Upper Mafic Complex and regional metamorphic *PTt* history of the Ivrea zone, we collected samples for petrographic study and geochemical analysis on traverses through the Kinzigite Formation. The longest sections of continuous exposure south of the Val Sesia region crossing the contact between the Kinzigite Formation and the Upper Mafic Complex were along Rio Forcioula in Val Strona di Postua and Fiume Duggia in Val Duggia (Figure 5.2). We compared samples collected along these traverses with more distal samples collected in Val Strona di Omezna and Val d'Ossola (Figure 5.1). The general regional pattern of metamorphic zonation reflects an increase in grade from the amphibolite- to the granulite-facies both toward the northwest and the southwest, approximately perpendicular and parallel to the regional fabric, respectively.

BETWEEN UPPER AND LOWER VAL STRONA DI OMEGNA AND VAL D'OSSOLA

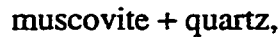
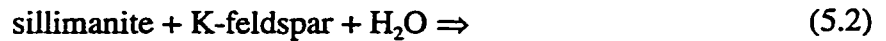
The increase in metamorphic grade to the northwest with increasing original crustal depth has been previously described, and characterizes the regional amphibolite- to granulite-facies metamorphism in the Ivrea zone. A textural change in metapelite from lepidoblastic to granoblastic attends the replacement of muscovite and biotite by K-feldspar and garnet, with increasing grade (Hunziker and Zingg, 1980; Schmid, 1967; Schmid and Wood, 1976). Compositions of amphibolite-facies metapelite in lower Val Strona di Omezna lie within the three-phase field defined by biotite-garnet-sillimanite on an AFM projection from muscovite (Figure 5.3). In the

granulite facies rocks of upper Val Strona di Omegna and Val d'Ossola, quartz + hypersthene ± garnet granulite and metacalc-silicate are interlayered with granoblastic graphite + sillimanite + garnet gneiss, interpreted to be residual material from the melting of metapelite (Schmid, 1978/1979; Schmid and Wood, 1976; Schnetger, 1994). Schmid and Wood (1976) attributed the increase in modal garnet at the expense of biotite to the continuous reaction:



Based on a compilation of previous petrographic work, Zingg (1980) located mineral isograds that represent prograde reactions produced during the high-grade, regional metamorphic episode (Figure 5.1). These isograds include the muscovite - K-feldspar isograd in sillimanite-bearing metapelite, the first appearance of coexisting pyroxenes in metabasite, and the upper stability of calcite-quartz-actinolite in calc-silicate.

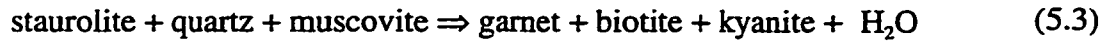
Two phases of muscovite growth are apparent southeast of the muscovite-out isograd (Figure 5.1) in lower Val Strona di Omegna and Val d'Ossola. Muscovite₂ is distinguished from muscovite₁ in that its foliation is oblique to that defined by muscovite₁, biotite, and sillimanite (Figure 5.4A). This relationship suggests that muscovite₂ may have appeared during retrograde cooling and hydration through the reaction:



an inference supported by common textures indicating the direct replacement of sillimanite + K-feldspar by symplectitic intergrowths of muscovite₂ + quartz.

BETWEEN LOWER VAL SESIA AND VAL STRONA DI POSTUA

Metamorphic grade increases from the amphibolite facies in lower Val Strona di Omega, parallel to the regional fabric SSW toward the Val Sesia region. In Kinzigite Formation south of Val Sesia, orthopyroxene commonly coexists with plagioclase in amphibole-bearing metabasites, indicating final equilibration of these rocks in the granulite facies. Figure 5.3 depicts AFM projections of metapelite illustrating the change from the garnet-biotite-sillimanite three-phase field in Val Strona di Omega to the garnet-cordierite-sillimanite three-phase field south of Val Sesia. Fibrolite is the dominant textural variety of sillimanite, but with increasing grade, coarse-grained prismatic sillimanite is common. Zingg (1980) reported the occasional presence of relict staurolite enclosed by cordierite. Relict kyanite has also been reported in a number of localities south of the Val Sesia region (Bertolani, 1959; Boriani and Sacchi, 1973; Capedri, 1971; Demarchi et al., 1998). The reactions:

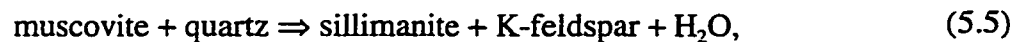


and

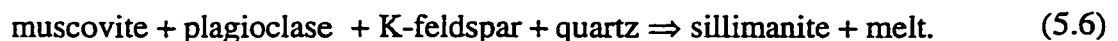


probably document the prograde transition from the kyanite + staurolite to the sillimanite stability field during a high-pressure phase of prograde metamorphism.

The muscovite-out isograd in metapelite lies to the northeast of the region south of Val Sesia (Figure 5.1), so metapelite overlying the Upper Mafic Complex commonly contains sillimanite + K-feldspar, but lacks primary muscovite (Zingg, 1980). This assemblage implies the reaction:



or an H₂O-conserved melting reaction such as



At pressures below 6 kbar, either reaction 5.5 or 5.6 signifies temperatures proximal to the Mafic Complex exceeded ~600 °C (Vielzeuf and Holloway, 1988).

In lower Val Strona di Omegna, biotite is the major mineral phase in metapelite. However, biotite is irregularly distributed in metapelite overlying the Mafic Complex south of Val Sesia, with some samples containing <5% modal biotite. The decrease in the proportion of modal biotite to the southwest is coincident with the appearance of cordierite in an approximately 2 - 3 km aureole overlying the Upper Mafic Complex (Figure 5.1). Cordierite is often heavily pinnitized, but, when preserved, at least two generations are apparent (Capedri and Rivalenti, 1973). Cordierite₁, present in minor amounts, encloses fibrolite and is elongate parallel to the foliation defined by biotite and the long axis of the garnet augen. This observation implies that cordierite₁ growth followed reaction 5.3 or 5.4. We infer that cordierite₁ may have formed from the continuous reaction:



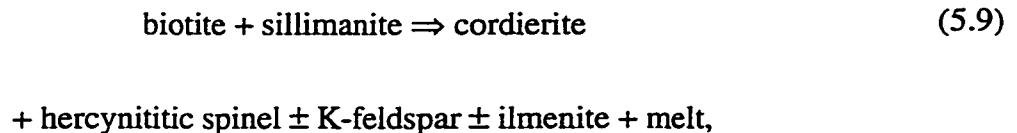
Cordierite₂, the more abundant phase, occur as up to 5 mm prisms which often cut the foliation defined by biotite and sillimanite (Capedri and Rivalenti, 1973). Idiomorphic cordierite is often present also in leucotonalite leucosomes within migmatitic metapelite. These K-poor leucosomes are restricted to the 2-km aureole surrounding the Upper Mafic Complex coincident with the appearance of cordierite and hercynitic spinel in the melanosome assemblage. We interpret these relationships to indicate that cordierite₂ was a peritectic phase produced during the melting reaction

from which the leucotonalite leucosomes were derived. These observations imply the reaction:



This inference is supported by the common occurrence of cordierite₂ with K-feldspar porphyroblasts in the tonalite to granodiorite diatexite (Bürgi and Klötzli, 1990; Quick et al., 1994), which separates the Upper Mafic Complex from the overlying Kinzigite Formation south of the Val Sesia region.

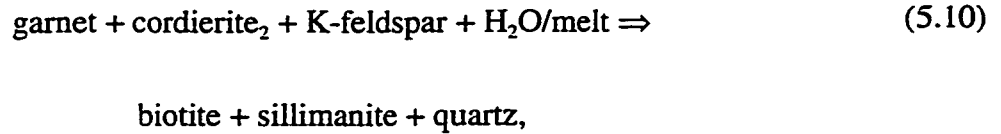
Hercynitic spinel with sillimanite corona is occasionally present and is always enclosed within cordierite₂ cores (Figure 5.4B). This observation is consistent with the reaction:



in locally quartz deficient domains.

Retrograde replacement of the assemblage cordierite + K-feldspar is indicated by the development of symplectitic intergrowths of biotite + sillimanite + quartz (Figures 5.4C and 5.4D). This observation implies retrograde hydration via

reaction with a vapor phase or back-reaction with residual melt through the equilibrium:



along the retrograde path.

Although andalusite was not observed in this study, it has been reported between lower Val Sesia and Val Sessera (Capedri and Rivalenti, 1973; Demarchi et al., 1998; Zingg, 1980). The abundance of andalusite increases to the southwest and is reported to occur commonly near Biella in Valle Mosso (Bertolani, 1959; Sacchi, 1962). Although Zingg (1980) interpreted andalusite as a relict phase, Capedri and Rivalenti (1973), based on microstructural relationships, infer andalusite growth after sillimanite. According to this view, the rare andalusite occurrences document the retrograde transition from the sillimanite to the andalusite stability field:



THERMOBAROMETRY

The widespread occurrence of metapelite in the Kinzigite Formation south of the Val Sesia region provides favorable assemblages for thermobarometry, providing

additional constraints on the regional *PTt* paths. Calculations were conducted with MacPTAX (J. Lieberman, 1991, unpublished) using a 1991 update of Berman's thermodynamic database (Berman, 1988). Pressure and temperature estimates were obtained with the GASP ($3\text{An} \Rightarrow \text{Grs} + 2\text{Als} + \text{Qtz}$) reaction and Fe-Mg exchange between garnet and biotite. We adopted the activity models of Berman (1990) for garnet, McMullin (McMullin et al., 1991) for biotite, and Fuhrman and Lindsley (1988) for plagioclase. Mineral compositions and garnet and plagioclase zoning patterns were obtained by x-ray mapping and electron microprobe analyses. In accordance with Guidotti and Dyars' (1991) empirical model, we assumed that ferric iron accounted for 8% of FeO^{T} in biotite. We assumed $\text{FeO}^{\text{T}} = \text{FeO}$ in garnet. Sample locations are provided on Figure 5.2 and representative mineral analyses are listed in Tables 5.3, 5.4, and 5.5.

PT conditions were estimated for nine samples collected on traverses along the Rio Forcioula (6) and Fiume Duggia (3) (Figure 5.2). To estimate "peak" conditions, we compared garnet core compositions free of local zoning near inclusions (determined by X-ray mapping and microprobe analyses) with plagioclase cores and neighboring matrix biotite not in contact with garnet. South of the Val Sesia region, the texture of the predominant garnet phase is medium/coarse grained elongate augen, with a long axis parallel to the foliation defined by sillimanite and biotite. At least three phases of garnet growth are evident. Garnet augen possess inclusion-rich cores surrounded by inclusion-free rims, and late, fine-grained, inclusion-free, idiomorphic garnets cut the foliation defined by biotite, sillimanite, and the long axis of the garnet

augen. Unlike garnets from lower Val Strona di Omegna and Val d'Ossola which exhibit compositional zoning in grossular and, to a lesser extent, spessartine components in the interior and the outermost ~5-10 μ , garnet south of the Val Sesia region is virtually unzoned (Figure 5.5). The absence of interior growth zoning probably indicates homogenization of the garnets at temperatures exceeding 600-650 °C (Whitney and Dilek, 1998).

Figure 5.6 depicts the results of our thermobarometric calculations for metapelite overlying the Upper Mafic Complex and reported *PT* estimates on rocks at a similar structural level in lower Val Strona di Omegna (Henk et al., 1997). Estimated “peak” *PT* conditions deviate from conditions indicated by the modal mineralogy in that one sample, which contains sillimanite, overlaps the stability field of andalusite. Therefore, “peak” calculated temperatures probably do not correspond to the maximum temperatures attained due to retrograde Fe-Mg exchange and because exchange and net transfer equilibria tend to have different closure temperatures (Frost and Chacko, 1989). Therefore, our calculation of “peak” conditions should be regarded as a minimum estimate of the *PT* conditions during the local thermal maximum.

PRESSURE-TEMPERATURE HISTORY

PETROGENETIC GRID

We inferred the regional *PTt* path using the sequence of metamorphic reactions deduced from our microstructural interpretation of reaction histories with additional constraints provided by *PT* estimates derived from geothermobarometry. The petrogenetic grid we used for our analysis (Figure 5.7A) includes the beginning of melting in the system Qz–Ab–An–Or–H₂O (Johannes, 1984) and relevant subsolidus and melting reactions for intermediate X_{Mg} pelites (Vielzeuf and Holloway, 1988) in the system KFMASH. The bulk composition of typical metapelite in the Ivrea zone approximates the intermediate X_{Mg} metapelite for which the grid applies (Figure 5.3). For clarity, single lines represent the divariant fields for the equilibria in Figure 5.7 (Vielzeuf and Holloway, 1988). The omission of Fe₂O₃, TiO₂, Na₂O, and CaO from the KFMASH model system precludes the consideration of reactions involving Fe-Ti oxides and plagioclase. Inclusion of an albitic component shifts melting curves to lower temperatures by ~40 °C (Vielzeuf and Holloway, 1988), whereas an anorthitic component reduces this effect (Carrington and Harley, 1995; Thompson and Tracy, 1979).

SUMMARY OF INFERRED *PTt* PATH

Two *PTt* paths are illustrated in Figure 5.7B. The thick shaded line illustrates our inferred *PTt* path "A" for rocks proximal to the Upper Mafic Complex

south of the Val Sesia region. The thinner shaded line labeled path "B" depicts the *PTt* path for rocks distal to the Upper Mafic Complex in Val Strona di Omega. Both paths were inferred for rocks at the approximate structural level of the contact between the Upper Mafic Complex and the Kinzigite Formation south of the Val Sesia region. Arrows indicate constraints on the *PTt* path for which we interpret microstructural evidence that the indicated reaction boundaries were crossed during metamorphism. *PT* and age constraints obtained from geothermobarometry (Figure 5.6) and geochronology are indicated at their respective portions of the *PTt* path.

One interpretation of the presence of relict kyanite and staurolite is that these phases document staurolite growth and the prograde transition from the kyanite to the sillimanite stability field due to thickening during prograde metamorphism. Although not the only interpretation of the prograde metamorphic evolution of the Ivrea zone (Zingg, 1983; Handy and Zingg, 1991), this interpretation is consistent with evidence of high-pressure metamorphism elsewhere in the Paleozoic basement of the Alps documenting the collisional phase of the Variscan orogeny (e.g. Vielzeuf and Pin, 1989). The trajectory and maximum pressure attained along the prograde path, however, are unconstrained (Figure 5.7B). Henk *et al.* (1997) inferred *PT* conditions at the thermal peak of metamorphism for rocks in lower Val Strona di Omega between 4 kbar/650 °C and 6 kbar/700 °C (marked "T" in Figure 5.7B).

Subsequent to the regional thermal maximum, path "A" and path "B" diverge. The absence of cordierite and the presence of retrograde muscovite₂ through reaction 5.2 in metapelite from lower Val Strona di Omega requires that cooling accompany

decompression from the regional barometric gradient at the thermal maximum. However, high-grade conditions (exceeding 650 °C) in supracrustal rocks proximal to the Upper Mafic Complex were maintained during decompression, an inference consistent with *PT* estimates derived from geothermobarometry (Figure 5.6). High-grade conditions proximal to the Upper Mafic Complex are also consistent with the occurrence of sillimanite as a common inclusion phase within garnet, an observation indicating a significant portion of the prograde path for proximal rocks (path "A") occurred within the stability field of sillimanite. Additionally, the occurrence of peritectic cordierite₂ via reaction 5.8 requires temperatures exceeding 650-700 °C. Upon decompression at lower temperatures, the breakdown of biotite produces cordierite in the presence of a vapor phase rather than a melt (Figure 5.7A). Finally, temperatures exceeding 600 - 650 °C proximal to the Upper Mafic Complex are consistent with the absence of zoning patterns in garnet (Figure 5.5).

The predominant microstructural feature of retrograde metamorphism preserved in metapelite proximal to the Upper Mafic Complex is replacement of cordierite and K-feldspar by symplectitic intergrowths of biotite + sillimanite + quartz (Reaction 5.10). The dP/dT slope (Figure 5.7A) of this equilibrium is shallow (Vielzeuf and Holloway, 1988), indicating the region followed a near isobaric cooling path following regional retrograde decompression and magmatism (Figure 5.7B). Andalusite (Reaction 5.11) probably documents the retrograde transition from the sillimanite to the andalusite stability field.

ANATEXIS

The preceding *PTt* analysis implies decompression melting of metapelite was restricted to proximal rocks overlying the Upper Mafic Complex containing cordierite₂, which we interpret formed as a peritectic phase. To test this inference, we conducted mass balance calculations from which we estimated the extent of depletion of metapelite proximal to the Upper Mafic Complex relative to metapelite at a similar structural level in Val Strona di Omegna and Val d'Ossola. We adopted the isocon method of mass balance, originally developed by Grant (1986) on the basis of Gresens' (1967) equations, as assumptions of constant mass or volume are not required. Olsen and Grant (1991) have demonstrated application of the isocon method for metasomatic alteration and anatexis in migmatites and discussed the various sources of uncertainty.

Our analysis incorporates a revised logarithmic formulation of the isocon equations in which several of the variables are recast. A complete derivation of the equations is provided in the Appendix. The final form of the equation used for the analysis is:

$$\ln(M^A) = \ln \left[\left(\frac{M^o}{M^A} \right) C_i^o + \left(\frac{M^A}{M^A} \right) C_i^A \right], \quad (5.12)$$

where M^o , M^A , and M^A are the original rock mass, altered rock mass, and mass of material removed, respectively. C_i^A , C_i^o , and C_i^A are the concentrations of component i in the altered rock, the original rock, and in the altering fluid, respectively.

According to this formulation, conserved components ($C_i^A = 0$) should lie on a straight line with a slope of one (called an isocon). The intercept of the isocon (I) on the C^A axis on a log-log plot of component concentration in the original (C^0) against the altered (C^A) rock is related to the change in mass of the rock during alteration through the relationship:

$$M^A = \frac{M^0(1 - e^I)}{e^I} \quad (5.13)$$

Mobile components extracted from or added to the rock during alteration should lie below or above the isocon, respectively. As this formulation is logarithmic, lines of constant depletion or enrichment will be curved and asymptotic to the isocon. To illustrate this point, our isocon diagrams (Figures 5.8 and 5.9) are contoured with curves of constant depletion and enrichment in ppm. From these relationships, the change in mass of the rock, and composition of the altering fluid may be calculated (Appendix A).

SAMPLES

We collected samples of metapelite melanosomes and adjacent leucotonalite leucosomes for whole-rock major and trace element analysis along the Rio Forcioula and Fiume Duggia (Figure 5.2). We collected and analyzed 10 samples of metapelite from lower Val d'Ossola and Val Strona di Omegna which did not exhibit a migmatitic character, from which we calculated the average composition and

degree of variability in the oxide and trace element concentrations. We used this average composition to construct a composite protolith composition for comparison with individual metapelite samples proximal to the Upper Mafic Complex. Whole rock major and trace element concentrations for metapelite melanosomes and individual samples used to construct the composite protolith are listed in Table 5.1.

RESULTS

Figure 5.8 depicts isocon diagrams comparing four representative metapelite melanosomes to the composite metapelite (C°) averaged from samples collected in Val d'Ossola (Figure 5.1). The isocons for all four samples in Figure 5.8 were calculated by linear regression of compositional components that we have assumed are conserved during anatexis: TiO_2 , MgO , and FeO^T . For all samples, SiO_2 , Na_2O , CaO , K_2O , Ba , Rb , Sr , Ta , and Cs are distributed below the isocon, indicating a systematic loss of these components during contact metamorphism. The trace elements Y , Hf , La , and Zr typically were distributed along the isocon, indicating these components were relatively immobile during alteration. The smallest mass loss (-18%) is indicated by the isocons for samples 62497-01 and 70197-05. Isocons for samples 80496-20 and 70197-3 indicate a net loss of 33% and 26% mass respectively. Other samples not plotted exhibited similar levels of mass loss. Depletion in K_2O typically exceeded that of Na_2O and total alkali depletion exceeded that of CaO . Our predicted composition of melt removed from the melanosome is high in SiO_2 and contains 1000 – 1500 ppm Ba and 220 – 300 ppm Rb . These relationships suggest

that a granitic melt enriched in orthoclase component over albite was extracted from the melanosomes.

Leucotonalite leucosomes immediately adjacent to the melanosomes do not represent the extracted granitic melt: they are systematically depleted in the alkalis and most other compositional components relative to our predicted melt composition (Figure 5.9). Therefore, the leucotonalite leucosomes probably represent the granitic melt extracted from the restite, further depleted by loss of an orthoclase-enriched component, an inference consistent with their systematic depletion in LILE relative to the adjacent melanosomes (Figure 5.10). Wholesale, regional depletion in the alkalis (Barboza et al., 1999) indicates that melt extraction was efficient south of Val Sesia, perhaps promoted by progressive, non-coaxial, ductile deformation of the carapace of supracrustal rocks during emplacement of the Upper Mafic Complex (Snoke et al., 1994; Snoke et al., 1999).

DISCUSSION AND CONCLUSIONS

TECTONIC IMPLICATIONS

Figure 5.11 depicts a schematic illustration of our model for metamorphism and magmatic accretion at the Ivrea zone. Reported occurrences of relict kyanite and staurolite (Bertolani, 1959; Boriani and Sacchi, 1973; Zingg, 1980) probably document prograde metamorphism in the kyanite + staurolite stability field. One possible interpretation of these relict phases is that prograde metamorphism along

the prograde *PTr* path accompanied thickening in a compressional tectonic environment (Figure 5.11A). According to this view, thickening during the early prograde metamorphic evolution of the Ivrea zone preceded the regional thermal maximum of 299 ± 5 , so was perhaps coincident with regional compression during the collisional phase of the Variscan orogeny (Matte, 1986; Matte, 1991). Although the regional peak pressures prior to the thermal maximum are unconstrained, the ubiquitous presence of sillimanite regionally and as inclusions within garnet indicates prograde metamorphism within the stability field of sillimanite and likely precludes significant overthickening as the mechanism that caused the regional thermal maximum.

We infer that the regional thermal peak of metamorphism accompanied decompression along the prograde path (Figure 5.11B), yielding a barometric gradient from 4-5 kbar to 8-10 kbar across the Ivrea zone (Henk et al., 1997). This interpretation is consistent with Brodie (1995) who interpreted oriented symplectic intergrowths of orthopyroxene, plagioclase, and spinel in metapelite from upper Val Strona di Omega as indicating an episode of regional near-isothermal decompression. *PT* conditions for rocks in lower Val Strona di Omega at the regional thermal maximum are 3.5-6.0 kbar and $\sim 650-700$ °C, implying a thermal gradient of $\sim 40-60$ °C/km, if the geotherm was quasi-steady state. These *PT* conditions are elevated with respect to an average crustal geotherm and De Yoreo *et al.* (1991) suggest that such conditions require elevated heat flow through a combination of magmatic accretion, aqueous fluid flow, and/or lithospheric extension.

The appearance of cordierite, hercynitic spinel, grossular-poor garnet and anorthitic plagioclase indicates that depleted metapelite proximal to the Upper Mafic Complex underwent near-isothermal decompression subsequent to the regional thermal maximum. The absence of these phases and the presence retrograde muscovite₂ requires that significant cooling accompanied decompression in rocks distal to the Upper Mafic Complex. *PT* estimates indicate rocks from lower Val Strona di Postua equilibrated at 1-3 kbar lower pressure than rocks at a similar structural level in Val Strona di Omega (Figure 5.6). These observations indicate that emplacement of the Upper Mafic Complex occurred during retrograde decompression from the regional thermal maximum (Figure 5.11C). Although heat released during cooling provided the thermal energy to reset proximal mineral assemblages, distal rocks were incompletely reset.

We propose that crustal attenuation through tectonic extension (Figures 5.11B and 5.11C) may explain decompression from regional peak pressures attained during prograde compression. Extension, perhaps accompanied by magmatic accretion, leads to passive upwelling of the asthenosphere and a consequent steepening of the geotherm, thereby enhancing the lower crustal heat budget (De Yoreo et al., 1991; Furlong and Londe, 1986). Whitney & Dilek (1998) interpreted Miocene extension after Oligocene contraction as having produced a *PTt* path in the Nigde massif, Turkey similar to what we have inferred for the Ivrea zone. Lachnebruch & Sass (1978) inferred a geotherm exceeding 40 °C/km for the Battle Mountain High in the Basin and Range Province, suggesting enhanced heat flow

through tectonic extension could, in principle, have caused regional metamorphism at the Ivrea zone.

Crustal attenuation through tectonic extension is consistent also with other observations in the Ivrea zone. Sills (1984) inferred a barometric gradient of approximately 0.5 kbar/km in Val Sesia and Val Mastallone and Henk *et al.* (1997) inferred 0.41 kbar/km in Val Strona di Omegna. Both of these estimates exceed the lithostatic gradient of 0.3 kbar/km (Burke and Fountain, 1990), suggesting crustal attenuation by a factor of ~1.4 subsequent to the closure temperature of the net transfer reactions from which pressure was estimated in the respective studies. Regional extension is consistent with Brodie and Rutter's (1987) inference that 2km of E-W directed attenuation within the lowermost 5 km of the Ivrea zone occurred along mylonitic shear zones. Handy (1987) estimated 8-10 km of E-W directed extension along normal faulting near the boundary between the Ivrea and Strona-Ceneri zones. Additionally, Quick *et al.* (1994), interpreted the arcuate structure of relict magmatic foliation in the Upper Mafic Complex as implying emplacement into a zone of active extension, an inference consistent with age estimates for the onset of regional extension along the regional retrograde *PTt* path (Brodie *et al.*, 1989). Finally, Snoke *et al.* (1994; 1999) reported evidence supporting progressive, non-coaxial, ductile deformation within the carapace of supracrustal rocks overlying the Upper Mafic Complex, an observation consistent with ductile attenuation during emplacement. Although mineral compositional variability and the thin (~3km) section overlying the Upper Mafic Complex preclude a direct calculation of the barometric gradient in Val

Strona di Postua, significant crustal attenuation can be accommodated by our results (Figure 5.2).

We conclude that the tectonics of the Ivrea zone from the Late Carboniferous through the Early Permian was characterized by tectonic extension. The peak thermal episode of regional granulite-facies metamorphism resulted from elevated heat flow during extension and was perhaps enhanced by magmatic accretion below the current level of exposure (Henk et al., 1997). Emplacement of the Upper Mafic Complex took place late during this extensional phase and accompanied up to ~1-3 kbar of decompression from ambient pressures at the regional peak of metamorphism. The heat released during crystallization of the Upper Mafic Complex provided the thermal energy for metamorphism up to the granulite facies in proximal crustal rocks. The occurrence of cordierite, hercynitic spinel, leucotonalite leucosomes, anorthitic plagioclase, and grossular-poor garnets preserve evidence of this episode of low-pressure, high-temperature contact metamorphism. Continued crustal attenuation after the regional thermal maximum led to decompression melting of metapelite overlying the Upper Mafic Complex and their depletion by up to ~30% granite component. The cessation of extension and high-grade conditions in rocks proximal to the Upper Mafic Complex was perhaps coincident with its final emplacement (Demarchi et al., 1998) and was followed by a period of near isobaric-cooling (Figure 5.11D).

MAGMATIC ACCRETION MODELS

Our field, petrographic, and geochemical evidence imply that anatexis and metamorphism caused by emplacement of the Upper Mafic Complex was confined within a ~2 km aureole in supracrustal rocks overlying the intrusion. Models that rely upon rapid cooling and convective heat transfer during magmatic accretion (Campbell and Turner, 1987; Wells, 1980) overpredict the extent of crustal heating and anatexis we observe in the Ivrea zone. For instance, Huppert and Sparks (1988) calculated that emplacement of basaltic magma at 1200 °C into crust at 500-850 °C would generate a volume of silicic magma roughly 0.6 to 2.0 times that of the basalt. This amount exceeds the extent of anatexis we have inferred within the Upper Mafic Complex contact aureole. Even simulations based on a conductive model for heat transfer (Barboza and Bergantz, 1996) overestimate the extent of the contact aureole in less than 0.1 Ma after the initiation of magmatism.

We propose the discrepancy between the model results and the field observations may be resolved if new additions of magma were supplied to the Upper Mafic Complex episodically and at slow rate, an inference consistent with the proposed “gabbro glacier” model for emplacement of the Mafic Complex (Quick et al., 1994). In this way, heat advected into the Upper Mafic Complex by intruding magmas was balanced by conductive cooling within the overlying supracrustal rocks. In this case, the narrow contact aureole represents the thermal equilibration of crustal rocks from the heat released during magmatism at the final stages of emplacement of the Upper Mafic Complex. Therefore, the common model assumption that large

volumes of mafic magma are emplaced instantaneously relative to the rate of conductive cooling, at least in the case of the Ivrea zone, is invalid. If the Ivrea zone is representative of magmatic accretion, emplacement of large volumes of mafic magma within the lower continental crust may not inexorably imply regional-scale metamorphism and anatexis of crustal rocks. Reference to studies which predict regional granulite-facies metamorphism and extensive crustal anatexis are a consequence magmatic accretion (Campbell and Turner, 1987; Huppert and Sparks, 1988; Wells, 1980; Wickham and Oxburgh, 1987) should be tempered by an awareness that such effects are not apparent in the Ivrea zone, widely regarded as the putative example of such a process.

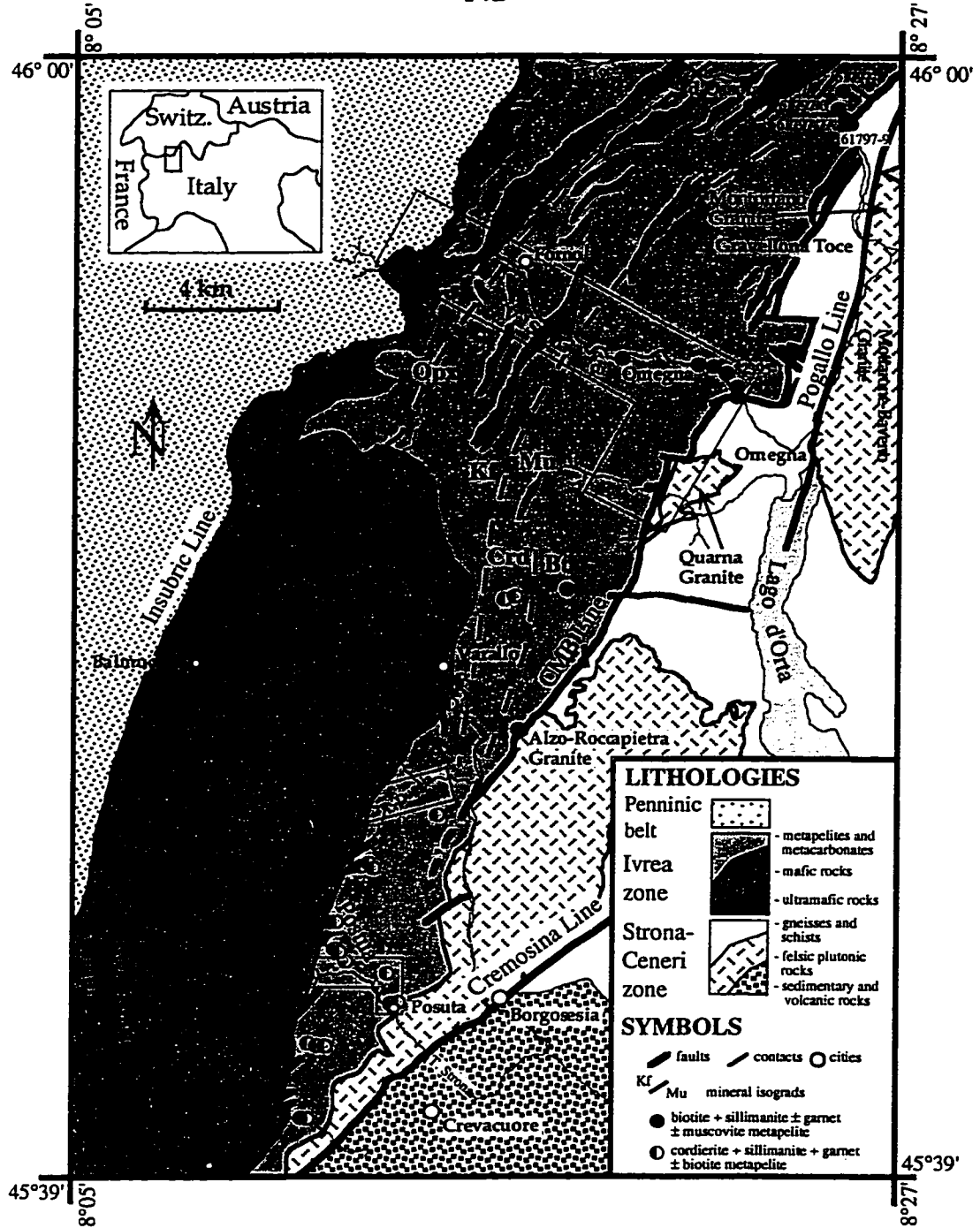


Figure 5.1. Geologic map of the southern Ivrea and Strona-Ceneri zones west of Lago d'Orta. Inset shows location of study area in northern Italy. Contact between Mafic Complex and Kinzigite Formation based on our own mapping and that of Quick et al. (1994). Stratigraphic relationships within the Mafic Complex from Sinigoi et al. (1996). Boundary between the Ivrea zone and the Strona-Ceneri zone between Val Strona di Omegna and Val d'Ossola from Boriani et al. (1990a). The muscovite - K-feldspar isograd, and the first appearance of orthopyroxene in mafic rocks indicated by the dashed lines (Schmid, 1967; Zingg, 1980).

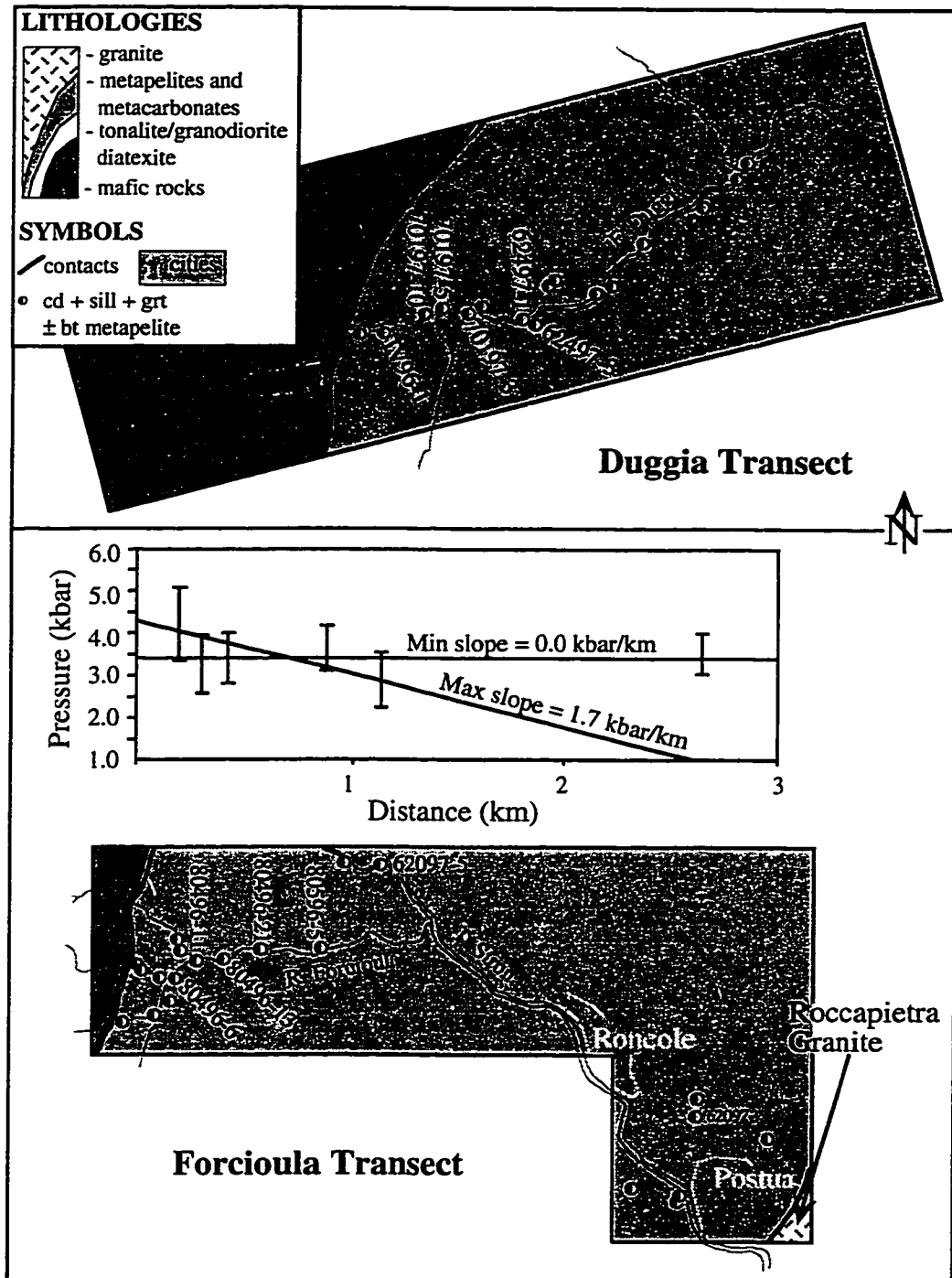


Figure 5.2. Detail sample location maps along R. Forcioula and F. Duggia. Labels indicate samples used for thermobarometry and mass balance calculations. Across-strike barometric gradient along the R. Forcioula transect with distance from the contact between the Kinzigite Formation and the Upper Mafic Complex.

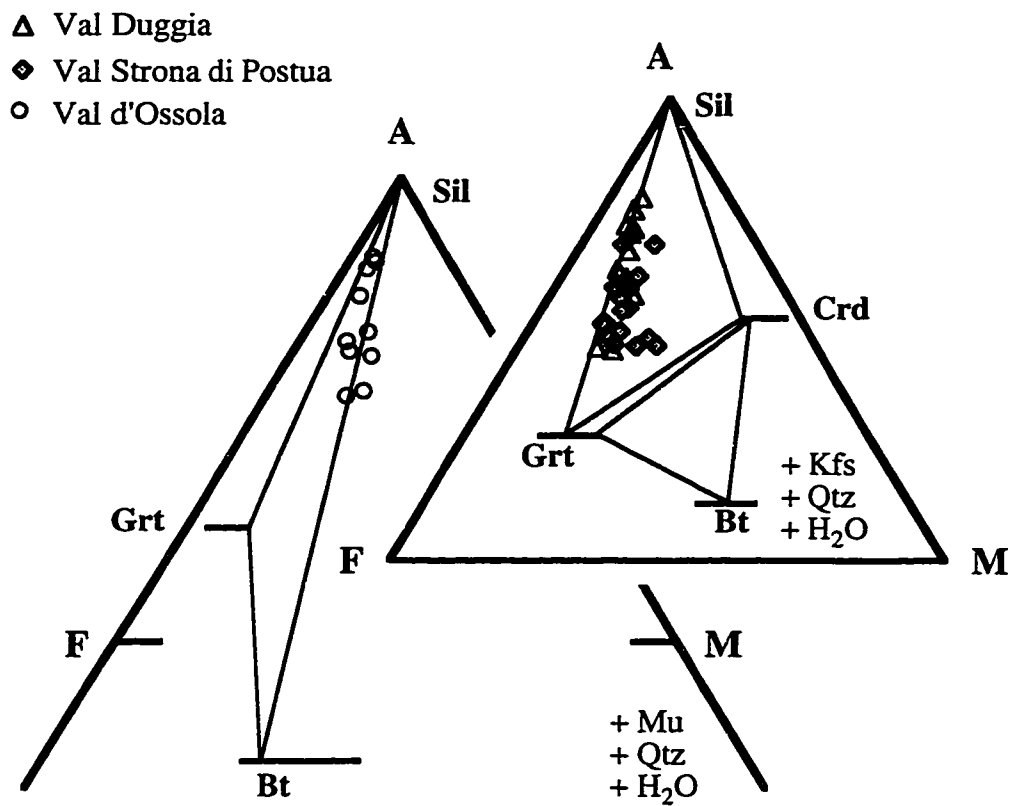


Figure 5.3. AFM projection from muscovite (Val d'Ossola samples) and K-feldspar (F. Duggia and R. Forcioula samples). Bars for minerals indicate the range of measured Fe/Mg ratios for minerals in representative samples.

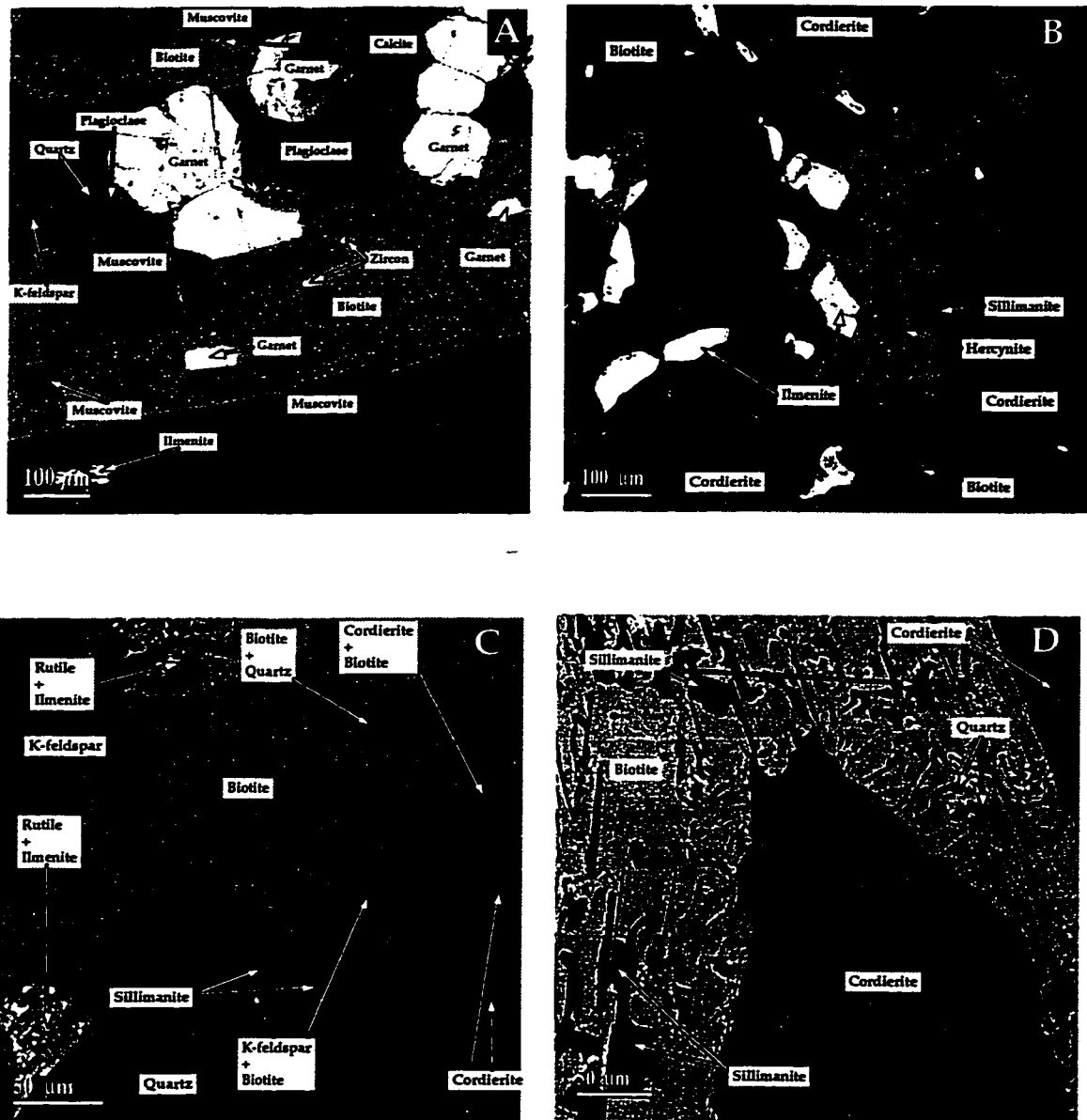


Figure 5.4. A) Retrograde muscovite₂ nearly perpendicular to the foliation defined by muscovite₁, biotite, and sillimanite; sillimanite-garnet-biotite schist 82395-1, Val Strona di Omega. B) Hercynitic spinel and ilmenite with sillimanite coronae in cordierite₂ core; sillimanite-cordierite-garnet gneiss 80596-5, Val Strona di Posuta. C) Retrograde replacement of cordierite + K-feldspar by symplectitic intergrowths of biotite + sillimanite + quartz; sillimanite-cordierite-garnet gneiss 62097-3. D) Closeup of cordierite₂ with reaction rim of radiating biotite + quartz + sillimanite symplectite; sillimanite-cordierite-garnet gneiss 62097-3.

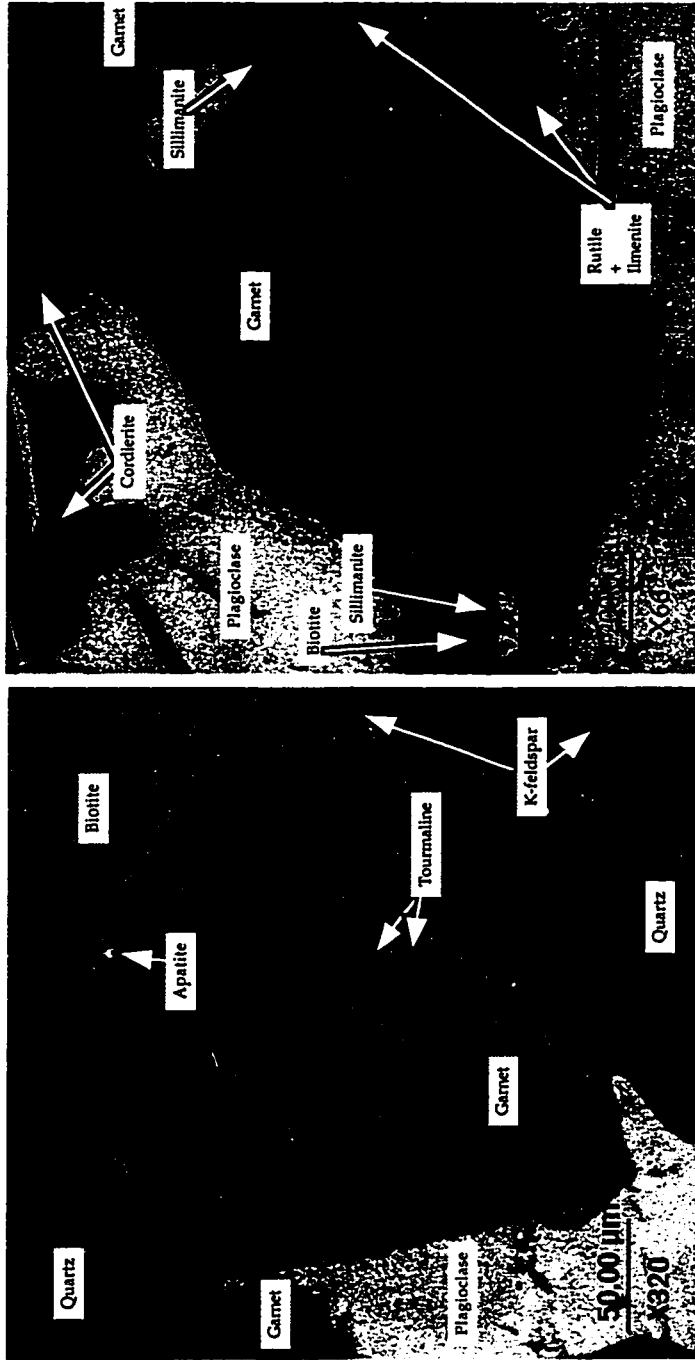


Figure 5.5. X-ray maps of grossular component in garnet. A) fine-grained, idiomorphic garnet exhibiting interior growth zoning and a strongly zoned rim where juxtaposed with biotite; sillimanite-garnet-biotite schist 82395-1, lower Val Strona di Omegna. B) unzoned, coarse-grained garnet; sillimanite-cordierite-garnet gneiss 62497-3, Val Strona di Postua.

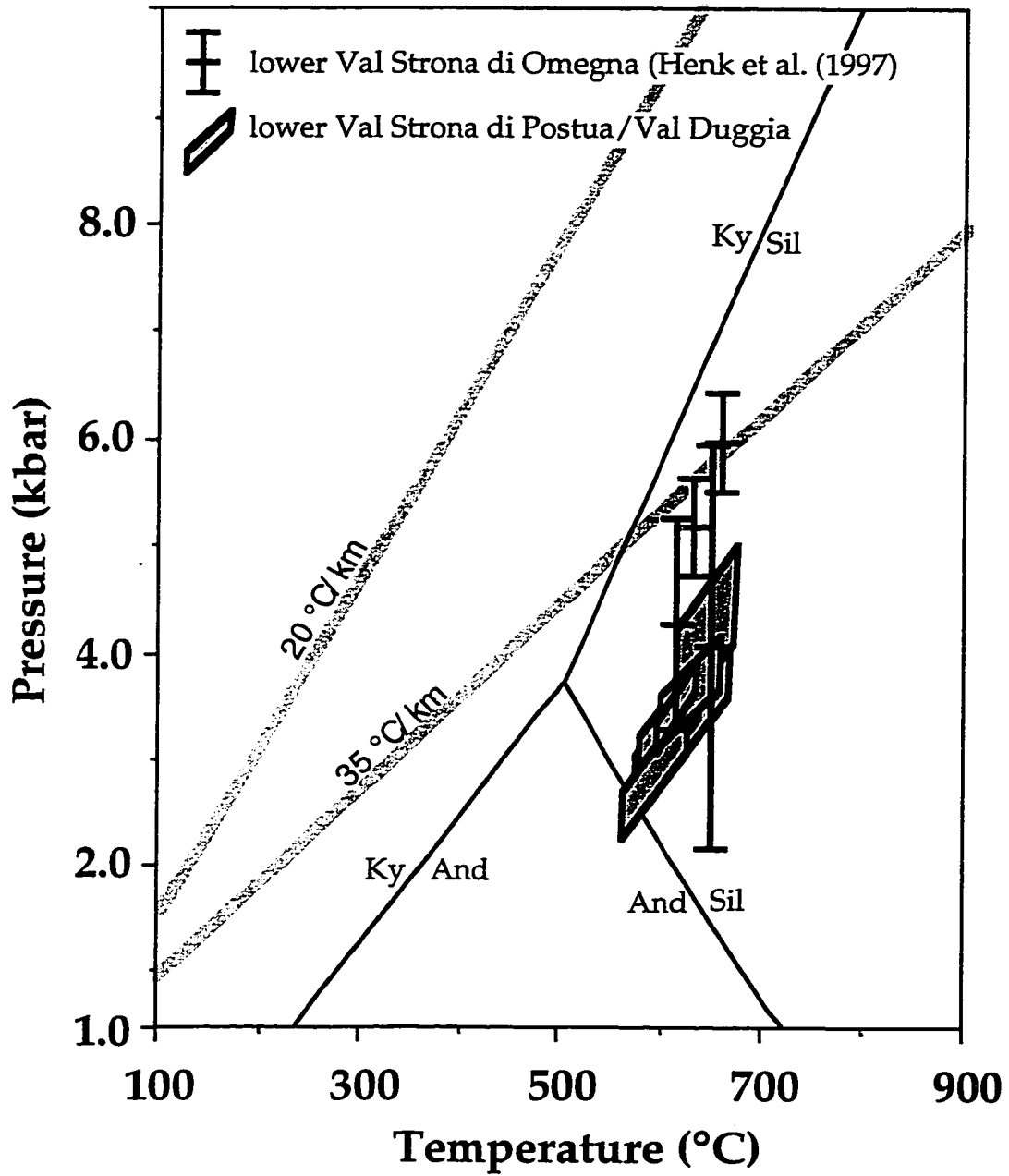


Figure 5.6. Calculated *PT* positions of thermobarometric equilibria for representative metapelite from Val Strona di Posuta and Val Duggia. Bars represent reported *PT* estimates for structurally equivalent metapelite in lower Val Strona di Omegna (Henk et al., 1997).

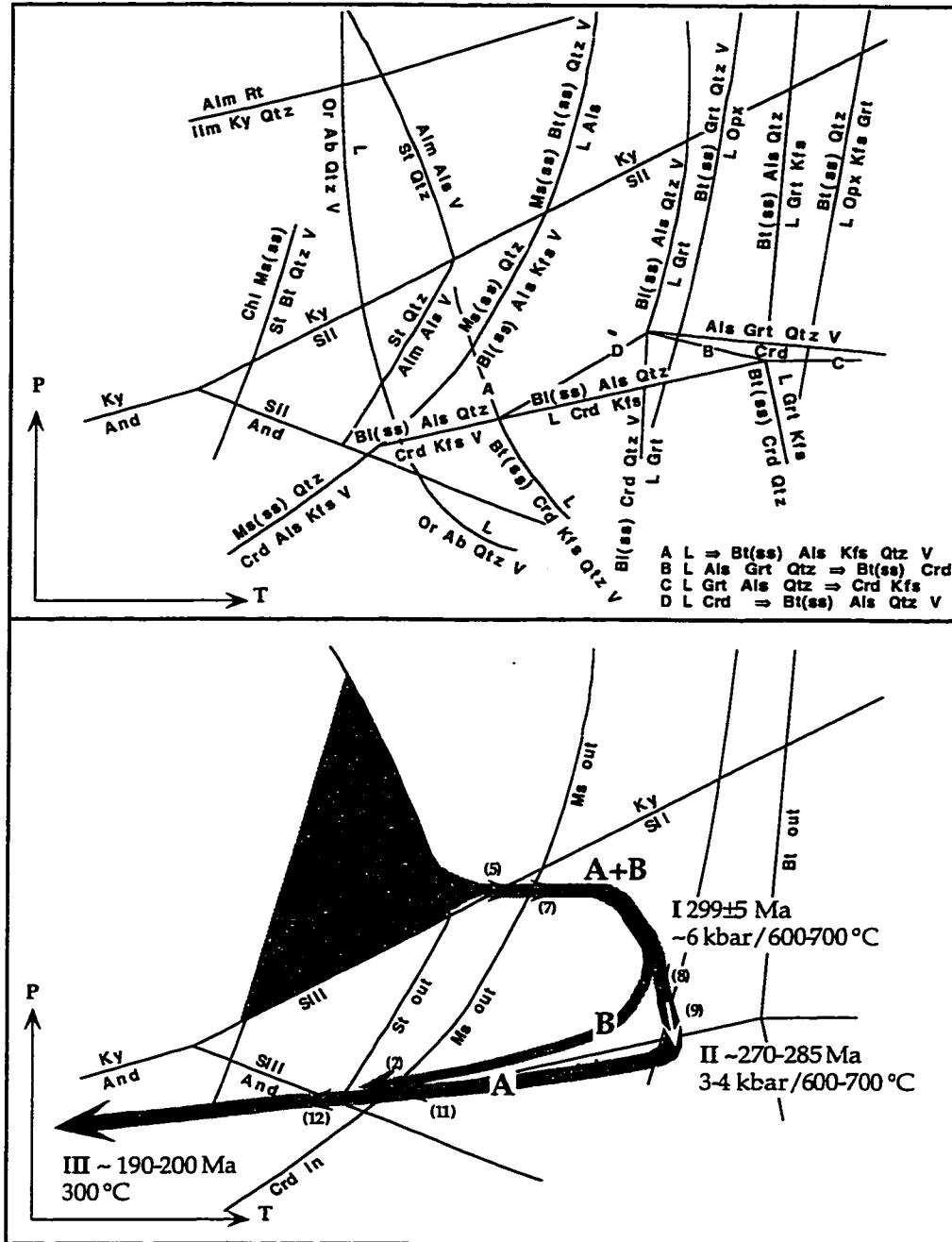


Figure 5.7. Partial petrogenetic grid (5.7A) and proposed PTt path (5.7B). Reaction boundaries adapted after Jones and Brown (1990) and references therein. Reaction $\text{Chl} + \text{Ms(ss)} \Rightarrow \text{St} + \text{Bt} + \text{V}$ taken from Xu et al.(1994). PT conditions and age constraints at the regional thermal maximum (I) and the thermal maximum for rocks proximal to the Upper Mafic Complex discussed in text. Cooling age (III) below $\sim 300^\circ\text{C}$ based on K-Ar biotite ages (Bürgi and Klötzli, 1990). Shaded region encompasses possible prograde PTt paths for the Ivrea zone.

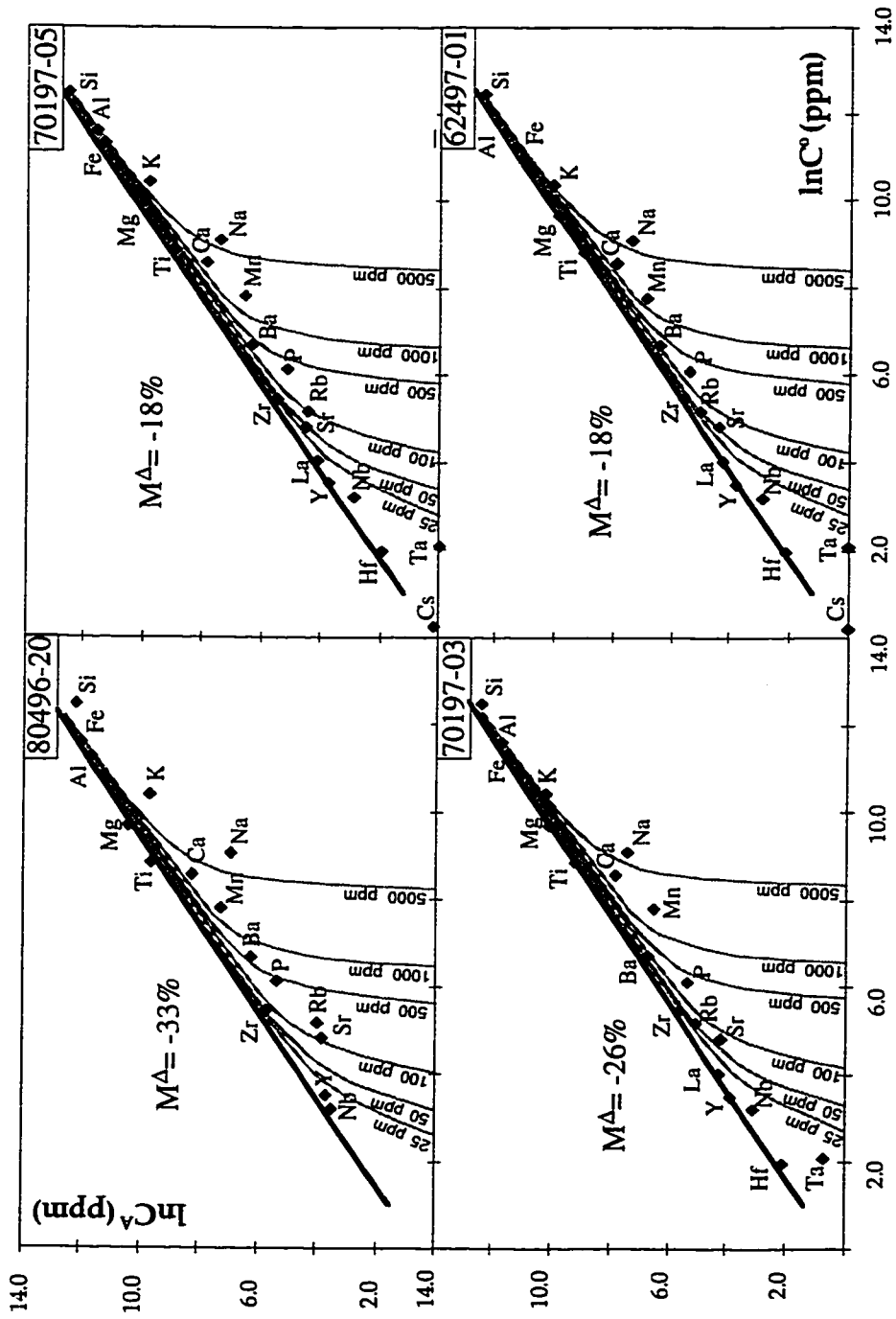


Figure 5.8. Isocon mass balance between migmatitic metapelite melanosome samples and the calculated composite metapelite protolith.

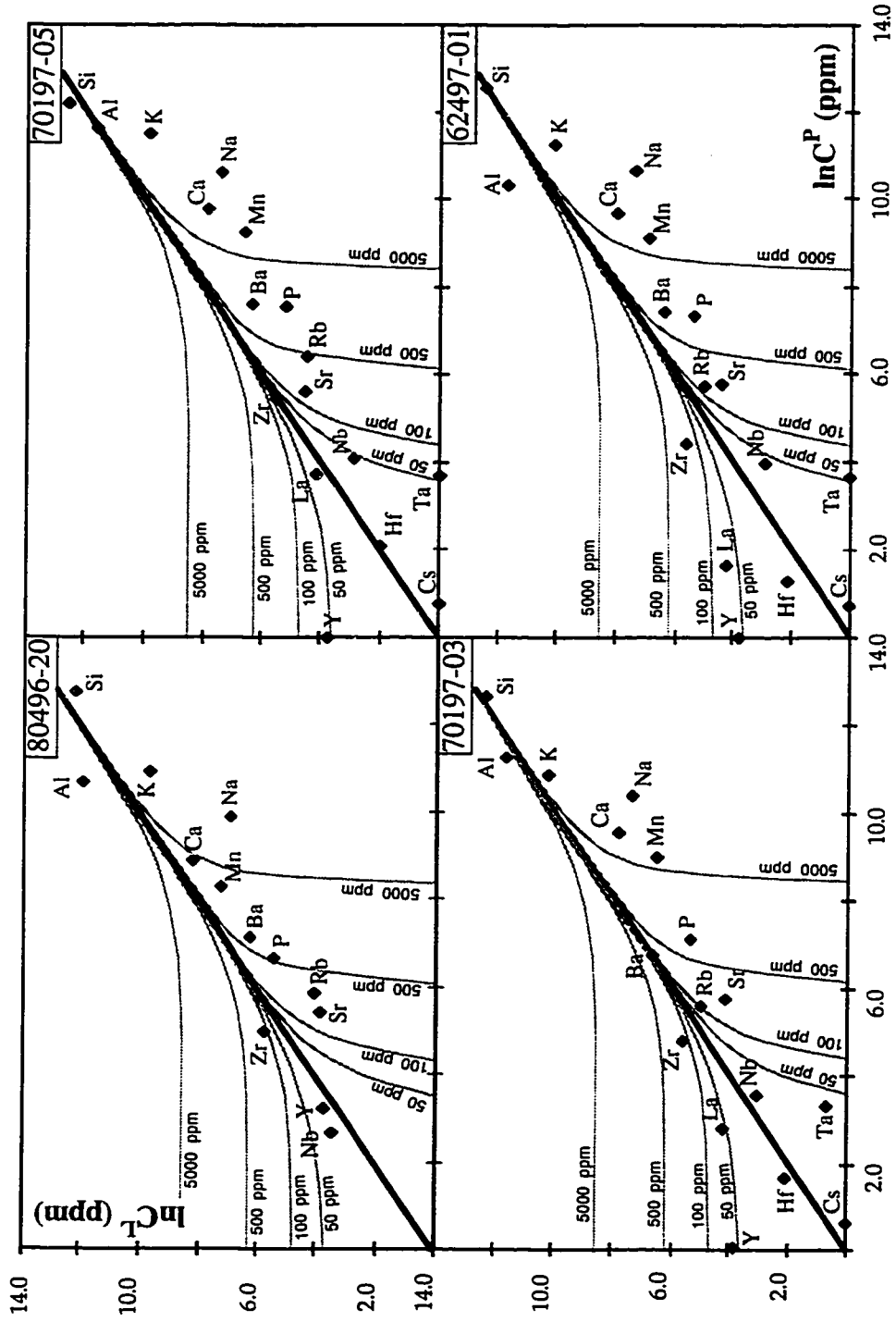


Figure 5.9. Isochron mass balance between the predicted melt and leucosomes immediately adjacent to the migmatitic metapelite melanosomes.

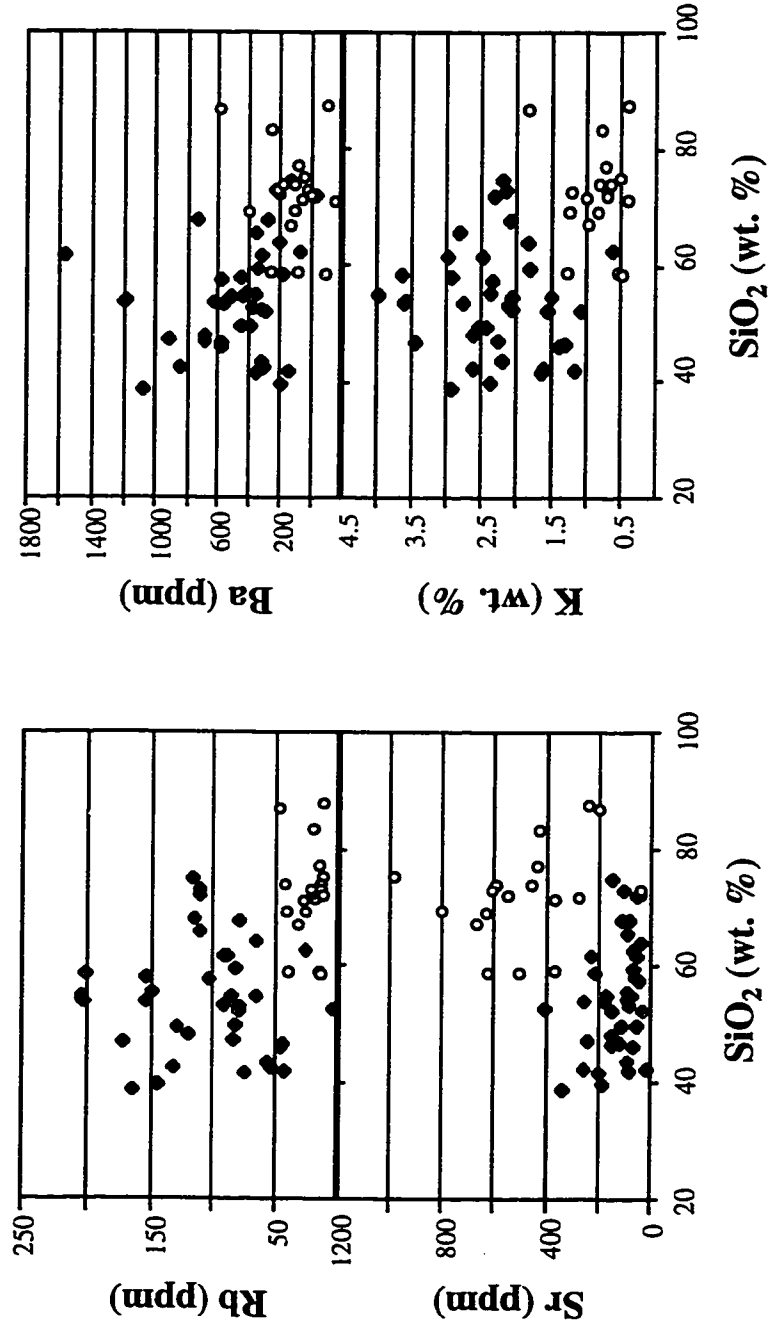


Figure 5.10. Plot of ppm K, Ba, Rb, and Sr vs. SiO₂ for metapelite melanosomes (filled diamonds) and leucotonalite leucosomes (open circles).

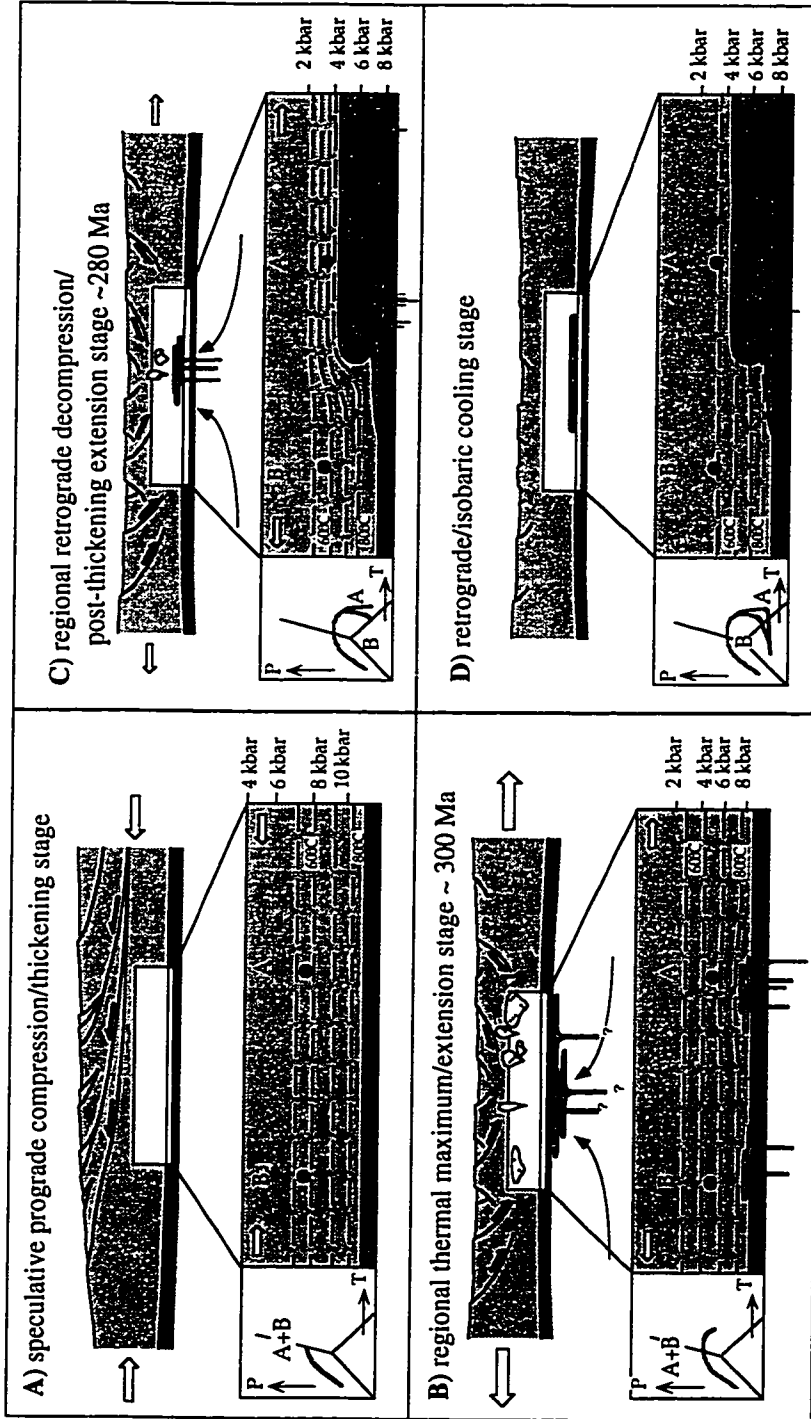


Figure 5.6. Calculated *PT* positions of thermobarometric equilibria for representative metapelite from Val Strona di Posuta and Val Duggia. Bars represent reported *PT* estimates for structurally equivalent metapelite in lower Val Strona di Omega (Henk et al., 1997).

Table 5.1: Whole rock major- and trace-element compositions of representative metapelite melanosomes.

| | 80496 -21 | 062497 -01 | 070197 -03 | 070197 -05 | 061797 -01 | 061797 -03 | 061797 -07A | 061797 -09 | 82395 -01 |
|--------------------------------|--------------|---------------|---------------|---------------|---------------|---------------|----------------|---------------|--------------|
| SiO ₂ | 42.37 | 55.41 | 53.75 | 59.5 | 58.58 | 57.96 | 54.86 | 46.87 | 53.8 |
| TiO ₂ | 2.59 | 1.43 | 1.65 | 1.34 | 1.4 | 1.04 | 1.21 | 1.62 | 0.955 |
| Al ₂ O ₃ | 29.29 | 23.62 | 22.62 | 20.24 | 18.13 | 21.93 | 21.83 | 26.15 | 19 |
| FeO ^T | 14.75 | 10.87 | 12.55 | 10.79 | 10.39 | 8.53 | 9.32 | 12.87 | 12.3 |
| MnO | 0.18 | 0.13 | 0.09 | 0.09 | 0.09 | 0.22 | 0.08 | 0.23 | 0.77 |
| MgO | 5.24 | 3.24 | 3.81 | 3.15 | 3.12 | 2.35 | 2.75 | 3.5 | 2.5 |
| CaO | 0.54 | 0.4 | 0.37 | 0.37 | 0.31 | 0.63 | 0.39 | 0.45 | 1.44 |
| Na ₂ O | 0.14 | 0.22 | 0.23 | 0.22 | 0.57 | 1.48 | 1.43 | 0.57 | 1.79 |
| K ₂ O | 1.93 | 2.85 | 3.31 | 2.18 | 4.4 | 3.51 | 4.79 | 4.14 | 4.36 |
| Cr ₂ O ₃ | | 0.01 | 0.02 | 0.02 | 0.01 | 0.01 | 0.01 | 0.01 | |
| P ₂ O ₅ | 0.05 | 0.05 | 0.05 | 0.04 | 0.1 | 0.14 | 0.1 | 0.08 | 0.12 |
| Nb | 32 | 18 | 22 | 17 | 23 | 16 | 20 | 23 | 38 |
| Zr | 300 | 270 | 280 | 237 | 271 | 168 | 242 | 222 | 205 |
| Y | 40 | 43 | 46 | 42 | 29 | 31 | 31 | 44 | 33 |
| Sr | 46 | 78 | 65 | 90 | 53 | 151 | 109 | 87 | 174 |
| Rb | 54 | 149 | 154 | 82 | 201 | 154 | 205 | 173 | 203 |
| Ba | 505 | 617 | 826 | 544 | 378 | 654 | 551 | 881 | 1400 |
| La | | 68 | 71 | 60 | 52 | 49 | 54 | 86 | |
| Cs | | 1 | 2 | 1 | 8 | 7 | 11 | 6 | |
| Hf | | 8 | 8 | 7 | 8 | 5 | 7 | 7 | |
| Ta | | 1 | 1 | 1 | 2 | 1 | 1 | 1 | |

Table 5.2: Whole rock major- and trace-element compositions of representative leucosomes.

| | 80496-20 | 062497-02 | 070197-04 | 070197-06 |
|--------------------------------|----------|-----------|-----------|-----------|
| SiO ₂ | 71.15 | 72.71 | 68.88 | 71.33 |
| TiO ₂ | 0.12 | 0.14 | 0.45 | 0.42 |
| Al ₂ O ₃ | 16.53 | 16.32 | 16.02 | 15.02 |
| FeO ^F | 0.56 | 1.08 | 2.81 | 1.45 |
| MnO | 0.01 | 0.01 | 0.01 | 0.01 |
| MgO | 0.44 | 0.39 | 0.95 | 0.34 |
| CaO | 7.29 | 3.09 | 2.61 | 3.44 |
| Na ₂ O | 1.38 | 3.7 | 3.44 | 3.74 |
| K ₂ O | 0.47 | 1.17 | 2.37 | 1.38 |
| Cr ₂ O ₃ | | 0.01 | 0.01 | 0.01 |
| P ₂ O ₅ | 0.31 | 0.07 | 0.08 | 0.05 |
| Nb | 4 | 1 | 7 | 6 |
| Zr | 12 | 61 | 211 | 66 |
| Y | 2 | 4 | 11 | 4 |
| Sr | 372 | 619 | 613 | 599 |
| Rb | 28 | 40 | 56 | 27 |
| Ba | 45 | 452 | 954 | 451 |
| La | | 20 | 110 | 47 |
| Cs | | 1 | 1 | 1 |
| Hf | | 1 | 6 | 2 |
| Ta | | 1 | 1 | 1 |

Table 5.3: Representative matrix biotite analyses.

| | 80496-11 | 62097-03 | 70197-10 | 80496-6 | 80496-13 |
|--------------------------------|----------|----------|----------|---------|----------|
| SiO ₂ | 36.80 | 36.45 | 36.45 | 36.78 | 36.91 |
| TiO ₂ | 4.55 | 4.45 | 4.45 | 5.56 | 3.94 |
| Al ₂ O ₃ | 17.19 | 18.11 | 18.11 | 16.57 | 16.59 |
| FeO ^T | 12.38 | 14.00 | 14.00 | 13.60 | 12.91 |
| MnO | 0.00 | 0.01 | 0.01 | 0.00 | 0.02 |
| MgO | 13.93 | 12.37 | 12.37 | 12.14 | 14.33 |
| Na ₂ O | 0.06 | 0.16 | 0.16 | 0.09 | 0.14 |
| K ₂ O | 9.35 | 9.83 | 9.83 | 9.48 | 9.48 |
| Total | 94.26 | 95.39 | 95.39 | 94.21 | 94.31 |
| Si | 5.47 | 5.41 | 5.41 | 5.51 | 5.51 |
| Ti | 0.51 | 0.50 | 0.50 | 0.63 | 0.44 |
| Al | 3.01 | 3.17 | 3.17 | 2.93 | 2.92 |
| Al ^{IV} | 2.53 | 2.59 | 2.59 | 2.49 | 2.49 |
| Al ^{VI} | 0.48 | 0.58 | 0.58 | 0.44 | 0.43 |
| Fe | 1.42 | 1.60 | 1.60 | 1.57 | 1.48 |
| Mn | 0.00 | 0.00 | 0.00 | 0.00 | 0.00 |
| Mg | 3.09 | 2.74 | 2.74 | 2.71 | 3.19 |
| Na | 0.02 | 0.05 | 0.05 | 0.02 | 0.04 |
| K | 1.77 | 1.86 | 1.86 | 1.81 | 1.80 |
| X _{Fe} | 0.26 | 0.29 | 0.29 | 0.28 | 0.27 |
| X _{Mn} | 0.00 | 0.00 | 0.00 | 0.00 | 0.00 |
| X _{Mg} | 0.56 | 0.50 | 0.50 | 0.49 | 0.59 |
| X _{Ti} | 0.09 | 0.09 | 0.09 | 0.11 | 0.08 |
| X _{Al^{VI}} | 0.09 | 0.11 | 0.11 | 0.08 | 0.08 |

Table 5.4: Representative garnet core compositions.

| | 80496-11 | 62097-03 | 70197-10 | 80496-6 | 80496-13 |
|--------------------------------|----------|----------|----------|---------|----------|
| SiO ₂ | 38.44 | 37.94 | 38.19 | 38.13 | 38.46 |
| TiO ₂ | 0.02 | 0.00 | 0.01 | 0.00 | 0.04 |
| Al ₂ O ₃ | 21.66 | 21.90 | 21.71 | 21.53 | 21.26 |
| FeO ^T | 29.68 | 31.68 | 31.53 | 30.26 | 31.22 |
| MnO | 0.72 | 0.69 | 0.74 | 0.49 | 0.62 |
| MgO | 7.50 | 6.50 | 6.64 | 7.66 | 7.05 |
| CaO | 1.52 | 1.41 | 1.33 | 1.12 | 1.22 |
| Total | 99.54 | 100.12 | 100.15 | 99.19 | 99.88 |
| Si | 6.01 | 5.96 | 5.99 | 6.00 | 6.03 |
| Ti | 0.00 | 0.00 | 0.00 | 0.00 | 0.00 |
| Al | 3.99 | 4.05 | 4.01 | 3.99 | 3.93 |
| Fe | 3.88 | 4.16 | 4.13 | 3.98 | 4.10 |
| Mn | 0.10 | 0.09 | 0.10 | 0.07 | 0.08 |
| Mg | 1.75 | 1.52 | 1.55 | 1.79 | 1.65 |
| Ca | 0.26 | 0.24 | 0.22 | 0.19 | 0.21 |
| X _{alm} | 0.65 | 0.69 | 0.69 | 0.66 | 0.68 |
| X _{spe} | 0.02 | 0.02 | 0.02 | 0.01 | 0.01 |
| X _{pyr} | 0.29 | 0.25 | 0.26 | 0.30 | 0.27 |
| X _{grs} | 0.04 | 0.04 | 0.04 | 0.03 | 0.03 |

Table 5.5: Representative matrix plagioclase analyses.

| | 80496-11 | 62097-03 | 70197-10 | 80496-6 | 80496-13 |
|--------------------------------|----------|----------|----------|---------|----------|
| SiO ₂ | 55.51 | 56.80 | 56.80 | 57.64 | 58.97 |
| Al ₂ O ₃ | 27.79 | 27.44 | 27.44 | 27.04 | 25.93 |
| CaO | 8.58 | 9.10 | 9.10 | 7.60 | 7.81 |
| Na ₂ O | 6.43 | 6.15 | 6.15 | 7.35 | 6.68 |
| K ₂ O | 0.14 | 0.15 | 0.15 | 0.21 | 0.14 |
| FeO | 0.01 | 0.08 | 0.08 | | 0.02 |
| Total | 98.46 | 99.72 | 99.72 | 99.85 | 99.55 |
| Si | 2.53 | 2.55 | 2.55 | 2.61 | 2.64 |
| Al | 1.49 | 1.45 | 1.45 | 1.39 | 1.37 |
| Ca | 0.42 | 0.44 | 0.44 | 0.37 | 0.37 |
| Na | 0.57 | 0.54 | 0.54 | 0.65 | 0.58 |
| K | 0.01 | 0.01 | 0.01 | 0.01 | 0.01 |
| Fe | 0.00 | 0.00 | 0.00 | | 0.00 |
| X _{an} | 0.42 | 0.45 | 0.45 | 0.36 | 0.39 |
| X _{ab} | 0.57 | 0.55 | 0.55 | 0.63 | 0.60 |
| X _{or} | 0.01 | 0.01 | 0.01 | 0.01 | 0.01 |

BIBLIOGRAPHY

- Agarwal, P. K., and O'Neill, B. K., 1988, Transport phenomena in multi-particle systems - I. Pressure drop and friction factors: unifying the hydraulic-radius and submerged-object approaches: *Chemical Engineering Science*, v. 43, p. 2487-2499.
- Arzi, A. A., 1978, Critical phenomena in the rheology of partially melted rocks: *Tectonophysics*, v. 44, p. 173-184.
- Asai, S., and Muchi, I., 1978, Theoretical analysis and model experiments on the formation mechanism of channel-type segregation: *Transactions: Iron and Steel Institute of Japan*, v. 18, p. 90-98.
- Barboza, S. A., 1995, The Dynamics of Dehydration Melting and Implications for Melt Extraction in the Lower Crust following Underplating: An Example from the Ivrea-Verbano Zone, northern Italy [M.S. thesis]: University of Washington, 46 p.
- Barboza, S. A., and Bergantz, G. W., 1996, Dynamic model of dehydration melting motivated by a natural analogue: applications to the Ivrea-Verbano zone, northern Italy: *Transactions of the Royal Society of Edinburgh*, v. 87, p. 23-31.
- Barboza, S. A., and Bergantz, G. W., 1997, Melt productivity and rheology: complementary influences on the progress of melting: *Numerical Heat Transfer A*, v. 31, p. 375-392.
- Barboza, S. A., and Bergantz, G. W., 1998, Rheological transitions and the progress of melting of crustal rocks: *Earth and Planetary Science Letters*, v. 158, p. 19-29.
- Barboza, S. A., Bergantz, G. W., and Brown, M., 1999, Regional granulite facies metamorphism in the Ivrea zone: Is the Mafic Complex the smoking gun or a red herring: *Geology*, In review.
- Beard, J. S., and Lofgren, G. E., 1989, Effects of water on the composition of partial melts of greenstone and amphibolite: *Science*, v. 244, p. 195-197.
- Beckermann, C., and Viskanta, R., 1988a, Double-diffusive convection during dendritic solidification of a binary mixture: *Physicochemica Hydrodynamica*, v. 10, no. 2, p. 195-213.

- Beckermann, C., and Viskanta, R., 1988b, Natural convection solid/liquid phase change in porous media: *International Journal of Heat and Mass Transfer*, v. 31, no. 1, p. 35-46.
- Beckermann, C., and Viskanta, R., 1993, Mathematical modeling of transport phenomena during alloy solidification: *Applied Mechanics Reviews*, v. 46, no. 1, p. 1-27.
- Bennon, W. D., and Incropera, F. P., 1987a, A continuum model for momentum, heat and species transport in binary solid-liquid phase change systems I. Model formulation: *International Journal of Heat and Mass Transfer*, v. 30, no. 10, p. 2161-2170.
- Bennon, W. D., and Incropera, F. P., 1987b, A continuum model for momentum, heat and species transport in binary solid-liquid phase change systems II. Application to solidification in a rectangular cavity: *International Journal of Heat and Mass Transfer*, v. 30, no. 10, p. 2171-2187.
- Berckhemer, H., 1968, Topographie des "Ivrea-Körpers" abgeleitet aus seismischen und gravimetrischen Daten: *Schweizerische Mineralogische und Petrographische Mitteilungen*, v. 48, p. 695-732.
- Bergantz, G. W., 1989, Underplating and partial melting: Implications for melt generation and extraction: *Science*, v. 245, p. 1093-1095.
- Bergantz, G. W., 1995, Changing paradigms and techniques for the evaluation of magmatic processes: *Journal of Geophysical Research*, v. 100, p. 17,603-17,613.
- Bergantz, G. W., and Dawes, R., 1994, Aspects of magma generation and ascent in continental lithosphere, in Ryan, M. P., ed., *Magmatic Systems*: San Diego, Academic, p. 291-317.
- Berman, R. G., 1988, Internally-consistent thermodynamic data for minerals in the system $\text{Na}_2\text{O}-\text{K}_2\text{O}-\text{CaO}-\text{MgO}-\text{FeO}-\text{Fe}_2\text{O}_3-\text{Al}_2\text{O}_3-\text{SiO}_2-\text{TiO}_2-\text{H}_2\text{O}-\text{CO}_2$: *Journal of Petrology*, v. 29, p. 445-522.
- Berman, R. G., 1990, Mixing properties of Ca-Mg-Fe-Mn garnets: *American Mineralogist*, v. 75, p. 328-344.
- Bertolani, M., 1959, La formazione basica "Ivrea Verbano" e la sua posizione nel quadro geologico-petrografico della Bassa Valsesia e del Biellese: *Periodico di Mineralogia*, v. 28, p. 151-209.
- Bird, R. B., Stewart, W. E., and Lightfoot, E. N., 1960, *Transport Phenomena*: New York, John Wiley & Sons, 780 p.

- Bittner, D., and Schmeling, H., 1995, Numerical modelling of melting processes and induced diapirism in the lower crust: *Geophysical Journal International*, v. 123, p. 59-70.
- Bohlen, S. R., 1987, Pressure-temperature-time paths and a tectonic model for the evolution of granulites: *Journal of Geology*, v. 95, p. 617-632.
- Boriani, A., Bigioggero, B., and Origoni Giobbi, E., 1977, Metamorphism, tectonic evolution, and tentative stratigraphy of the "Serie dei Laghi"-geological map of the Verbania area (northern Italy): *Memorie degli Istituti di Geologia e Mineralogia dell'Universita di Padova*, v. 32, p. 1-25.
- Boriani, A., Burlini, L., Caironi, V., Origoni Giobbi, E., Sassi, A., and Sesana, E., 1988, Geological and petrological studies on the Hercynian plutonism of Serie dei Laghi-geological map of its occurrence between Valsesia and Lago Maggiore (N-Italy): *Rendiconti della Società Italiana di Mineralogia e Petrologia*, v. 43-2, p. 367-384.
- Boriani, A., Burlini, L., and Sacchi, R., 1990a, The Cossato-Mergozzo-Brissago line and the Pogallo line (southern Alps, N-Italy) and their relationships with the late-Hercynian magmatic and metamorphic events: *Tectonophysics*, v. 182, p. 91-102.
- Boriani, A., Caironi, V., Origoni Giobbi, E., and Vannucci, R., 1992, The Permian intrusive rocks of Serie dei Laghi (Western Southern Alps): *Acta Vulcanologica*, v. 2, p. 73-86.
- Boriani, A., Giobbi Origoni, E., Borghi, A., and Caironi, V., 1990b, The evolution of the "Serie Dei Laghi" (Strona-Ceneri and Schisti dei Laghi): the upper component of the Ivrea-Verbano crustal section; Southern Alps, North Italy and Ticino, Switzerland: *Tectonophysics*, v. 182, p. 103-118.
- Boriani, A., and Sacchi, R., 1973, Geology of the junction between the Ivrea-Verbano and Strona-Ceneri zones (Southern Alps): *Memorie degli Istituti di Geologia e Mineralogia dell'Universita di Padova*, v. 28, p. 1-35.
- Bowers, J. R., Kerrick, D. M., and Furlong, K. P., 1990, Conduction model for the thermal evolution of the Cuscutic aureole, Maine: *American Journal of Science*, v. 290, p. 644-665.
- Brodie, K. H., 1995, The development of oriented symplectites during deformation: *Journal of Metamorphic Geology*, v. 13, p. 499-508.
- Brodie, K. H., Rex, D., and Rutter, E. H., 1989, On the age of deep crustal extensional faulting in the Ivrea Zone, northern Italy, *in* Coward, M. P., Dietrich, D., and

- Park, R. G., eds., *Alpine Tectonics*: London, Geological Society Special Publication, v. 45, p. 203-210.
- Brodie, K. H., and Rutter, E. H., 1987, Deep crustal extensional faulting in the Ivrea Zone of northern Italy: *Tectonophysics*, v. 140, p. 193-212.
- Brown, G. C., and Fyfe, W. S., 1970, The production of granitic melts during ultrametamorphism: *Contributions to Mineralogy and Petrology*, v. 28, p. 310-318.
- Brown, M., 1994, The generation, segregation, ascent and emplacement of granite magma: The migmatite-to-crustally-derived granite connection in thickened orogens: *Earth Science Reviews*, v. 36, p. 83-130.
- Brown, M., Averkin, Y. A., McLellan, E. L., and Sawyer, E. W., 1995, Melt segregation in migmatites: *Journal of Geophysical Research*, v. 100, p. 655-679.
- Buntebarth, G., 1991, Thermal models of cooling., *in* Voll, G., Topel, J., Pattison, D. R. M., and Seifert, F., eds., *Equilibrium and Kinetics in Contact Metamorphism: The Ballachulish Igneous Complex and its Aureole*: Heidelberg, Springer-Verlag, p. 379-404.
- Bürgi, A., and Klötzli, U., 1990, New data on the evolutionary history of the Ivrea zone (northern Italy): *Bulletin of the Swiss Association of Petroleum Geologists and Engineers*, v. 56, p. 49-70.
- Burke, M. M., and Fountain, D. M., 1990, Seismic properties of rocks from an exposure of extended continental crust - new laboratory measurements from the Ivrea Zone: *Tectonophysics*, v. 182, p. 119-146.
- Campbell, I. H., and Turner, J. S., 1987, A laboratory investigation of assimilation at the top of a basaltic magma chamber: *Journal of Geology*, v. 95, p. 155-172.
- Capedri, S., 1971, *Sulle rocce della formazione basica Ivrea-Verbanò. 2. Petrografia delle granuliti e rocce derivate nella Val Mastallone (Vercelli) e loro evoluzione petrogenetica*: *Memorie della Società Geologica Italiana*, v. 10, p. 277-312.
- Capedri, S., and Rivalenti, G., 1973, Metamorphic crystallisations in relation to plastic deformations in a pelitic series (Valle Strona, Vercelli, Italy): *Bollettino della Società Geologica Italiana*, v. 92, p. 649-668.
- Carrington, D. P., and Harley, S. L., 1995, Partial melting and phase relations in high-grade metapelites: An experimental petrogenetic grid in the KFMASH system: *Contributions to Mineralogy and Petrology*, v. 120, p. 270-291.

- Chu, T. Y., and Hickox, C. E., 1990, Thermal convection with large viscosity variation in an enclosure with localized heating: *Journal of Heat Transfer*, v. 112, p. 388-395.
- Clemens, J. D., and Mawer, C. K., 1992, Granitic magma transport by fracture propagation: *Tectonophysics*, v. 204, p. 339-360.
- Conrad, W. K., Nicholls, I. A., and Wall, V. J., 1988, Water-saturated and -undersaturated melting of metaluminous and peraluminous crustal compositions at 10 kb: evidence for the origin of silicic magmas in the Taupo Volcanic Zone, New Zealand, and other occurrences: *Journal of Petrology*, v. 29, p. 765-803.
- Cruden, A. R., Koyi, H., and Schmeling, H., 1995, Diapiric basal entrainment of mafic into felsic magma: *Earth and Planetary Science Letters*, v. 131, p. 321-340.
- Davidson, I., McCarthy, M., Powell, D., Torres, H. H. F., and Santos, C. A., 1995, Laminar flow in shear zones: the Pernambuco Shear Zone, NE Brazil: *Journal of Structural Geology*, v. 17, p. 149-161.
- De Yoreo, J. J., Lux, D. R., and Guidotti, C. V., 1991, Thermal modelling in low-pressure/high-temperature metamorphic belts: *Tectonophysics*, v. 188, p. 209-238.
- Demarchi, G., Quick, J. E., Sinigoi, S., and Mayer, A., 1998, Pressure gradient and original orientation of a lower-crustal intrusion in the Ivrea-Verbano zone, northern Italy: *Journal of Geology*, v. 106, p. 609-622.
- Dostal, J., and Capedri, S., 1979, Rare earth elements in high-grade metamorphic rocks from the western Alps: *Lithos*, v. 12, p. 41-49.
- Ellis, D. J., 1987, Origin and evolution of granulites in normal and thickened crust: *Geology*, v. 15, p. 167-170.
- Fountain, D. M., 1976, The Ivrea-Verbano and Strona-Ceneri zones, northern Italy: A cross-section of the continental crust -- New evidence from seismic velocities: *Tectonophysics*, v. 33, p. 145-165.
- Fountain, D. M., 1989, Growth and modification of lower continental crust in extended terrains: The role of extension and magmatic underplating, *in* Mereu, R. F., Mueller, S., and Fountain, D. M., eds., *Properties and Processes of Earth's Lower Crust: Geophysical Monograph Series: Washington D.C., AGU*, p. 287-299.

- Fowler, M. G., 1986, Large-ion lithophile element characteristics of an amphibolite facies to granulite facies transition at Gruinard Bay, Northwest Scotland: *Journal of Metamorphic Geology*, v. 4, p. 345-359.
- Frost, B. R., and Chacko, T., 1989, The granulite uncertainty principle: limitations on thermobarometry in granulites: *Journal of Geology*, v. 97, p. 435-450.
- Fuhrman, M. L., and Lindsley, D. H., 1988, Ternary feldspar modeling and thermometry: *American Mineralogist*, v. 73, p. 201-215.
- Furlong, K. P., and Londe, M. D., 1986, Thermal - mechanical consequences of Basin and Range extension, *in* Mayer, L., ed., *Extensional tectonics of the Southwestern United States: a perspective on processes and kinematics*, Geological Society of America Special Paper, p. 22-30.
- Fyfe, W. S., 1973, The granulite facies, partial melting and the Archean crust: *Philosophical Transactions of the Royal Society of London Series A*, v. 273, p. 457-461.
- Gans, P. B., 1987, An open-system, two-layer crustal stretching model for the eastern Great Basin: *Tectonics*, v. 6, p. 1-12.
- Gansser, A., 1968, The Insubric Line, a major geotectonic problem: *Schweizerische Mineralogische und Petrographische Mitteilungen*, v. 48, p. 123-143.
- Ghiorso, M. S., and Sack, R. O., 1995, Chemical mass transfer in magmatic processes IV. A revised and internally consistent thermodynamic model for the interpolation and extrapolation of liquid-solid equilibria in magmatic systems at elevated temperatures and pressures: *Contributions to Mineralogy and Petrology*, v. 119, p. 197-212.
- Giese, P., 1968, Die struktur der erdkruste im bereich der Ivrea-Zone. Ein vergleich verschiedener, seismischer interpretationen und der versuch einer petrographisch-geologischen deutung: *Schweizerische Mineralogische und Petrographische Mitteilungen*, v. 48, p. 261-284.
- Giese, P., Reutter, K.-J., Jacobshagen, V., and Nicolich, R., 1982, Explosion seismic crustal studies in the Alpine Mediterranean region and their implications to tectonic processes., *in* Berckhemer, H., and Hsü, K., eds., *Alpine-Mediterranean Geodynamics*, AGU, p. 39-73.
- Grant, J. A., 1986, The isocon diagram - A simple solution to Gresens' equation for metasomatic alteration: *Economic Geology*, v. 81, p. 1976-1082.

- Grant, J. A., and Frost, B. R., 1990, Contact metamorphism and partial melting of pelitic rocks in the aureole of the Laramie anorthosite complex, Morton Pass, Wyoming: *American Journal of Science*, v. 290, p. 425-472.
- Gresens, R. L., 1967, Composition-volume relationships of metasomatism: *Chemical Geology*, v. 2, p. 47-55.
- Grunder, A. L., 1995, Material and thermal roles of basalt in crustal magmatism: Case study from eastern Nevada: *Geology*, v. 23, p. 952-956.
- Guidotti, C. V., and Dyar, M. D., 1991, Ferric iron in metamorphic biotite and its petrologic and crystallochemical implications: *American Mineralogist*, v. 76, p. 161-175.
- Hamilton, W. B., 1981, Crustal evolution by arc magmatism: *Philosophical Transactions of the Royal Society of London Series A*, v. 301, p. 279-291.
- Hamilton, W. B., 1988, Plate tectonic and island arcs: *Bulletin of the Geological Society of America*, v. 100, p. 1,503-1,527.
- Handy, M. R., 1987, The structure, age and kinematics of the Pogallo fault zone; Southern Alps, northwestern Italy: *Eclogae Geologicae Helvetiae*, v. 80, p. 593-632.
- Harley, S. L., 1989, The origins of granulites: a metamorphic perspective: *Geological Magazine*, v. 126, p. 215-331.
- Harris, N., Ayres, M., and Massey, J., 1995, The incongruent melting of muscovite: the implications for the geochemistry and extraction of granite magmas: *Journal of Geophysical Research*, v. 100, p. 15,767-15,777.
- Henk, A., Franz, L., Teufel, S., and Oncken, O., 1997, Magmatic underplating, extension, and crustal reequilibration: Insights from a cross-section through the Ivrea Zone and Strona-Ceneri Zone, northern Italy: *Journal of Geology*, v. 105, p. 367-377.
- Hildreth, W., and Moorbath, S., 1988, Crustal contributions to arc magmatism in the Andes of Central Chile: *Contributions to Mineralogy and Petrology*, v. 98, p. 455-489.
- Hirn, A., Nadir, S., Thouvenot, F., Nicolich, R., Pellis, G., Scarascia, S., Tabacco, I., Castellano, F., and Merlanti, F., 1989, Mapping the Moho of the Western Alps by wide angle reflection seismics: *Tectonophysics*, v. 162, p. 193-202.

- Hollister, L. S., and Crawford, M. L., 1986, Melt-enhanced deformation: a major tectonic process: *Geology*, v. 14, p. 558-561.
- Hunziker, J. C., and Zingg, A., 1980, Lower Palaeozoic amphibolite to granulite facies metamorphism in the Ivrea zone (Southern Alps, northern Italy): *Schweizerische Mineralogische und Petrographische Mitteilungen*, v. 60, p. 181-213.
- Huppert, H., and Sparks, R. S. J., 1991, Comments on "on convective style and vigor in sheet-like magma chambers" by Bruce D. Marsh: *Journal of Petrology*, v. 32, p. 851-854.
- Huppert, H. E., and Sparks, R. S. J., 1988, The generation of granitic magmas by intrusion of basalt into continental crust: *Journal of Petrology*, v. 29, no. 3, p. 599-624.
- Hyndman, D. W., 1981, Controls on source and depth of emplacement of granitic magma: *Geology*, v. 9, p. 244-249.
- Irvine, T. N., 1970, Heat transfer during solidification of layered intrusions. I. sheets and sills: *Canadian Journal of Earth Science*, v. 7, p. 1031-1061.
- Jarchow, C. M., Thompson, G. A., Catchings, R. D., and Mooney, W. D., 1993, Seismic evidence for active magmatic underplating beneath the Basin and Range Province, western United States: *Journal of Geophysical Research*, v. 98, p. 22,095-22,108.
- Jaupart, C., and Tait, S., 1995, The dynamics of differentiation in magma reservoirs: *Journal of Geophysical Research*, v. 100, p. 17,615-17,636.
- Jeffrey, D. J., and Acrivos, A., 1976, The rheological properties of suspensions of rigid particles: *Journal of the American Institute of Chemical Engineers*, v. 22, p. 417-432.
- Johannes, W., 1984, Beginning of melting in the granite system Qz-Or-Ab-An-H₂O: *Contributions to Mineralogy and Petrology*, v. 86, p. 264-273.
- Jones, K. A., and Bown, M., 1990, High-temperature 'clockwise' *P-T* paths and melting in the development of regional migmatites: an example from southern Brittany, France: *Journal of Metamorphic Geology*, v. 8, p. 551-578.
- Kay, R. W., and Kay, S. M., 1980, Chemistry of the lower crust: inferences from magmas and xenoliths., *in* National Research Council and Geophysics Study Committee, eds., *Continental Tectonics*: Washington D.C., National Academy of Sciences, p. 139-150.

- Kay, R. W., and Kay, S. M., 1981, The nature of the lower continental crust: Inferences from geophysics, surface geology, and crustal xenoliths: *Reviews in Geophysics*, v. 19, p. 271-297.
- Kissling, E., 1980, *Krustenaufbau und Isostasie in der Schweiz*. [Ph.D. thesis]: ETH Zürich.
- Köppel, V., 1974, Isotopic U-Pb ages of monazites and zircons from the crust-mantle transition and adjacent units of the Ivrea and Ceneri zones (Southern Alps, Italy): *Contributions to Mineralogy and Petrology*, v. 43, p. 55-70.
- Köppel, V., and Grünfelder, M., 1971, A study of inherited and newly formed zircons from paragneisses and granitised sediments of the Strona-Ceneri Zone (Southern Alps): *Schweizerische Mineralogische und Petrographische Mitteilungen*, v. 51, p. 385-410.
- Krieger, I. M., and Dougherty, T. J., 1959, A mechanism for non-Newtonian flow in suspensions of rigid spheres: *Transactions of the Rheological Society*, v. 3, p. 137-152.
- Lachenbruch, A. H., and Sass, J. H., 1978, Models of an extending lithosphere and heat flow in the Basin and Range province: *Geological Society of America Memoir*, v. 152, p. 209-250.
- Le Breton, N. L., and Thompson, A. B., 1988, Fluid-absent (dehydration) melting of biotite in metapelites in the early stages of crustal anatexis: *Contributions to Mineralogy and Petrology*, v. 99, p. 226-237.
- Lister, G. S., Etheridge, M. A., and Symonds, P. A., 1986, Detachment faulting and the evolution of passive continental margins: *Geology*, v. 14, p. 246-250.
- Mareschal, J.-C., and Bergantz, G. B., 1990, Constraints on thermal models of the Basin and Range province: *Tectonophysics*, v. 174, p. 137-146.
- Marsh, B. D., 1981, On the crystallinity, probability of occurrence, and rheology of lava and magma: *Contributions to Mineralogy and Petrology*, v. 78, p. 85-98.
- Marsh, B. D., 1989, On convective style and vigor in sheet-like magma bodies: *Journal of Petrology*, v. 30, no. 3, p. 479-530.
- Marsh, B. D., 1991, Reply to comments of Huppert and Sparks: *Journal of Petrology*, v. 32, p. 855-860.
- Matte, P., 1986, Tectonics and plate tectonics for the Variscan belt of Europe: *Tectonophysics*, v. 177, p. 141-156.

- Matte, P., 1991, Accretionary history and crustal evolution of the Variscan belt in Europe: *Tectonophysics*, v. 196, p. 309-337.
- McCarthy, T. C., and Patiño Douce, A. E., 1997, Experimental evidence for high temperature felsic melts formed during basaltic intrusion of the deep crust: *Geology*, v. 25, p. 463-466.
- McMullin, D. W. A., Berman, R. G., and Greenwood, H. J., 1991, Calibration of the SGAM thermobarometer for pelitic rocks using data from phase-equilibrium experiments and natural assemblages: *Canadian Mineralogist*, v. 29, p. 889-908.
- Mehnert, K., 1975, The Ivrea zone, a model of the deep crust: *Neues Jahrbuch Mineralogie Abhandlungen*, v. 125, p. 156-199.
- Mehnert, K. R., 1968, Migmatites and the origin of granitic rocks: Amsterdam, Elsevier, 335-342 p.
- Miller, C. F., Watson, E. B., and Harrison, T. M., 1988, Perspectives on the source, segregation and transport of granitoid magmas: *Transactions of the Royal Society of Edinburgh*, v. 79, p. 135-156.
- Mueller, S., Ansorge, J., Egloff, R., and Kissling, E., 1980, A crustal cross section along the Swiss Geotraverse from the Rhinegraben to the Po Plain: *Eclogae Geologicae Helvetiae*, v. 73, p. 463-483.
- Newhouse, L. A., and Pozrikidis, C., 1990, The Rayleigh-Taylor instability of a viscous liquid layer resting on a plane wall: *Journal of Fluid Mechanics*, v. 217, p. 615-638.
- Ni, J., and Beckermann, C., 1991, A volume-averaged two-phase model for transport phenomena during solidification: *Metallurgical Transactions B*, v. 22B, p. 349-361.
- Nicolas, A., 1989, Structures of ophiolites and dynamics of ocean lithosphere: Dordrecht, Kluwer, Academic, 367 p.
- Nicolas, A., Hirn, A., Nicolich, R., Polino, R., and the ECORS-CROP Working Group, 1990, Lithospheric wedging in the Western Alps inferred from the ECORS-CROP traverse: *Geology*, v. 18, p. 587-590.
- Oldenburg, C. M., and Spera, F. J., 1991, Numerical modeling of solidification and convection in a viscous pure binary eutectic system: *International Journal of Heat and Mass Transfer*, v. 34, p. 2107-2121.

- Oldenburg, C. M., and Spera, F. J., 1992, Hybrid model for solidification and convection: *Numerical Heat Transfer B*, v. 21, p. 217-229.
- Olsen, S. N., and Grant, J. A., 1991, Isocon analysis of migmatization in the Front Range, Colorado, USA: *Journal of Metamorphic Geology*, v. 9, p. 151-164.
- Patankar, S. V., 1980, *Numerical Heat Transfer and Fluid Flow*: New York, Hemisphere, 197 p.
- Patiño Douce, A. E., and Johnston, A. D., 1991, Phase equilibria and melt productivity in the pelitic system: implications for the origin of peraluminous granitoids and aluminous granulites: *Contributions to Mineralogy and Petrology*, v. 107, p. 202-218.
- Pin, C., 1986, Datation U/Pb sur zircons a 285 Ma du complexe gabbro-dioritique du Val Sesia - Val Mastallone et age tardihercynien du metamorphisme granulitique de la zone Ivrea-Verbanò (Italie): *Comptes Rendus de l'Academie des Sciences, Ser. 2*, v. 303, p. 827-830.
- Pin, C., 1990, Evolution of the lower crust in the Ivrea zone: a model based on isotopic and geochemical data, *in* Vielzeuf, D., and Vidal, P., eds., *Granulites and Crustal Evolution*: Dordrecht, Kluwer, p. 87-110.
- Pin, C., and Sills, J. D., 1986, Petrogenesis of layered gabbros and ultramafic rocks from Val Sesia, the Ivrea zone, NW Italy: trace element and isotope geochemistry: *Geological Society Special Publication*, v. 24, p. 231-249.
- Pitcher, W. S., 1993, *The Nature and Origin of Granite*: London, Blackie Academic & Professional, 321 p.
- Prakash, C., and Voller, V. R., 1989, On the numerical solution of continuum mixture model equations describing binary solid-liquid phase change: *Numerical Heat Transfer B*, v. 15, p. 171-189.
- Quick, J. E., Sinigoi, S., and Mayer, A., 1994, Emplacement dynamics of a large mafic intrusion in the lower crust of the Ivrea-Verbanò Zone, northern Italy: *Journal of Geophysical Research*, v. 99, p. 21,559-21,573.
- Rivalenti, G., Garutti, G., Rossi, A., Siena, F., and Sinigoi, S., 1980, Existence of different peridotite types and of a layered igneous complex in the Ivrea zone of the Western Alps: *Journal of Petrology*, v. 22, p. 127-153.
- Rivalenti, G., Rossi, A., Siena, F., and Sinigoi, S., 1984, The layered series of the Ivrea-Verbanò igneous complex, Western Alps, Italy: *Tschermaks Mineralogische Petrgraphische Mitteilungen*, v. 33, p. 77-99.

- Rivalenti, R., Garuti, G., and Rossi, A., 1975, The origin of the Ivrea-Verbano Basic Formation (western Italian Alps) - whole rock geochemistry: *Bollettino della Società Geologica Italiana*, v. 94, p. 1149-1186.
- Roscoe, R., 1952, The Viscosity of Suspensions of Rigid Spheres: *British Journal of Applied Physics*, v. 3, p. 267-269.
- Rosten, H. I., and Spalding, D. B., 1987, The PHOENICS Reference Manual, CHAM TR/200.
- Rudnick, R. L., and Presper, T., 1990, Geochemistry of intermediate/- to high-pressure granulites, *in* Vielzeuf, D., and Vidal, P. eds., *Granulites and Crustal Evolution*: Dordrecht, Kluwer, p. 523-550.
- Rushmer, T., 1991, Partial melting of two amphibolites: contrasting experimental results under fluid-absent conditions: *Contributions to Mineralogy and Petrology*, v. 107, p. 41-59.
- Rushmer, T., 1995, An experimental deformation study of partially molten amphibolite: application to low-melt fraction segregation: *Journal of Geophysical Research*, v. 100, p. 15,681-15,695.
- Rutter, E. H., and Neumann, D. H. K., 1995, Experimental deformation of partially molten Westerly granite under fluid-absent conditions, with implications for the extraction of granitic magmas: *Journal of Geophysical Research*, v. 100, p. 15,697-15,715.
- Sacchi, R., 1962, Nuovi data geologici sull tavoletta Valle Mosso: *Bollettino del Servizio Geologica d'Italia*, v. 83, p. 51-59.
- Sawyer, E. W., 1991, Disequilibrium melting and the rate of melt-residuum separation during migmatization of mafic rocks from the Grenville Front, Quebec: *Journal of Petrology*, v. 32, p. 701-738.
- Sawyer, E. W., 1994, Melt segregation in the continental crust: *Geology*, v. 22, p. 1019-1022.
- Schmid, R., 1967, Zur petrographie und struktur der Zone Ivrea-Verbano zwischen Valle d'Ossola und Val Grande (Prov. Novara Italien): *Schweizerische Mineralogische und Petrographische Mitteilungen*, v. 47, p. 935-1117.
- Schmid, R., 1978/1979, Are the metapelites in the Ivrea zone restites?: *Memorie degli Istituti di Geologia e Mineralogia dell'Universita di Padova*, v. 33, p. 67-69.

- Schmid, R., and Wood, B. J., 1976, Phase relationships in granulitic metapelites from the Ivrea-Verbano zone (northern Italy): *Contributions to Mineralogy and Petrology*, v. 54, p. 255-279.
- Schmid, S. M., 1993, Ivrea zone and adjacent Southern Alpine basement, *in* von Raumer, J. F., and Neubauer, F., eds., *Pre-Mesozoic Geology in the Alps*: Berlin, Springer-Verlag, p. 567-583.
- Schmid, S. M., Zingg, A., and Handy, M., 1987, The kinematics of movements along the Insubric Line and the emplacement of the Ivrea Zone: *Tectonophysics*, v. 135, p. 47-66.
- Schnetger, B., 1994, Partial melting during the evolution of the amphibolite-to-granulite-facies gneisses of the Ivrea Zone, northern Italy: *Chemical Geology*, v. 113, p. 71-101.
- Schulze, F., Behrens, H., and Holtz, F., 1994, Effect of water on the viscosity of haplogranitic melts. Experimental investigation using the falling sphere method: EOS, *Transactions of the American Geophysical Union*, v. 75 (44), p. 724.
- Shaw, H. R., 1972, Viscosities of magmatic liquids: an empirical method of prediction: *American Journal of Science*, v. 272, p. 870-893.
- Shervais, J. W., 1979, Thermal emplacement model for the alpine lherzolite massif at Balmuccia, Italy: *Journal of Petrology*, v. 20, p. 795-820.
- Sighinolfi, G. P., 1969, K-Rb ratio in high-grade metamorphism: A confirmation of the hypothesis of a continual crustal evolution: *Contributions to Mineralogy and Petrology*, v. 21, p. 346-356.
- Sighinolfi, G. P., and Gorgoni, C., 1978, Chemical evolution of high-grade metamorphic rocks - anatexis and remotion of material from granulite terrains: *Chemical Geology*, v. 22, p. 157-176.
- Sills, J. D., 1984, Granulite facies metamorphism in the Ivrea zone, N.W. Italy: *Schweizerische Mineralogische und Petrographische Mitteilungen*, v. 64, p. 169-191.
- Sills, J. D., and Tarney, J., 1984, Petrogenesis and tectonic significance of amphibolites interlayered with metasedimentary gneisses of the Ivrea zone, Southern Alps, northwest Italy: *Tectonophysics*, v. 107, p. 187-208.
- Sinigoï, S., Quick, J. E., Clemens-Knott, D., Mayer, A., Dimarchi, G., Mazzucchelli, M., Negrini, L., and Rivalenti, G., 1994, Chemical evolution of a large mafic

- intrusion in the lower crust, Ivrea-Verbano Zone, northern Italy: *Journal of Geophysical Research*, v. 99, p. 21,575-21,590.
- Sinigoi, S., Quick, J. E., Mayer, A., and Budahn, J., 1996, Influence of stretching and density contrasts on the chemical evolution of continental magmas: an example from the Ivrea-Verbano zone: *Contributions to Mineralogy and Petrology*, v. 123, p. 238-250.
- Sinigoi, S., Quick, J. E., Mayer, A., and Demarchi, G., 1995, Density-controlled assimilation of underplated crust, Ivrea-Verbano zone, Italy: *Earth and Planetary Science Letters*, v. 129, p. 183-191.
- Sinton, J. M., and Detrick, R., 1992, Mid-ocean ridge magma chambers: *Journal of Geophysical Research*, v. 97, p. 197-216.
- Snoke, A. W., Kalakay, T. J., and Fountain, D. M., 1994, The polyphase history of the Ivrea-Verbano Zone, southern Alps, northern Italy as indicated by a new structural transect: *Geological Society of America Abstracts with programs*, v. 26, no. 7, p. A-197.
- Snoke, A. W., Kalakay, T. J., Quick, J. E., and Sinigoi, S., 1999, Deep-crustal shear zone as a result of mafic igneous intrusion in the lower crust, Ivrea-Verbano Zone, Southern Alps, Italy: *Earth and Planetary Science Letters*, v. in review.
- Stüwe, K., Sandiford, M., and Powell, R., 1993, Episodic Metamorphism and Deformation in Low-Pressure, High-Temperature Terranes: *Geology*, v. 21, p. 829-832.
- Swanson, D. A., Cameron, K. A., Evarts, R. C., Pringle, P. T., and Vance, J. A., 1989, Cenozoic volcanism in the Cascade Range and Columbia Plateau, southern Washington and northernmost Oregon: *New Mexico Bureau of Mines and Mineral Resources Memoir*, v. 47, p. 1-50.
- Symmes, G. H., and Ferry, J. M., 1995, Metamorphism, fluid flow and partial melting in pelitic rocks from the Onawa contact aureole, central Maine, USA: *Journal of Petrology*, v. 36, p. 587-612.
- Teufel, S., and Schärer, U., 1989, Unraveling the age of high-grade metamorphism of the Ivrea zone: a monazite single-grain and small fraction study: *TERRA abstracts*, v. 1, p. 350.
- Thompson, A. B., 1982, Dehydration melting of pelitic rocks and the generation of H₂O undersaturated granitic liquids: *American Journal of Science*, v. 282, p. 1567-1595.

- Thompson, A. B., and Tracy, R. J., 1979, Model systems for the anatexis of pelitic rocks. II. Facies series melting reactions in the system CaO-KAlO₂-NaAlO₂-Al₂O₃-H₂O: *Contributions to Mineralogy and Petrology*, v. 70, p. 429-438.
- Turcotte, D. L., and Schubert, G., 1982, *Geodynamics: Applications of Continuum Physics to Geologic Problems*: New York, John Wiley, 450 p.
- van der Molen, I., and Paterson, M. S., 1979, Experimental deformation of partially-melted granite: *Contributions to Mineralogy and Petrology*, v. 70, p. 299-318.
- Vavra, G., Gebauer, D., Schmid, R., and Compston, W., 1996, Multiple zircon growth and recrystallization during polyphase Late Carboniferous to Triassic metamorphism in granulites of the Ivrea zone (Southern Alps): an ion microprobe (SHRIMP) study: *Contributions to Mineralogy and Petrology*, v. 122, p. 337-358.
- Vavra, G., and Schaltegger, U., 1999, Post-granulite facies monazite growth and rejuvenation during Permian to Lower Jurassic thermal and fluid events in the Ivrea zone (Southern Alps): *Contributions to Mineralogy and Petrology*, in press.
- Vavra, G., Schmid, R., and Gebauer, D., 1999, Internal morphology, habit and U-Th-Pb microanalysis of amphibolite-to-granulite facies zircons: geochronology of the Ivrea zone (Southern Alps): *Contributions to Mineralogy and Petrology*, in press.
- Vielzeuf, D., and Holloway, J. R., 1988, Experimental determination of the fluid-absent melting relations in the pelitic system: *Contributions to Mineralogy and Petrology*, v. 98, p. 257-276.
- Vielzeuf, D., and Pin, C., 1989, Geodynamic implications of granulitic rocks in the Hercynian belt, *in* Daly, J.S., Cliff, R.A., and Yardley, B.W.D. eds., *Evolution of Metamorphic Belts: Geological Society Special Publication No. 43*, p. 343-348.
- Vigneresse, J. L., Barbey, P., and Cuney, M., 1996, Rheological transitions during partial melting and crystallization with application to felsic magma segregation and transfer: *Journal of Petrology*, v. 37, p. 1579-1600.
- Voller, V. R., and Prakash, C., 1987, A fixed grid numerical modelling methodology for convection-diffusion mushy region phase-change problems: *International Journal of Heat and Mass Transfer*, v. 30, no. 8, p. 1709-1719.

- Voshage, H., Hofmann, A. W., Mazzucchelli, M., Rivalenti, G., Sinigoi, S., Raczek, I., and Demarchi, G., 1990, Isotopic evidence from the Ivrea Zone for a hybrid lower crust formed by magmatic underplating: *Nature*, v. 347, p. 731-736.
- Wells, P. R. A., 1980, Thermal models for the magmatic accretion and subsequent metamorphism of continental crust: *Earth and Planetary Science Letters*, v. 46, p. 253-265.
- Whitney, D. L., and Dilek, Y., 1998, Metamorphism during alpine crustal thickening and extension in Central Anatolia, Turkey: the Nigde Metamorphic Core Complex: *Journal of Petrology*, v. 39, p. 1385-1403.
- Whitney, D. L., and Irving, A. J., 1994, Origin of K-poor leucosomes in a metasedimentary migmatite complex by ultrametamorphism, syn-metamorphic magmatism and subsolidus processes: *Lithos*, v. 32, p. 173-192.
- Whitney, J. A., 1988, The origin of granite: The role and source of water in the evolution of granitic magmas: *Bulletin of the Geological Society of America*, v. 100, p. 1886-1897.
- Wickham, S. M., 1987, The segregation and emplacement of granitic magmas: *Journal of the Geological Society of London*, v. 144, p. 281-297.
- Wickham, S. M., and Oxburgh, E. R., 1987, Low-pressure regional metamorphism in the Pyrenees and its implications for the thermal evolution of rifted continental crust: *Philosophical Transactions of the Royal Society of London Series A*, v. 321, p. 219-242.
- Wildemuth, C. R., and Williams, M. C., 1984, Viscosity of suspensions modeled with a shear-dependent maximum packing fraction: *Rheologica Acta*, v. 23, p. 627-635.
- Wyllie, P. J., 1977, Crustal anatexis: An experimental review: *Tectonophysics*, v. 43, p. 41-71.
- Xu, G., Will, T. M., and Powell, R., 1994, A calculated petrogenetic grid for the system $K_2O-FeO-MgO-Al_2O_3-SiO_2-H_2O$, with particular reference to contact-metamorphosed pelites: *Journal of Metamorphic Geology*, v. 12, p. 99-119.
- Yardley, B. W. D., 1986, Is there water on the deep continental crust?: *Nature*, v. 323, p. 111.
- Zingg, A., 1980, Regional metamorphism in the Ivrea Zone (Southern Alps, N-Italy): Field and microscopic investigations: *Schweizerische Mineralogische und Petrographische Mitteilungen*, v. 60, p. 153-173.

- Zingg, A., 1983, The Ivrea and Strona-Ceneri Zones (southern Alps, Ticino and N.-Italy)- a review: Schweizerische Mineralogische und Petrographische Mitteilungen, v. 63, p. 361-392.
- Zingg, A., Handy, M. R., Hunziker, J. C., and Schmid, S. M., 1990, Tectonometamorphic history of the Ivrea Zone and its relationship to the crustal evolution of the Southern Alps: Tectonophysics, v. 182, p. 169-192.

APPENDIX A: DERIVATION OF THE LOGARITHMIC ISOCON METHOD

This is the re-derivation of the isocon method, which defines ΔC_i more intuitively

Terminology:

M^A = mass of altered rock

M^o = mass of original rock

M^Δ = change in mass of rock

M^A_i = mass of oxide i in altered rock

M^o_i = mass of oxide i in original rock

M^Δ_i = change in mass of oxide i in altered rock

C^A_i = concentration of oxide i in altered rock

C^o_i = concentration of oxide i in original rock

C^Δ_i = change in concentration of oxide i in altered rock

Relative to an arbitrary mass of the original rock (M^o), the mass of some component (i) after alteration equals the original mass plus any change in mass of that component. Similarly, the altered rock mass is equal to the original rock mass plus the change in mass during alteration. We have:

$$M_i^A = M_i^o + M_i^{\Delta} \quad \text{A.1}$$

$$M^A = M^o + M^{\Delta} \quad \text{A.2}$$

Dividing through by M^o to get units of concentration, we obtain:

$$\frac{M_i^A}{M^o} = \frac{M_i^o}{M^o} + \frac{M_i^{\Delta}}{M^o} \quad \text{A.3}$$

Multiplying both sides of the equation by the ratio of the mass before and after alteration (M^o/M^A), we have:

$$\left(\frac{M_i^A}{M^o}\right)\left(\frac{M^o}{M^A}\right) = \left(\frac{M_i^o}{M^o} + \frac{M_i^{\Delta}}{M^o}\right)\left(\frac{M^o}{M^A}\right) \quad \text{A.4}$$

Simplifying and converting to units of concentration gives:

$$C_i^A = C_i^o\left(\frac{M^o}{M^A}\right) + \frac{M_i^{\Delta}}{M^A} \quad \text{A.5}$$

Substituting equation A.2 for the quantity M^A , gives:

$$C_i^A = C_i^o \left(\frac{M^o}{M^o + M^A} \right) + \left(\frac{M_i^A}{M^o + M^A} \right) \quad \text{A.6}$$

Simplifying:

$$C_i^A (M^o + M^A) = C_i^o M^o + M_i^A \quad \text{A.7}$$

$$C_i^A M^o + C_i^A M^A = C_i^o M^o + M_i^A \quad \text{A.8}$$

$$C_i^A M^A = C_i^o M^o - C_i^A M^o + M_i^A \quad \text{A.9}$$

$$C_i^A M^A = M^o (C_i^o - C_i^A) + M_i^A \quad \text{A.10}$$

$$C_i^A = \frac{M^o}{M^A} (C_i^o - C_i^A) + \frac{M_i^A}{M^A} \quad \text{A.11}$$

Converting M_i^A/M^A to units of concentration gives:

$$C_i^A = \frac{M^o}{M^A} (C_i^o - C_i^A) + C_i^A \quad \text{A.12}$$

Solving for the concentration of component i in the altered rock, we have:

$$C_i^A = \left(\frac{M^o}{M^A} \right) C_i^o - \left(\frac{M^o}{M^A} \right) C_i^A + C_i^A \quad \text{A.13}$$

$$C_i^A + \left(\frac{M^o}{M^A}\right)C_i^A = \left(\frac{M^o}{M^A}\right)C_i^o + C_i^A \quad \text{A.14}$$

$$C_i^A \left(\frac{M^A + M^o}{M^A}\right) = \left(\frac{M^o}{M^A}\right)C_i^o + C_i^A \quad \text{A.15}$$

$$C_i^A = \left(\frac{M^o}{M^A}\right) \left(\frac{M^A}{M^A + M^o}\right) C_i^o + \left(\frac{M^A}{M^A + M^o}\right) C_i^A \quad \text{A.16}$$

From equation A.2, $M^A + M^o = M^A$. We can substitute to obtain:

$$C_i^A = \left(\frac{M^o}{M^A}\right)C_i^o + \left(\frac{M^A}{M^A}\right)C_i^A \quad \text{A.17}$$

Taking the natural log of both sides, we can see that:

$$\ln(100 \cdot C_i^A) = \ln \left[100 \cdot \left(\frac{M^o}{M^A}\right)C_i^o + 100 \cdot \left(\frac{M^A}{M^A}\right)C_i^A \right] \quad \text{A.18}$$

This step (equation A.18) simply makes the diagram legible so that the extent of alteration can be read graphically. The previous method used scaling factors rather than logarithms for this purpose. Unfortunately, different scaling factors have to be used for different elements, so a linear regression may not be used to obtain the isocon. The limitation of this formulation is that, since it is a logarithmic scale, the distance from the isocon will not be a direct measure of the extent of depletion. For

instance, 5% depletion in FeO in a metapelite (low concentration in the original rock) will plot a significant distance from the isocon, while 5% depletion in SiO₂ (high in concentration in the original rock) will plot much closer. In other words, lines of constant depletion will be asymptotic to the isocon.

For conserved elements, $C_i^A = 0$, so;

$$\ln(100 \cdot C_i^A) = \ln \left[100 \cdot \left(\frac{M^o}{M^A} \right) C_i^o \right] \quad \text{A.19}$$

$$\ln(100 \cdot C_i^A) = \ln(100 \cdot C_i^o) + \ln \left(\frac{M^o}{M^A} \right) \quad \text{A.20}$$

So, on a log-log plot, the immobile components generate a straight line of slope 1, whose intercept on the C^A axis (I) is the ratio of masses before and after alteration. We can calculate the mass change during alteration from this relationship:

$$\ln \left(\frac{M^o}{M^A} \right) = I \quad \text{A.21}$$

$$\frac{M^o}{M^A} = e^I \quad \text{A.22}$$

However, from equation A.2, we can write $M^A + M^o = M^A$. Substituting;

$$\frac{M^o}{M^o + M^{\Delta}} = e^f \quad \text{A.23}$$

$$M^o = e^f (M^o + M^{\Delta}) \quad \text{A.24}$$

$$M^{\Delta} = \frac{M^o - e^f M^o}{e^f} \quad \text{A.25}$$

$$M^{\Delta} = \frac{M^o(1 - e^f)}{e^f} \quad \text{A.26}$$

Since we defined C_i^{Δ} as the concentration of component i in the altering fluid, we can calculate the composition of the altering fluid directly from this method. This was not possible with the previous method, as C_i^{Δ} was defined as M^{Δ}/M^o . Although this is in concentration units, it is not the concentration of component i in the altering fluid.

The above derivation yielded separate equations for conserved and non-conserved elements. For non-conserved elements:

$$\ln(100 \cdot C_i^{\Delta}) = \ln \left[100 \cdot \left(\frac{M^o}{M^{\Delta}} \right) C_i^o + 100 \cdot \left(\frac{M^{\Delta}}{M^{\Delta}} \right) C_i^{\Delta} \right], \quad \text{A.27}$$

and conserved elements lie on the logarithmic isocon:

$$\ln(100 \cdot C_i^A) = \ln \left[100 \cdot \left(\frac{M^o}{M^A} \right) C_i^o \right]. \quad \text{A.28}$$

Starting from equation A.27, we can solve to obtain the concentration of component i in the altering fluid:

$$\ln(100 \cdot C_i^A) = \ln \left[100 \cdot \left(\frac{M^o}{M^A} \right) C_i^o + 100 \cdot \left(\frac{M^A}{M^A} \right) C_i^A \right] \quad \text{A.29}$$

$$C_i^A = \left(\frac{M^o}{M^A} \right) C_i^o + \left(\frac{M^A}{M^A} \right) C_i^A. \quad \text{A.30}$$

$$\left(\frac{M^A}{M^A} \right) C_i^A = \left(\frac{M^o}{M^A} \right) C_i^o + C_i^A \quad \text{A.31}$$

$$C_i^A = \left(\frac{M^A}{M^A} \right) C_i^A - \left(\frac{M^o}{M^A} \right) C_i^o \quad \text{A.32}$$

CURRICULUM VITA

Scott A. Barboza

University of Washington

1998

EDUCATION

June 1995 - Present
Ph.D. Geology
University of Washington

September 1993 - June 1995
M.S. Geology
University of Washington

September 1990 - June 1993
B.S. (High Honors) Geology
University of California, Davis

HONORS AND AWARDS

1999 David A. Johnston Memorial Award
1997 - 1998 Peter Misch Fellowship
1994 Richard E. Fuller Scholarship
1993 UCD Geology Department Citation for Academic Excellence
1992 Everett Dale Jackson Scholarship

ASSOCIATION MEMBERSHIPS

American Geophysical Union
Geological Society of America
Mineralogical Society of America
American Association of Petroleum Geologists

THESES

Barboza, S.A., 1995, *The dynamics of dehydration melting and implications for melt extraction in the lower crust following underplating: an example from the Ivrea-Verbano Zone, northern Italy*. Unpublished M.S. Thesis, University of Washington.

Barboza, S.A., 1993, *The impact of layered mantle convection on the spatial stability of hot spot plumes in the upper mantle*. Unpublished Honors Thesis, University of California, Davis.

PUBLISHED PAPERS

Barboza, S.A., 1998, Field guide to the migmatites of the southern Ivrea zone: GSA Penrose Conference Volume.

Barboza, S.A. and Bergantz, G.W., 1998, Rheological transitions and the progress of melting of crustal rocks: *Earth and Planetary Science Letters*, v. 158, p. 19-29.

Barboza, S.A. and Bergantz, G.W., 1997, Melt productivity and rheology: complementary influences on the progress of melting: *Numerical Heat Transfer, Part A*, v. 31, p. 375-392.

Barboza, S.A. & Bergantz, G.W., 1996, A dynamic model of dehydration melting motivated by a natural analogue: applications to the Ivrea-Verbano Zone, northern Italy: *Transactions of the Royal Society of Edinburgh: Earth Science*, v. 87, p. 23-31.

MANUSCRIPTS IN REVIEW

Barboza, S.A., Bergantz, G.W. & Brown, M., 1999, Regional granulite-facies metamorphism in the Ivrea zone: Is the Mafic Complex the smoking gun or a red herring?: *Geology*, in review.

MANUSCRIPTS IN PREPARATION

Barboza, S.A. & Bergantz, G.W., 1998, Metamorphism and anatexis in the Mafic Complex contact aureole, Ivrea zone, northern Italy: *Journal of Petrology*.

WORK IN PROGRESS

Barboza, S.A., 1999, Isocon analysis applications in igneous and metamorphic geology: *Journal of Metamorphic Geology*.

Barboza, S.A., Quick, J.E., and Sinigoi, S., 1999, Origin of leucotonalite leucosomes in the Mafic Complex contact aureole, Ivrea zone, northern Italy: *Journal of Geology*.

CONFERENCE PRESENTATIONS

Barboza, S.A., Bergantz, G.W., & Brown, M., 1998, Basaltic magmatism and regional metamorphism in the Ivrea zone: Revisions to the underplating model: GSA Penrose Conference Abstract Volume.

Barboza, S.A. and Bergantz, G.W., 1997, Melt productivity and rheology: complementary influences on crustal melting following underplating: EOS, v. 78 (46), p. F797.

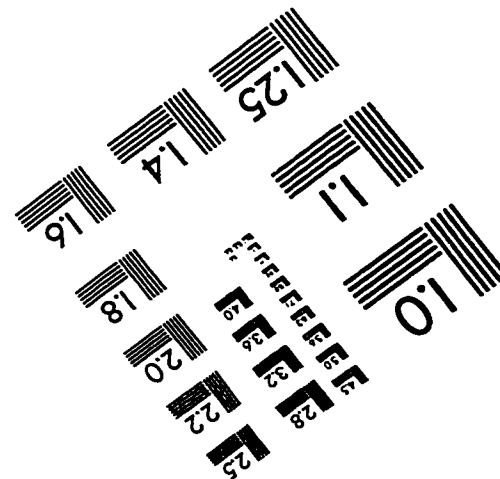
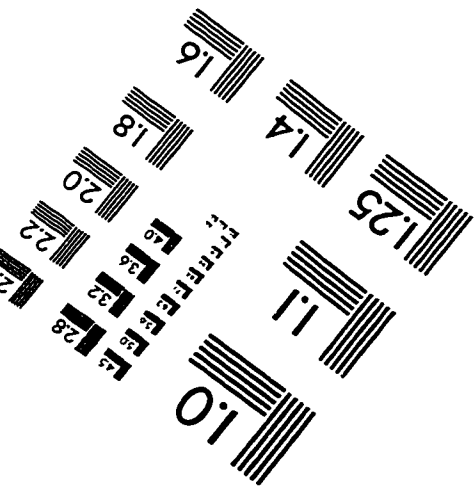
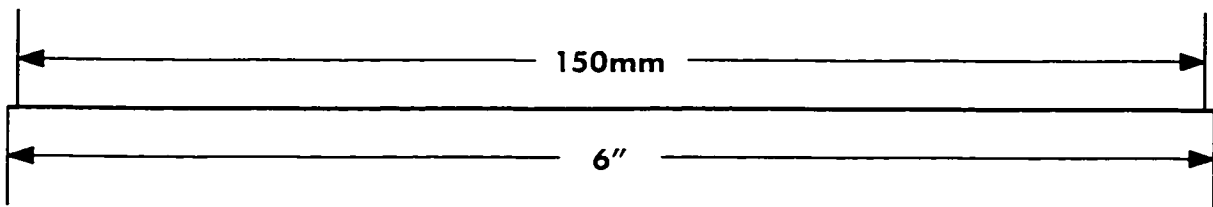
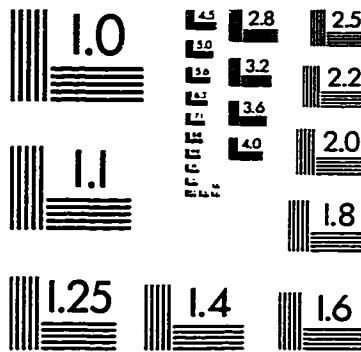
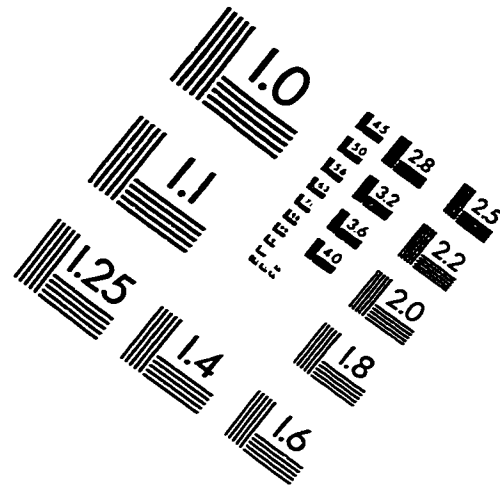
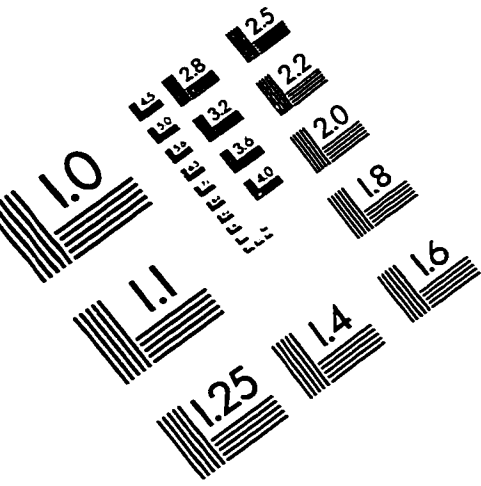
Barboza, S.A. and Bergantz, G.W., 1995, The dynamics of melting and implications for melt extraction in the lower crust following basaltic underplating: EOS, Transactions of the American Geophysical Union, v. 76 (46), p. F691.

Barboza, S.A. and Bergantz, G.W., 1995, The dynamics of dehydration melting and implications for melt extraction in the lower crust following underplating: An example from the Ivrea-Verbano Zone, northern Italy: U.S. Geological Survey, Circular, v. 1122, p. 94.

Barboza, S.A. and Bergantz, G.W., 1994, Thermal and dynamical state of the lower crust following underplating: Implications for melt generation and petrologic diversity: EOS, Transactions of the American Geophysical Union, v. 75 (44), p. 729.

Bergantz, S.A. and Barboza, S.A., 1994, From mush to MASH: Underplating, gabbro "glaciers" and partial melting in the lower crust, applications to the Ivrea-Verbano Zone and the Basin and Range Province: EOS, Transactions of the American Geophysical Union, v. 75 (16), p. 359.

IMAGE EVALUATION TEST TARGET (QA-3)



APPLIED IMAGE, Inc
 1653 East Main Street
 Rochester, NY 14609 USA
 Phone: 716/482-0300
 Fax: 716/288-5989

© 1993, Applied Image, Inc., All Rights Reserved